

## ABSTRACT

CASTELLANOS, NATASHA IRIS. Formulation and Characterization of Novel Soft Magnetic Beads, Magneto-capillary Gels, and Responsive Soft Structures (Under the direction of Dr. Orlin D. Velev).

Magnetic fields offer superior control over the assembly, dynamics, and reconfiguration of colloidal particles. However, synthesizing ‘soft’ colloidal particles with switchable magnetic dipole moment remains a challenge, while such particles could form the basis of numerous responsive gels and soft materials with new properties and functionality.

In this dissertation, we present a way to overcome this fundamental challenge based on a strategy to synthesize soft microbeads with tunable residual dipole moments. The microbeads are composed of polydimethylsiloxane (PDMS) matrix with internally embedded magnetic nanoparticles (MNPs). The distribution and orientation of the MNPs within the PDMS bead matrix is controlled by an external magnetic field during the synthesis process, thus allowing for the preparation of anisotropic PDMS microbeads with internally aligned nanoparticle chains. We study and present the differences in the magnetic interactions between microbeads containing magnetically aligned MNPs and microbeads with randomly distributed MNPs. The suspensions of microbeads with randomly distributed MNPs were responsive to applied magnetic fields but did not otherwise form any permanent network in the absence of a field. Contrastingly, the interparticle interactions in suspensions of microbeads with embedded aligned MNP chains result in the spontaneous formation of percolated networks due to residual magnetization. The structure in these suspensions can be switched by applying magnetization, demagnetization, and re-magnetization cycles that correspondingly evoke formation, break-up, and reformation of 2D percolated networks. The mechanical response of the microbead suspension was quantified by oscillatory rheology and correlated to the propensity for network formation by the magnetic

microbeads. We also correlated experimentally the 2D alignment of the microbeads to the direction of earth's magnetic field. Overall, the results prove that the soft magnetic microbeads enable rich variety of structures and can serve as an experimental toolbox for modelling interactions in dipolar systems leading to various percolated networks, novel magneto-rheological materials, and smart gels.

Magnetically responsive polymer-based materials are of large interest due to their biocompatibility and the ease of controlling the structure when making composite materials. We reported how the control of the capillary forces and magnetic interactions can be used for magnetically directed assembly of novel magneto-capillary gels. We present two types of such Magnetically Responsive Capillary Gels (MRCGs). In MRCG Type 1, the magnetic nanoparticles (MNPs) are dispersed in the liquid phase that forms capillary bridges between the PDMS microspheres. MRCG Type 2 is constituted of magnetically responsive PDMS microbeads with internally embedded, randomly distributed MNPs. We characterized the properties of the gels with respect to rheology, magnetic response, and ability to re-assemble on field application. We established that the formation of capillary bridges between PDMS microbeads via the addition of a secondary, immiscible fluid leads to gelation. Both MRCGs exhibit the property of magnetic field induced self-repair. These data are correlated to the MRCG's structure and response.

Magnetic interaction templating was conducted to study and manipulate the magnetic response of the beads with magnetically aligned MNPs. Several techniques were applied with the end goal of making uniform magnetic anchor sites with reproducible morphology length scale comparable to that of the magnetic beads. A homocomposite, capillary-based 3D printing method proved to be the best option for making structures with these characteristics. We studied these 3D printed structures as potential magnetic anchor sites for no-slip conditions of magnetic gel

characterization. These anchor sites may achieve better distributed rheology sample loading, due to the magnetic interactions of the suspensions and the printed structures, and in turn achieve accurate rheological characterization. Overall, we have constructed a rich toolbox of structural and interaction capabilities that can be applied to a variety of magnetically and capillary networked colloidal systems.

© Copyright 2021 by Natasha Castellanos

All Rights Reserved

Formulation and Characterization of Novel Soft Magnetic Beads, Magneto-capillary Gels, and Responsive Soft Structures

by  
Natasha Iris Morales Castellanos

A dissertation submitted to the Graduate Faculty of  
North Carolina State University  
in partial fulfillment of the  
requirements for the degree of  
Doctor of Philosophy

Chemical Engineering

Raleigh, North Carolina  
2021

APPROVED BY:

---

Dr. Orlin D. Velez  
Committee Chair

---

Dr. Bhuvnesh Bharti  
External Member

---

Dr. Saad Khan

---

Dr. Joseph Tracy

---

Dr. Lilian Hsiao

## **DEDICATION**

*This dissertation is dedicated to my family for their everlasting love and support, especially to my mother, my husband, and my daughter. You are my biggest motivation.*

*¡Los amo!*

## BIOGRAPHY

Natasha Iris Morales Castellanos was born in Lázaro Cárdenas, Michoacán, México. She immigrated to Winston Salem, NC, USA with her mother, Norma Castellanos Valdivia, when she was five years old. Natasha is the eldest of three siblings. She attended several elementary schools and middle schools before graduating salutatorian from Robert B. Glenn High School in Kernersville, NC in 2012.

Upon graduation, Natasha began her undergraduate studies at Salem College. As a first-generation college student and immigrant, Natasha sought opportunities to reach out to middle school and high school students to encourage a college-bound path. To this end, she participated in the Middle School Achievers program and the Latino Achievers program. Natasha also took part in campus life. She was an orientation leader throughout her time at Salem, a peer mentor, and a campus tour guide for potential students. Natasha also held executive positions for several clubs such as the Salem Chapter of the American Chemical Society. She was nominated to be a tutor for math and science courses as part of Salem's QUEST program. Her passion for teaching led her to be a middle school math tutor for the Winston Salem Forsyth County School system at the Downtown School. She continues to be a private tutor for math, science, and Spanish courses today.

Natasha completed undergraduate research with Salem biochemistry professor Dr. Jing Ye studying the effect of pH on proteins throughout her undergraduate studies. In the summer of 2013, she received an NSF fellowship to work under the supervision of Dr. Lachgar in the chemistry department at Wake Forest University. In the summer of 2014, she joined an organic chemistry-focused project as a Translational Science Center intern under the supervision of chemistry professor Dr. King. Lastly, in the summer of 2015, she joined Dr. Marini's lab on a breast cancer-

focused microscopy imaging project at the Wake Forest Institute for Regenerative Medicine (WFIRM). During her last two years of undergraduate studies, Natasha also worked in the Regulatory Affairs/ Quality Assurance department at Carolina Liquid Chemistries at the Biotech Place in Winston Salem, NC. She graduated *summa cum laude* in May 2016 with a Bachelor of Science in Chemistry and Mathematics and minors in Statistics and Spanish with Chemistry Honors.

Her exposure to research during her undergraduate studies led Natasha to pursue a Ph.D. In August 2016, Natasha moved to Raleigh to begin her graduate studies in the Chemical and Biomolecular Engineering at North Carolina State University. She joined Dr. Orlin D. Velev's research group in January 2017. Natasha is passionate about education and STEM and because of this has participated in numerous community outreach activities at NC State and in the surrounding Research Triangle area. During her time at NC State, Natasha has also been a recruiting captain for the Chemical Engineering department for two consecutive years. In the summer and fall 2020, Natasha held an internship in the technical development team at Baebies, Inc. in Research Triangle Park, NC, where she helped develop newborn screening assays for Acute Kidney Injury.

Natasha married Antonio Clemente in September 2016. They welcomed their energetic daughter, Natalya Clemente Castellanos, on August 16, 2017. After completing her Ph.D., Natasha plans to spend a couple of months dedicated to her family before applying for an industry position. Her ultimate career goal is to be a professor at a teaching-focused college or university.

## ACKNOWLEDGMENTS

I would like to thank God first and foremost for his countless blessings and for giving me the opportunity to get to where I am today. The odds were often against me. As a five-year-old in a new country, unable to communicate due to the language barrier, I never could have imagined myself where I am at professionally 22 years later.

Next, I would like to thank my advisor, Dr. Orlin D. Velev, for his guidance and constant encouragement over the past five years. There are few people in this world that love their job and are as dedicated to it as he is, and I am thankful to have gotten the opportunity to be mentored by a person like him. He has been such a great inspiration to me. I will be forever grateful for his research enthusiasm and his ability to motivate and uplift me even at times when I felt discouraged.

I would like to thank all members of my doctoral committee: Dr. Saad Khan, Dr. Lilian Hsiao, Dr. Joseph Tracy, Dr. Bhuvnesh Bharti, and recently, Dr. Jan Genzer. I was fortunate enough to have taken at least one course under most of you and I am thankful for all that I learned from each of you both in and out of the classroom. Thank you all for all the valuable discussions and for your willingness to answer any questions I had about my research throughout my studies.

I would also like to thank all the members of the Velev group that I had a chance to interact with. It was a pleasure to collaborate, learn, and work with all of you. Cathryn, thanks for making sure the lab ran smoothly and for helping me with any imaging questions. Sabina, you are such an inspiration and I feel honored to have worked with you. Austin, thank you for always being willing to help. Tamoghna and Lilian, it's been great learning and working alongside you. Rachel and Sneha, thanks for all you do for the group, and I can't wait to see how you will continue to help the group dynamic going forward. I want to especially thank Dr. Sangchul Roh for helping me get

started with my project. Thank you for being my peer mentor and for the valuable advice and research discussions.

I would like to thank all the colleagues and friends I had a chance to interact with in my department, especially those that started the graduate school journey with me. First year, first semester was one of the toughest times I have ever faced both professionally and personally and I was lucky to be supported by people like Javier, Siyao, Jiaqi, and Daniel. I couldn't have gotten through it without you. I would also like to give a special thanks to Leah. Thank you for your patience and most of all, thank you for your friendship. Thanks for allowing me into your home. I will forever cherish all our conversations. To the administrative staff from the Department, (especially Sandra, Angela, and Michelle) who helped me countless times, thank you! I felt beyond blessed to be a member of such a collaborative, supportive, friendly, and welcoming environment.

Next, I would like to thank all the mentors I have had throughout my life. I truly wouldn't have gotten to where I am if it weren't for you believing in me: Mrs. Muller, Mrs. Hefner, and Mrs. Parnell, just to name a few. Thank you for instilling in me the joy of teaching and mentoring. From Salem College, I would like to thank Dr. Mattox, Dr. McKnight, and especially Dr. Ye for all her guidance and advice for graduate school. Thank you to all the scholarship programs that sponsored me for being such a key part of my undergraduate journey.

Lastly, I want to especially thank my family for all their support. To my husband, Antonio, thank you for being my rock, for being so supportive and understanding, and for constantly reminding me that everything will be okay during stressful times. To my daughter, Natalya, thank you, my little one, for doing more for me than you will ever know. Seeing your little face and hearing your laughter was my biggest motivation during the roughest times. To my mother and best friend, Norma, ¡gracias por todo! Thank you for all the sacrifices you made, for leaving your

country in search for a better future for me. Thank you for never ceasing to take care of me and for always helping me in any way that you can. A special thanks to my stepfather, Juan, for being the most loving and supportive stepparent. Thank you to my siblings, Andrick and Arlin, for being my biggest cheerleaders and for reminding me to stay humble. To my childhood best friend, Sadye, thank you for being patient with me and for remaining by my side even during the busiest and hardest times.

The list could truly go on. I thank everyone that has been a part of my personal and professional village. Thank you all, from the bottom of my heart!

## TABLE OF CONTENTS

LIST OF TABLES .....	xi
LIST OF FIGURES .....	xii
<b>Chapter 1: Assembly of responsive particle structures by magnetic and capillary interactions .....</b>	<b>1</b>
1.1 Introduction.....	1
1.2 Dispersed magnetic particles .....	4
1.3 Responsive soft materials with embedded magnetic particles.....	11
1.4 Magnetic interactions and structures from anisotropic colloidal particles .....	15
1.5 Magnetically responsive foams, gels, and coatings .....	18
1.6 3D printing in magneto-capillary pastes .....	22
1.7 Conclusions.....	23
1.8 Dissertation Outline .....	24
1.9 References.....	25
<b>Chapter 2: Field-driven reversible alignment and gelation of magneto-responsive soft anisotropic microbeads .....</b>	<b>30</b>
2.1 Introduction.....	30
2.2 Materials and Method .....	35
2.2.1 Dispersing the magnetic nanoparticles within the PDMS precursor medium .....	35
2.2.2 Synthesis of PDMS microbeads containing randomly distributed MNPs .....	35
2.2.3 Synthesis of PDMS microbeads containing magnetically aligned MNPs.....	36
2.2.4 Rheological Analysis of magnetic microbead suspensions .....	36
2.2.5 Optical Microscopy and Cell Orientation .....	37
2.2.6 Magnetometry .....	37
2.3 Results and Discussion .....	38
2.3.1 Bead Synthesis and Morphology .....	38
2.3.2 Bead Magnetic Interaction.....	41
2.3.3 Bead Assembly and Demagnetization .....	43
2.3.4 Other types of magnetic material embedded in the PDMS beads .....	46
2.3.5 Rheology of both types of magnetic ( $\text{Fe}_2\text{O}_3$ ) SMBs.....	53
2.3.6 Magnetometry characterization of the microbeads.....	57
2.3.7 Interaction Energy of the Microbeads.....	61
2.3.8 Long-range organization of the microbeads in weak magnetic fields .....	64
2.4 Concluding remarks .....	66
2.5 Acknowledgements.....	68
2.6 References.....	69

<b>Chapter 3: Design and Characterization of Novel Magnetocapillary Gels</b> .....	76
3.1 Introduction.....	76
3.2 Materials and Methods.....	77
3.2.1 Non-magnetic beads.....	77
3.2.2 Dispersing the magnetic nanoparticles within the PDMS Precursor medium .....	78
3.2.3 Synthesis of PDMS beads containing randomly distributed MNPs .....	79
3.2.4 Synthesis of MRCG type 1: capillary bridging with MNPs .....	80
3.2.5 Synthesis of MRCG type 2: Capillary bridging without MNPs .....	80
3.2.6 Rheological Analysis of Capillary Gels.....	81
3.2.7 Optical Microscopy.....	81
3.2.8 Self-Repair Testing.....	81
3.2.9 Magnetometry specifications .....	82
3.2.10 Temperature rheology study specifications .....	83
3.3 Results and Discussion .....	83
3.3.1 Magnetic characterization of the magneto-capillary gels .....	93
3.3.2 Magnetically assisted self-repairing .....	96
3.3.3 Rheology self-repair study.....	102
3.3.4 Temperature study of the magnetic gels .....	108
3.3.5 Other types of magneto-capillary gels studied.....	111
3.4 Conclusions.....	112
3.5 Acknowledgements.....	112
3.6 References.....	113

<b>Chapter 4: Design of 3D printed anchor sites for enhanced characterization of soft magnetic gels</b> .....	116
4.1 Introduction.....	116
4.2 Materials and Methods.....	119
4.2.1 Synthesis of magnetic PDMS prepolymer (10 wt% MNPs).....	119
4.2.2 Synthesis of PDMS beads containing embedded magnetic nanoparticles .....	119
4.2.3 Synthesis of PDMS beads containing embedded, aligned magnetic nanoparticles .....	119
4.2.4 Permanent NdFeB magnet specifications .....	120
4.2.5 Fabrication of precursor magnetic anchor sites (large magnet).....	120
4.2.6 Fabrication of precursor magnetic anchors (two small magnets) .....	120
4.2.7 Fabrication of precursor magnetic anchor sites (large magnet).....	120
4.2.8 Fabrication of precursor droplet magnetic anchors (two small magnets).....	121
4.2.9 Fabrication of dispersed magnetic anchors .....	121
4.2.10 Fabrication of Mayer rod coated magnetic anchors.....	121
4.2.11 Fabrication of 3D printed homocomposite, PDMS capillary structures .....	122
4.2.12 3D printer specifications .....	123
4.2.13 Optical Microscopy.....	123

4.2.14 Rheological characterization of chained bead gels .....	123
4.3 Results and Discussion .....	124
4.3.1 Other attempted magnetic anchoring techniques .....	124
4.3.2 3D printed homocomposite, PDMS capillary structures .....	132
4.3.3 Magnetic interaction of soft magnetic gel and the 3D printed structures.....	142
4.3.4 Interaction of chained beads and printed structures under a rotating magnetic field .....	143
4.3.5 Demagnetization studies of the soft magnetic gel and 3D printed structures.....	145
4.3.6 Rheological characterization of the soft magnetic gels .....	149
4.3.7 NdFeB as magnetic material in 3D printed structures .....	151
4.4 Conclusions.....	153
4.5 Acknowledgements.....	154
4.6 References.....	155
<b>Chapter 5: Conclusions and Future Directions.....</b>	<b>159</b>
5.1 Summary .....	159
5.2 Future Outlook .....	161
5.3 References.....	168
APPENDICES .....	169
Appendix A.....	170
Appendix A.1 .....	171
Appendix A.2.....	172

## LIST OF TABLES

<b>Table 3.1</b>	Force calculations for sample self-repair experiment.....	82
<b>Table 3.2</b>	Squareness ratio of magneto-capillary gels .....	94
<b>Table 3.3</b>	Summary of the gel repair effectiveness by adhesion or the application of a magnetic field .....	102
<b>Table 3.4</b>	Summary of the self-repair time of the magnetic gels during the rheology measurements.....	108

## LIST OF FIGURES

<b>Figure 1.1</b>	Highlights of the topics and the focus of the introductory chapter: (a) Systems with dispersed magnetic particles, (b) Systems with embedded magnetic particles, (c) Interactions and assembly of patchy particles, (d) Making and properties of magnetically responsive foams, gels, and coatings, and (e) Capillary-mediated 3DP and magnetic actuation of soft matter .....	3
<b>Figure 1.2</b>	Examples of dispersed magnetic particle systems. (a) Superparamagnetic particles align in the direction of the applied magnetic field (left). Microscopy images of 5 $\mu\text{m}$ induced “double” dipole superparamagnetic particles showing staggering branched formation at high concentrations due to the applied complex (electric and magnetic) fields (right). (b) A temperature dependent, fatty acid-coated nanoparticle filament system that can use capillary force to form capillary bridges between the magnetic nanoparticles at higher temperatures that break apart at lower temperatures. This nanoparticle system also has magnetically assisted self-repairing properties. (c) Microscopy images highlighting the evolution of the suspension percolation after having a pulsed magnetic field applied for varying lengths of time at varying applied pulse frequencies. (d) Magnetic particles can undergo complex fields such as a combination of magnetic and electric fields (left). Complex particles such as Janus particles can also have complex interactions due to their differing hemisphere composition.....	8
<b>Figure 1.3</b>	Examples of magnetically embedded smart materials including (a) magnetically aligned embedded particles in elastomer films (b) magnetically aligned and embedded particles in an elastomer matrix, (c) microscale building blocks or “voxels” whose magnetic response is controlled by its complex structure. (d) polymeric nanocomposite actuators with heterogeneous magnetic anisotropy .....	14
<b>Figure 1.4</b>	Examples of patchy particles including Janus particles, microbots, and snowman shaped polystyrene/magnetite particles .....	17
<b>Figure 1.5</b>	Examples of a (a) thermophotomagnetic foam (b) magnetic-induced gel and a (c) magnetic field-driven coating .....	21
<b>Figure 1.6</b>	Direct writing extrusion-based 3D printing of homocomposite magneto-capillary pastes previously introduced by the Velev group .....	23
<b>Figure 2.1</b>	Schematics of the method of synthesizing PDMS microbeads with embedded iron (III) oxide nanoparticles using an emulsification technique. The internal organization of the magnetic nanoparticles can be preserved if the soft microbeads (SMBs) are cured under a magnetic field. The SMB microscope image examples shown are bigger than those typically used for the experiments (10 $\mu\text{m}$ ) for better visualization.....	34

<b>Figure 2.2</b>	(a) Magnetic elastomer spheres dispersed in water where the embedded MNPs can have two different orientations by having either (b) embedded randomly distributed iron (III) oxide nanoparticles (10 wt%, no field applied), or (c) magnetically aligned iron (III) oxide nanoparticles (10 wt%, field of 19 mT strength applied during curing). Scale bars are 20 $\mu\text{m}$ .....37
<b>Figure 2.3</b>	Optical microscopy images of PDMS beads containing 2.5 wt% of magnetic nanoparticles in (a) randomly dispersed state and (b) polymerized after the MNPs have been aligned in the presence of magnetic field. Note that the MNPs in some beads can be aligned in the form of single chain traversing the host bead. (c) Optical microscopy image of a suspension of PDMS beads containing 10 wt% of aligned magnetic nanoparticles. The higher density chains in the beads are clearly distinguishable .....40
<b>Figure 2.4</b>	The magnetic interactions in SMB suspensions (50 wt% PDMS microbeads in water, each containing 10 wt% MNPs) can vary as: (a) When MNPs are randomly dispersed inside, the microbeads do not appear to interact without the presence of an external magnetic field even when they have been subjected to external field earlier (“pre-magnetized”). (b) They demonstrate very weak chaining and branching only if the system is subjected to a magnetic field (19 mT). (c) Microbeads with embedded magnetically aligned MNPs form branched networks when pre-magnetized, even if external field is not applied, and (d) form organized percolated networks and align in the direction of an applied magnetic field (19 mT). Scale bars are 200 $\mu\text{m}$ .....42
<b>Figure 2.5</b>	The magnetically aligned microbead system demonstrated tunability by using reversible magnetization. (a) The aligned PDMS microbeads form branched networks even if no external magnetic field is applied due to the pre-magnetization during fabrication and (b) form more organized branched structures when an external field is applied ( $H = 19 \text{ mT}$ ). (c) These long-ranged structures break apart when the system is disturbed but can re-form almost immediately. (d) They can break down into mostly individual microbeads if the suspension is demagnetized but can re-assemble when re-magnetized. The black arrows indicate the direction of the external magnetic field. Scale bars are 200 $\mu\text{m}$ .....45
<b>Figure 2.6</b>	Microscopy images of PDMS beads with embedded NdFeB microparticles sheared at (a) 500 RPM and (b) 1000 RPM during emulsification. (c) Microscopy images of magnetic PDMS beads with embedded NdFeB microparticles that were demagnetized before curing .....48
<b>Figure 2.7</b>	Microscopy images of NdFeB PDMS beads that were (a) demagnetized for 7 minutes and then sonicated for 5 seconds prior to imaging, (b) demagnetized for 20 minutes and then sonicated for 5 seconds prior to imaging, (c) demagnetized for 20 minutes and then vortexed for 5 seconds prior to imaging, (d) demagnetized for an hour and then sonicated for 5

	seconds prior to imaging, and (e) demagnetized for an hour and then vortexed for 5 seconds prior to imaging .....	50
<b>Figure 2.8</b>	Microscopy images of NdFeB PDMS beads (a) with no magnetic field applied during curing, (b) with a magnetic field of 19 mT field strength applied during curing, and (c) the percolation network formation of the NdFeB PDMS beads that were magnetized (H= 19 mT) during curing.....	52
<b>Figure 2.9</b>	Storage, $G'$ , and loss, $G''$ , moduli as a function of frequency for each type of magnetic microbead. (a) The lack of interactions between the SMBs with randomly distributed MNPs demonstrates lower $G'$ and $G''$ and more liquid-like properties whereas in (b) the weak interactions between the magnetically aligned SMBS with embedded chains lead to magnetic force-induced structuring or 'soft' gel-like properties (50 wt% PDMS microbead to water, 10 wt% embedded MNPs) .....	53
<b>Figure 2.10</b>	Storage, $G'$ , and loss, $G''$ , moduli as a function of frequency for magnetic microbeads with (a) 2.5 wt%, (b) 5 wt%, and (c) 10 wt% aligned MNPs embedded in the SMB PDMS matrix. The gel strength increases as the number of MNPs loaded in the microbeads increases .....	55
<b>Figure 2.11</b>	Normalized storage, $G'$ , and loss, $G''$ , moduli for magnetic microbeads with 2.5 wt%, 5 wt%, and 10 wt% aligned MNPs embedded in the SMB PDMS matrix. The normalization of the rheology data (by dividing the moduli by the wt% of MNPs) results in good (but not complete) clustering of the curves, highlighting a general correlation between the weight % of MNPs in the microbeads and the viscoelasticity of the dispersion .....	57
<b>Figure 2.12</b>	Magnetization curves for (a) microbeads with randomly distributed MNPs and the (b) microbeads with embedded, magnetically aligned MNPs. These curves represent the normalized magnetic moment of the beads containing 10 wt% of MNPs as a function of the applied magnetic field. The arrows indicate the scan direction, when the applied field goes up or down during the measurement .....	59
<b>Figure 2.13</b>	Estimated interaction energy between two PDMS microbeads with 10 wt%, non-aligned and aligned MNPs embedded in the PDMS bead matrix (with $d = 10 \mu\text{m}$ ).....	62
<b>Figure 2.14</b>	The magnetic microbeads orient and organize in ways so that the embedded magnetic particle chains face the same direction and form linear structures that align in the direction of Earth's magnetic field (sample is 10 wt% MNPs in SMBs, the direction of the Earth' field is shown in the compass sensor image). Such orientation presents a fascinating analogy with the one observed with magnetotactic bacteria in nature .....	64

<b>Figure 3.1</b>	Bright field microscopy images of PDMS beads without internalized MNPs synthesized at increasing RPM varying from 500 RPM to 3000 RPM (left to right).....	84
<b>Figure 3.2</b>	Brightfield microscopy images of composite PDMS beads containing randomly distributed Fe <sub>2</sub> O <sub>3</sub> MNPs .....	85
<b>Figure 3.3</b>	Summary of the magnetocapillary gels synthesized, which differed by the location of the magnetic iron oxide nanoparticles (MNPs) as well as the control capillary gel. The Magnetically Responsive Capillary Gel (MRCG) type 1 was the gel type with MNPs in the PDMS beads, MRCG type 2 was the gel type with MNPs in the oleic acid capillary bridges. (a) Bright field image of control gel, (b) Fluorescence microscopy image of control gel, (c) Bright field image of MRCG type 1, (d) Fluorescence microscopy image of MRCG type 1, (e) Bright field image of MRCG type 2, (f) Fluorescence microscopy image of MRCG type 2.....	86
<b>Figure 3.4</b>	Gels with randomly dispersed MNPs in (a-d) the OA and (e-h) the PDMS beads with 10 wt%-40 wt% OA (left to right). All samples passed the gel inversion test by staying in one piece even when sample was turned upside down.....	87
<b>Figure 3.5</b>	An example of the magnetic response of the gel samples in the presence of a permanent magnet with (a) the sample being initially cut into several pieces and (b) then merged back into one piece in response to the proximity of the magnet in as little as 3 seconds.....	88
<b>Figure 3.6</b>	Angular frequency dependence of elastic (storage) modulus (filled symbols) and viscous (loss) modulus (open symbols) in the linear viscoelastic regime of our control samples (green), samples with randomly dispersed magnetic nanoparticles in the PDMS beads (red) and samples with magnetic nanoparticles in the oleic acid (blue) at varying weight percent of oleic acid (a) 20 wt% (b) 30 wt% and (c) 40 wt% .....	91
<b>Figure 3.7</b>	Relationship between the amount of oleic acid present in the gels and the elastic (storage, G') modulus in the linear viscoelastic regime (when frequency= 1 rad sec <sup>-1</sup> ) of our control samples (green), samples with randomly dispersed magnetic nanoparticles in the PDMS beads (red) and samples with magnetic nanoparticles in the oleic acid (blue).....	92
<b>Figure 3.8</b>	Overlay of magnetization graphs of (a) 20 wt% OA gels, (b) 30 wt% OA gels, and (c) 40 wt% OA gels. Insets show an expanded graph in the region from -10 to 12 kOe.....	95
<b>Figure 3.9</b>	Illustration of a magnetic gel self-repair driven by a permanent magnet, which enabled the capillary gel to regain its one-piece integrity.....	97

<b>Figure 3.10</b>	Illustration of self-repair experiments conducted either with an external magnetic field or with a force exerted on the sample and with samples in water medium. (a) Schematic of magnetically assisted self-repair and (b-e) Images of the steps in corresponding experiment. (f) Schematic of how the self-repair of a gel is conducted using the same force applied through a glass slide and (g-j) Images of the steps in corresponding experiment .....	100
<b>Figure 3.11</b>	Rheological data for the capillary gels of varying concentrations of OA with MNPs in the OA capillary bridges. These experiments were conducted to confirm gel self-repair. (a) 10 wt% OA, (b) 20 wt% OA, (c) 30 wt% OA, and (d) 40 wt% OA.....	104
<b>Figure 3.12</b>	Rheological data gathered for the capillary gels of varying concentrations of OA with 10 wt% MNPs in the PDMS beads. These experiments were conducted to confirm gel self-repair. (a) 10 wt% OA, (b) 20 wt% OA, (c) 30 wt% OA, and (d) 40 wt% OA .....	106
<b>Figure 3.13</b>	Angular frequency dependence of $G'$ (filled symbols) and $G''$ (open symbols) of samples stored in the oven (blue square), stored in the fridge (red circle) and stored in the freezer (green triangles) for gels with (a) 10 wt% MNPs in the PDMS beads with 10 wt% OA composition and (b) PDMS beads with 10 wt% MNPs in the OA at 10 wt% OA composition .....	110
<b>Figure 3.14</b>	A third type of magneto-capillary gel with PDMS beads with 10 wt% magnetically aligned embedded MNPs. (a) Schematic of this type of gel (b) Microscopy image of this type of gel .....	111
<b>Figure 4.1</b>	Images of the set-ups from some of the different methods that were tested for making magnetic anchors. (a) Highlights the methods involving spreading magnetic PDMS precursor (10 wt% dispersed, shown on left) or forming droplets (right) and using a single large permanent NdFeB magnet ( $H=50$ mT) to magnetize the $Fe_2O_3$ MNPs. (b) Shows the methods involving spreading magnetic precursor (10 wt% dispersed, shown on left) and using two smaller permanent NdFeB magnets ( $H=22$ mT, shown on the right). (c) Presents a method that includes a suspension of the magnetically aligned beads magnetized between two small permanent NdFeB magnets ( $H=22$ mT). (d) (top left and right) Microscopy images of a 5 wt% MNPs droplet that was cured under the presence of the two smaller permanent magnets. The remaining microscopy images show how dispersed chained PDMS beads interact and anchor to the cured $Fe_2O_3$ nanoparticles within a 1 wt% MNPs droplet.....	127
<b>Figure 4.2</b>	Highlights of a promising magnetic anchoring method involving the Mayer rod technique. (a) Images of glass slides that were coated with different concentrations of PVA (used as diluent) using rod 26. (b) Images of beads that were cured under the presence of a vertical magnetic field, resulting in the visible vertical chains within the PDMS beads. (c) Beads that were not	

cured under the presence of the vertical magnetic field, resulting in the visible horizontal chains embedded in the PDMS beads. (d) Dispersed beads (10 wt% MNPs) interacting with the beads in the coating which are notably of the same size and structure .....131

**Figure 4.3** Overview of the 3D-printing homocomposite technique used for shaping the structures from our chained PDMS beads. (a) Schematic of our 3D printing technique. The capillary paste is composed of the chained beads bridged together by PDMS. (b) An example of the 3D printing of one of the structures printed using this technique. (c) Schematic of the capillary paste composition. (d) Microscopy image of the cured capillary paste in a 3D printed structure .....133

**Figure 4.4** 3D printing the structures involved MATLAB coding of desired structures. (a) MATLAB code projection of holey wheel structure (left) and actual printed structure on disposable rheometer plate (right). (b) MATLAB code projection of grid circle structure (left) and actual printed structure on disposable rheometer plate (right). (c) Example of what part of the code looked like for the grid circle structure .....134

**Figure 4.5** (a) 3D printed rectangle used to study the magnet interaction of the chained beads within two printed lines. (b) 3D printing of dog bone shape demonstrated the versatility of this technique in that although we typically only printed one layer of material, we could deposit vertically at least up to 30 layers without the structure collapsing .....136

**Figure 4.6** Microscopy images of selected examples of printed lines with different loading amounts of embedded MNPs in the ink. (a) A 3D printed filament with 1 wt% embedded MNPs (left) and a cross section of the filament showing little magnetic material and no visible magnetic chains within the beads (right). (b) A 3D printed filament with 2.5 wt% embedded MNPs (left) and a cross section of the filament showing clearly visible magnetic chains within the beads. This was our final chosen loading amount (right). (c) A 3D printed filament with 5 wt% embedded MNPs (left) and a cross section of the corresponding filament showing slightly visible magnetic chains within the beads (right). (d) A 3D printed filament with 10 wt% embedded MNPs (left) and a cross section of the same filament (right). The filament is too dark and therefore the beads are no longer visible .....139

**Figure 4.7** The thickness of a 3D printed structure can be easily tuned by varying the pressure during extrusion. Once the minimum pressure for extrusion is reached, increasing the pressure further results in thicker printed lines. (a) A mesh printed at 50 psi and (b) a mesh 3D printed at 100 psi. The magnetic interaction of unchained beads with the 3D structures was also briefly investigated using microscopy. (c) Shows the unchained beads (example circled in red) interacting with the chained beads within the printed

structurer (circled in green). (d) A suspension of unchained beads interacting with the printed line in a non-structured way .....141

**Figure 4.8** The 3D printed line with the selected 2.5 wt% MNP and 6:4 composition and its interaction with a suspension of 5 wt% chained beads. (a) Microscopy images showing the morphology of the printed line and, specifically, visible chained beads within the printed structure. (b) A suspension of 5 wt% chained PDMS beads magnetically interacting with a single printed line. (c) A suspension of 5 wt% chained PDMS beads interacting between two 3D printed lines, demonstrating bridging behavior expanding from one printed structure (top) to the other (bottom). (d) A suspension of 5 wt% chained PDMS beads interacting with a printed structure after having been magnetized, showing more structured or aligned magnetic interaction. (e) A suspension of 5 wt% chained PDMS beads interacting with a printed structure with no prior magnetization after curing, showing more flexible branched structures composed of the chained beads .....143

**Figure 4.9** (a) A suspension of 5 wt% chained PDMS beads forming a percolation network that expands through the whole area within two printed lines (top) and a closer view of the chained beads in suspension interacting with the top line (bottom). (b) 5 wt% chained PDMS beads in suspension being exposed to a rotating field ( $H=16$  mT). Although the percolated network of beads are partially disrupted when responding to the rotating field, they almost immediately re-form once the field is removed and the beads re-align (top) The beads appear to individually respond to the applied rotating magnetic field but stay approximately in the same position (bottom) ..... 145

**Figure 4.10** Systems of chained bead suspensions of varying MNP concentration located within two 3D printed lines being magnetized, demagnetized and re-magnetized. (a) Suspension of 2.5 wt% chained beads magnetized and placed in between two printed lines, demonstrating bridging behavior and a percolation network (left). The same system after being subjected to a demagnetizing field, showing the chained beads no longer interacting with each other (middle). The same system once it was re-magnetized, resulting in the recovery of the percolation network of beads expanding the whole space within the printed lines. (b) 5 wt% chained beads show thicker aggregates within the percolated network. (c) 10 wt% chained beads showed even thicker chained bead aggregates in both magnetized (left) and re-magnetized (right) cases. The demagnetized system also does not appear to have been fully de-magnetized (middle) ..... 148

**Figure 4.11** (a) A schematic of a sample of the chained beads would interact with the printed structure on the rheometer plates. (b) A frequency sweep of a suspension of 2.5 wt% chained beads using a grid circle shaped 3D printed structure on the rheometer plate. (c) A frequency sweep of a suspension of 2.5 wt% chained beads using the traditionally used sandpaper on the rheometer plate (d) A frequency sweep of a suspension of 2.5 wt% chained

	beads using a wheel shaped circle 3D printed structure on the rheometer plate.....	150
<b>Figure 4.12</b>	Demonstration of the durability and flexibility of the printed anchor sites. (a) Shows what the wheel shaped magnetic anchor site looks like after taking two sample measurements. Intermittent cleaning was done to ensure anchors were only measuring the current sample. (b) Shows the 3D printed wheel anchor remains in one piece and in good condition after running two separate samples on it .....	151
<b>Figure 4.13</b>	(a) 3D printed mesh structure composed of 10 wt% NdFeB microparticles embedded in PDMS beads being bridged by PDMS and (b) a microscopy image of the morphology of a sample that was not magnetically aligned during curing. (c) Microscopy images of 3D structures that were cured under a magnetic field ( $H=1\text{mT}$ ) with the left showing that the NdFeB microparticles are embedded in the structure and the right image showing the NdFeB particles resembling magnetic cilia .....	152
<b>Figure 4.14</b>	Overview of other 3D printed magnetic structures demonstrating the vast possibilities enabled by the method. These structures include (a) a butterfly (b) a mesh (c) a diamond structure .....	154
<b>Figure 5.1</b>	Demonstration of applying an electromagnetic field to our chained beads system rather than the static magnetic field using a permanent magnet. (a) Schematic of the set up of the electromagnetic field with the sample of emulsified, but not yet cured, chained beads. (b) Microscopy image of 2.5 wt% chained beads in suspension cured after applying electromagnetic field of 0.51T. (c) Microscopy image of 2.5 wt% chained beads in suspension cured after applying an electromagnetic field of 0.84 T. (d) Compasses confirming that the orientation of the branched structures formed by the chained beads are in the direction of Earth's magnetic field for the beads cured using a 0.51T (left) and 0.84T (right).....	162
<b>Figure 5.2</b>	Drying pattern study of 2.5 wt% as well as 5 wt% magnetically aligned and randomly distributed MNPs in PDMS beads at 3 different concentrations of the magnetic beads to water, 6 wt%, 10 wt%, and 15 wt% at two different drying times, after 40 minutes and after the sample was fully dried. Red outline denotes chained beads samples and green outline denotes unchained beads or beads with randomly distributed MNPs .....	164
<b>Figure 5.3</b>	Microscopy images of a mixed suspension of 5 wt% magnetically aligned beads and 5 wt% randomly distributed PDMS beads.....	165
<b>Figure A.1</b>	Images highlighting other types of organic solvents that were used to try to disperse the Fe <sub>2</sub> O <sub>3</sub> MNPs and to reduce the viscosity of the PDMS Sylgard 184 base. As can be observed, only THF resulted in a MNP dispersion .....	171

**Figure A.2** Microscopy images of (a) 20 wt% Fe<sub>2</sub>O<sub>3</sub> MNPs embedded in PDMS beads and (b) 30 wt% Fe<sub>2</sub>O<sub>3</sub> MNPs embedded in PDMS beads. At 30 wt%, we begin to see smaller PDMS beads and what appears to be residual magnetic material in the cured sample before cleaning the beads. This means that all of the magnetic material is no longer being embedded into the PDMS beads. (c) At 40 wt% MNPs in the PDMS bead, there is a considerable amount of magnetic material left in the chamber as denoted by the darker filament like structures in the blue spatula above. This leads us to conclude that this percentage exceed the loading threshold .....172

## CHAPTER 1

### Assembly of responsive particle structures by magnetic and capillary interactions

#### 1.1 Introduction

This Chapter aims to highlight the foundational knowledge needed to better understand our motivation for studying the assembly of responsive particle structures by magnetic and capillary interactions. To that end, this chapter provides a review of current and previously used synthesis methods, types of particles, their interactions and materials that can be assembled from these particles. We have chosen to highlight key recent research achievements involving dispersed magnetic particles, magnetic particles embedded in a matrix, patchy particles, magnetically responsive foams, gels and coatings, and 3D printing of magneto-capillary pastes. These systems are exemplified graphically in Figure 1. The major capabilities and source of the fundamental science interest in these systems are a function of their response and re-arrangement in external magnetic fields. By tuning the strength and configuration of the applied magnetic field to the system, the magnetic interactions, dynamics and structure system can be precisely controlled. By introducing an external magnetic field, researchers can manipulate the orientation of the magnetic material, its colloidal interactions and potentially novel complex structures in a controlled manner.

Combining the magnetic interactions with capillary forces provides another convenient tool to control and manipulate particle structures. The capillary forces are characterized by very long range and directionality, which depend on the configuration of the multiphase (liquid-air, or liquid-liquid) system that wets the particles and generates the capillary forces. The capillary attraction is also unique with the family of forces used in colloidal assembly in that it does not lead to irreversible adhesion of the particles and allows their re-configuration even when strongly held together by the capillary menisci. For the purpose of this dissertation, capillary interactions are

used in combination with magnetic interactions to synthesize magneto-capillary gels and suspensions and will be discussed in great detail in Chapters 2-4 of this dissertation.

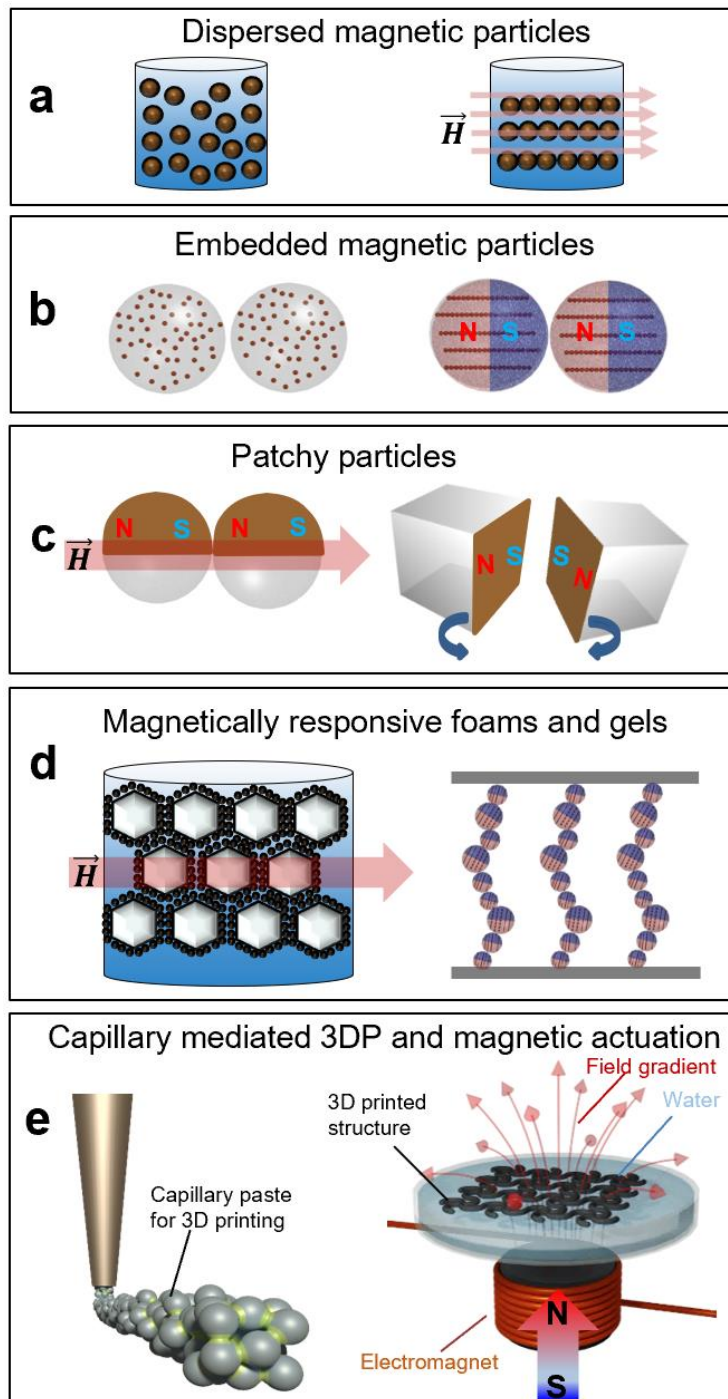


**Figure 1.1** Highlights of the topics and the focus of the introductory chapter: (a) Systems with dispersed magnetic particles, (b) Systems with embedded magnetic particles, (c) Interactions and assembly of patchy particles, (d) Making and properties of magnetically responsive foams, gels, and coatings, and (e) Capillary-mediated 3DP and magnetic actuation of soft matter.

## 1.2 Dispersed magnetic particles

Perhaps the most commonly used method for studying magnetic colloidal interactions and assembly is based on magnetic particles in suspension. The interactions induced in freely suspended particle systems are predominantly attractive. Having dispersed the magnetic material, typically nano- or micron-sized, in a non-magnetic fluid, such as silicone oil or a fatty acid, allows for remarkable tunability.<sup>1</sup> The magnetic material is usually composed of carbonyl iron,  $\gamma$ -Fe<sub>2</sub>O<sub>3</sub>, Fe<sub>3</sub>O<sub>4</sub>. Another advantage of these types of magnetically responsive systems is that by introducing an external magnetic field, the suspension can transition from liquid-like to solid or gel-like due to the magnetic particles' reorientation and structure formation driven by the applied field.<sup>1</sup> This type of response could find applications in a variety of research and industrial fields in order, e.g., to make units such as shock absorbers, or to assist in drug delivery.

A well-known example of a system comprising magnetically manipulated particles in suspension are magneto-rheological (MR) fluids.<sup>1</sup> An MR fluid can be composed of common types of magnetic material such as carbonyl iron. One composition improvement that can be done to a MR fluid is to incorporate magnetic nanoparticles as an additive in order to enhance not only the magnetic response of the system, but to stabilize it as well. One of the many reasons why a MR fluid may be favored in applications over other types of responsive fluids such as electrorheological fluids (ER) is that the yield stress of MR fluids is typically great than that of ER ones, meaning that MR fluids could be more widely applicable. Kim et al. looked at increasing concentrations of Fe<sub>2</sub>O<sub>3</sub> in a carbonyl-iron based MR fluid. By incorporating the Fe<sub>2</sub>O<sub>3</sub> component, they have been able to observe an increase in the saturation magnetization of their system as well as a decrease in sedimentation. This trend improved even more as the amount of added nanoparticles increased. They have also observed a transition in their system to gel-like matter

once a magnetic field was applied. The strength of this gel increased as the amount of magnetic nanoparticles increased, likely due to the increase in gap-filling by the Fe<sub>2</sub>O<sub>3</sub> nanoparticles.

Other groups such as Wang et al. and He et al. were able to successfully tune the optical properties of magnetic nanoparticle systems in the visible and infrared spectrum by taking advantage of the reorientation of their nanostructures in the direction of an applied magnetic field.<sup>2,3</sup> The first group studied this topic with the goal of applying the optically tuned magnetic material to technology areas such as sensors and anti-counterfeiting devices whereas the latter group proposed applying their findings to humidity sensing and structural color printing.

Magnetic suspensions may also serve as building blocks for more complex 3D systems such as photonic colloidal crystals. By coating colloidal nanocrystal clusters with silica, one can use nonaqueous media such as alcohol solvents to have the clusters self-assemble into ordered structures in the presence of an applied external magnetic field.<sup>4</sup> Silica-coated magnetite core-shell nanoparticles have also been studied by many researchers, including a group that focused on characterizing and comparing the colloidal crystallization in the presence and absence of an external magnetic field.<sup>5</sup> Industries such as those focused on displays and sensors could benefit from the tunability presented in the two types of systems presented above. Another sophisticated way to design and manipulate the properties of magnetic particles in suspension is to incorporate DNA linkers to chains of paramagnetic particles such as that studied by Byrom et al.<sup>6</sup> DNA fragments of varying sizes were used to link magnetic particles. By varying the field strength, these researchers have been able to control the magnetic particle chain flexibility and interparticle spacing.

Previous research has also included end-functional polymers used to prepare shell-stabilized, polymer-coated magnetic particles such as polystyrene-coated cobalt nanoparticles cast

in the form of one-dimensional structures.<sup>7</sup> Moreover, computational studies have also been conducted to better understand and predict the self-assembled states of paramagnetic nanoparticles' response to an applied magnetic field by taking into account the mutual polarization of the nanoparticles.<sup>8</sup>

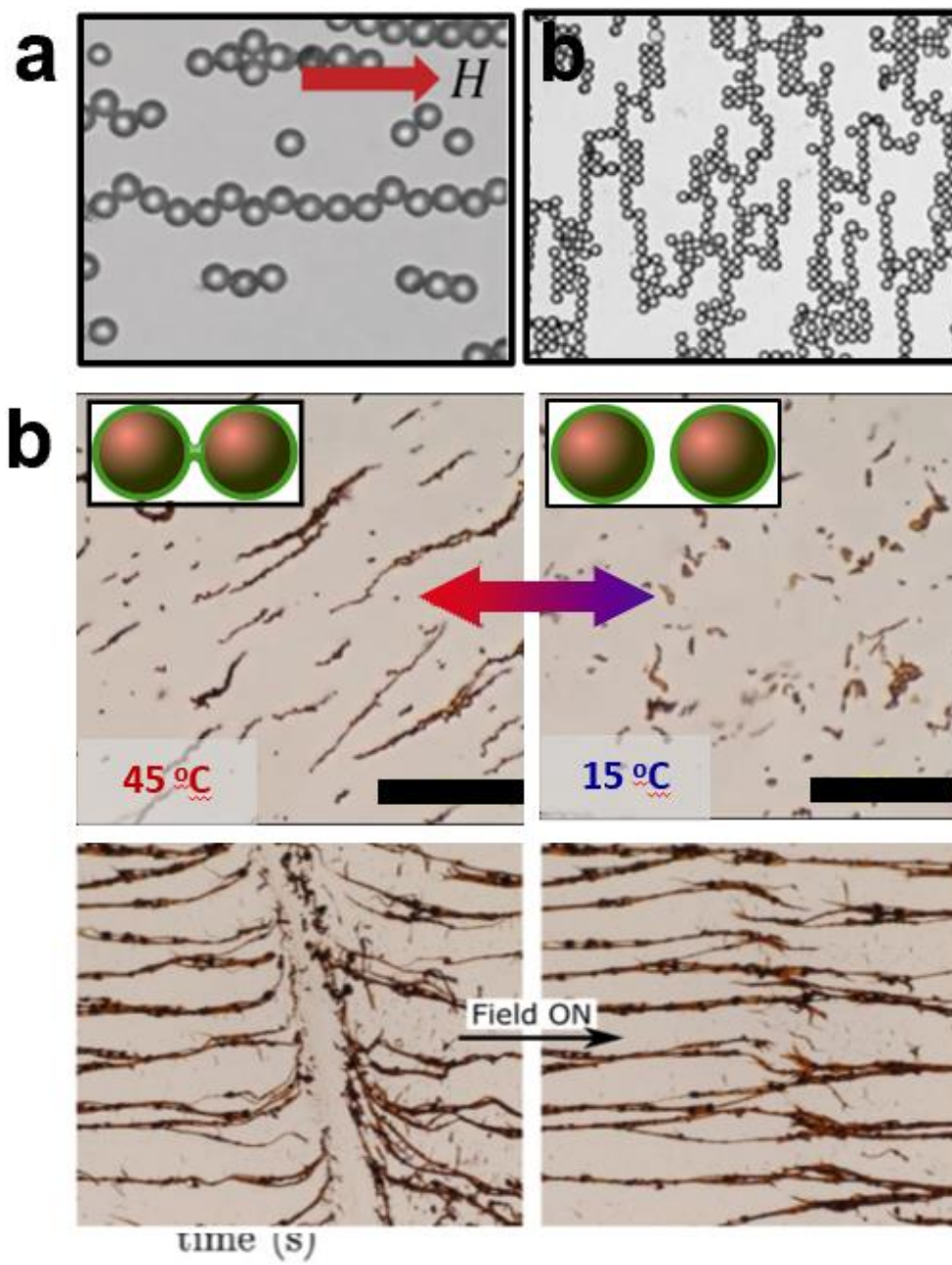
Our research group has investigated numerous types of systems with magnetic interactions and has looked extensively at the dynamic response of the dispersed magnetic material, specifically under complex magnetic fields. Some of this work is highlighted in figure 1.2a. Here we present partially staggered chains of superparamagnetic nanoparticles formed in the direction of an applied uniform magnetic field.<sup>9</sup> In order to obtain multi-directionality within the magnetic particle dispersions, our group also simultaneously applied an alternate current electric field and a uniform magnetic field. In earlier published work, we were also able to demonstrate double induced dipole particles at low and high packing fractions. In a more dilute system, the particles arrange themselves in long chains in the applied field direction, giving rise to “T” shaped and “Y” shaped connections. In a more concentrated system, the staggering of particles along the chain of particles in the direction of the applied field become more pronounced and the overall percolation network becomes more complex.<sup>10</sup> This results in two-dimensional, anisotropic networks of cross-linked chains (Figure 1.2b). By having particles with double dipoles, we were able to reach a few staggered conformations. We were able to confirm our results with computer simulations of our system.

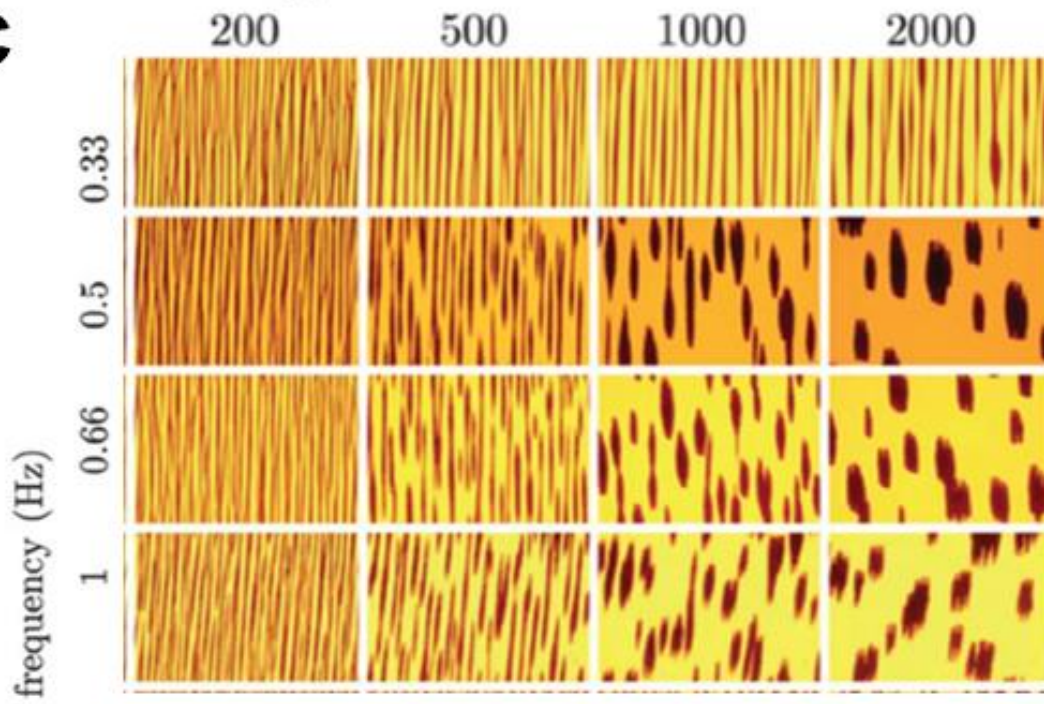
Another soft matter system introduced by Velev group is lipid coated  $\text{Fe}_2\text{O}_3$  magnetic nanoparticles suspended in water, where we investigated the linear chains and clusters formed under an applied external magnetic field (Figure 1.2c).<sup>11</sup> Through this research, our group was able to demonstrate that under the presence of a uniform magnetic field, the assembled lipid-bound

microfilaments have unprecedented flexibility as well as self-healing properties that enabled a repaired filament to remain in one piece even after the removal of the applied field. This was due to the lipid capillary bridges between the nanoparticles, which were able to reform and self-repair the filaments in the presence of the applied magnetic field. Once we introduced more complex fields such as a rotating magnetic field, we were able to use the magnetic response of our system to form different structures such as stretched, bent, and bundled filaments that could give rise to a variety of unusual shapes such as a ring, an infinity sign, a square, and a heart-like structure. Furthermore, other groups have shown how many hierarchical colloidal assemblies from superparamagnetic colloids such as 2D assembly networks and clusters as well as 1D assembled chains can be obtained both in time-varying and static magnetic fields.<sup>12</sup>

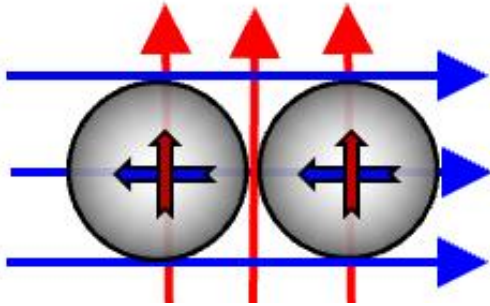
Swan et al. studied polystyrene latex beads embedded with iron oxide magnetic nanoparticles in such a way that the magnetic moments were randomly oriented dispersed in water.<sup>13</sup> They looked at these highly polarizable beads under toggling magnetic fields and therefore studied the depercolation and crystallization of their system depending on the frequency of their chosen applied field strength. They were able to show that a uniform pulse field could be used to overcome the kinetic constraints typical of strong dipolar interactions and instead self-assemble a suspension of their beads into condensed crystalline domains. Magnetic particles can have complex fields applied or the particles themselves can be complex particles such as patchy particles (Figure 1.2d). Large progress in understanding the physical mechanism of particle assembly in static and dynamic external fields has also been performed by researchers such as the work highlighted in Figure 1.2c.<sup>13</sup>

**Figure 1.2** Examples of dispersed magnetic particle systems. (a) Superparamagnetic particles align in the direction of the applied magnetic field (left). Microscopy images of 5  $\mu\text{m}$  induced “double” dipole superparamagnetic particles showing staggering branched formation at high concentrations due to the applied complex (electric and magnetic) fields (right). (b) A temperature dependent, fatty acid-coated nanoparticle filament system that can use capillary force to form capillary bridges between the magnetic nanoparticles at higher temperatures that break apart at lower temperatures. This nanoparticle system also has magnetically assisted self-repairing properties.<sup>11</sup> (c) Microscopy images highlighting the evolution of the suspension percolation after having a pulsed magnetic field applied for varying lengths of time at varying applied pulse frequencies.<sup>13</sup> (d) Magnetic particles can undergo complex fields such as a combination of magnetic and electric fields (left). Complex particles such as Janus particles can also have complex interactions due to their differing hemisphere composition.

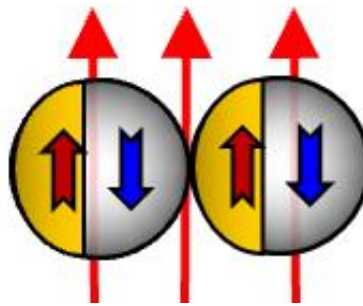


**c****d**

Complex fields



Complex particles



### 1.3 Responsive soft materials with embedded magnetic particles

Magnetic field-directed self-assembly is a convenient tool for making directionally responsive structures for a number of fields such as soft robotics and biomedical applications because it is contact free and highly tunable<sup>14</sup>. Two commonly used methods for embedding magnetic particle assemblies in soft polymer media include solvent casting and bulk polymerization.<sup>14</sup> By assembling magnetic nanoparticles and microparticles from suspension and incorporating the assemblies into more complex materials such as a polymer matrices, one is able to yield permanent materials with more advanced functions and applications. Furthermore, stability can be improved by decreasing the possibility of aggregation or the degree of sedimentation of a system, particularly for spherically shaped polymer particles.<sup>15</sup>

Our group has also incorporated magnetic nanoparticles inside the matrix of polydimethylsiloxane (PDMS) spherical beads.<sup>16</sup> By using a scalable emulsion technique, we were able to synthesize soft microbeads with either randomly dispersed (bead type 1) or magnetically aligned (bead type 2) embedded  $\text{Fe}_2\text{O}_3$  nanoparticles. Suspensions of these two types of beads demonstrated widely different magnetic and rheological properties based solely on the orientation of the fixed nanoparticles. By looking at the suspensions under the microscope, we found that the beads with randomly oriented nanoparticles demonstrated little interaction in the absence of a magnetic field. When a magnetic field was applied, the beads interacted and aligned in the direction of the applied field, however, these aligned structures immediately broke apart once the field was removed. The beads with chained nanoparticles, on the other hand, formed aligned structures at dilute concentrations and formed percolated networks at high concentrations even in the absence of an external magnetic field. In the presence of a magnetic field, the magnetically aligned beads formed more structured percolated networks in the direction of the

applied field. Moreover, these beads were able to quickly reform these percolated structures, even if the system was disrupted. The beads with chained magnetic nanoparticles had permanent magnetic dipoles and demonstrated gel-like properties. These systems are described in more detail in Chapter 2 of this thesis.

The physical understanding of the response of particles in dense, viscous or gelled dispersions necessitates a better understanding of the structure for effective quantification and characterization of the system. Shroyen et al. pointed out that optical microscopy and scattering methods may not be sufficient for all materials and that other methods such as electron microscopy involve much preparatory work and may be limiting in terms of the obtained information. They looked at partially dispersed suspensions at intermediate to higher particle loadings, including highly viscous matrices, and they were thus able to show that high frequency rheometry can be used to quantify dispersion quality using a home-built piezo shear rheometer.<sup>17</sup>

Schmauch et al. used solvent casting in order to obtain an elastomer film containing magnetically aligned, magnetic microparticles, which were chained by applying an external magnetic field (Figure 1.3a).<sup>18</sup> Since this alignment results in anisotropic magnetic properties in the composite, an anisotropic magnetic response can be obtained.<sup>14</sup> By controlling the alignment of the microparticles embedded in the film, they were able to directionally tune shape transformations of the matrix into shapes such as lifting arms” in a cross-shaped structure as well as in accordion-shaped structures (see Figure 1.3a).<sup>14,18</sup> These soft actuator cantilevers have been able to lift up to 50 times the mass of the polymer matrix, paving the way for various soft robotics applications.

Varga et al. present magnetic field sensitive functional elastomers with tunable elastic modulus. This research group studied the effect of an external magnetic field on the elastic

modulus of magnetically aligned chains embedded in elastomers <sup>19</sup> (Figure 1.3b). Their system was composed of poly(dimethyl siloxane) networks loaded with either magnetically aligned carbonyl iron particles or randomly oriented carbonyl iron. They were able to determine that the networks with aligned magnetic particles exhibited larger excess moduli compared to that of the randomly oriented magnetic particle networks in the presence of an applied external magnetic field. They were able to observe that their magneto-elastomer networks showed a 20% increase in elastic modulus as compared to that of the magnetically aligned particle network.

Another advance in actuated structures has been reported by Zhang et al., who have introduced a bottom-up assembly-based small-scale 3D soft-bodied machines that respond to an external stimulus, specifically an externally applied magnetic field. <sup>20</sup> They have been able to fabricate their microscale building blocks or “voxels” using a 3D heterogeneous integration approach in order to form much more complex shapes by taking advantage of the magnetic response brought about by the complex structure (Figure 1.3c) They have so far demonstrated that these machines can be used in biomedical applications because they were able to show that live stem cells were able to be carried and spread within the voxels in cell cages without noticeable toxic effect or cell death.

Kim et al. presented polymeric nanocomposite microactuators which could be manipulated using heterogeneous, programmable magnetic anisotropy in order to allow for shape control and complex actuator motion (Figure 1.3d). <sup>21</sup> Active or smart materials offer the advantage of sophisticated movement control and magnetically activated microdevices, in particular, can be controlled without the need of direct physical contact. Furthermore, being able to pattern multiple magnetic moments with different directions in a microstructure enables even greater tunability of the system. For this reason, magnetically anisotropic superparamagnetic materials make multi-

directional movement possible. By patterning each section of a four-piece polymerized resin structure to be aligned in a different direction using photopolymerization, these authors were able to present an actuator with snake-like recoil under the presence of an external field. This is due to the fact that the homogenous magnetic field is able to independently actuate each individual section based on the initial embedded magnetic particle alignment.

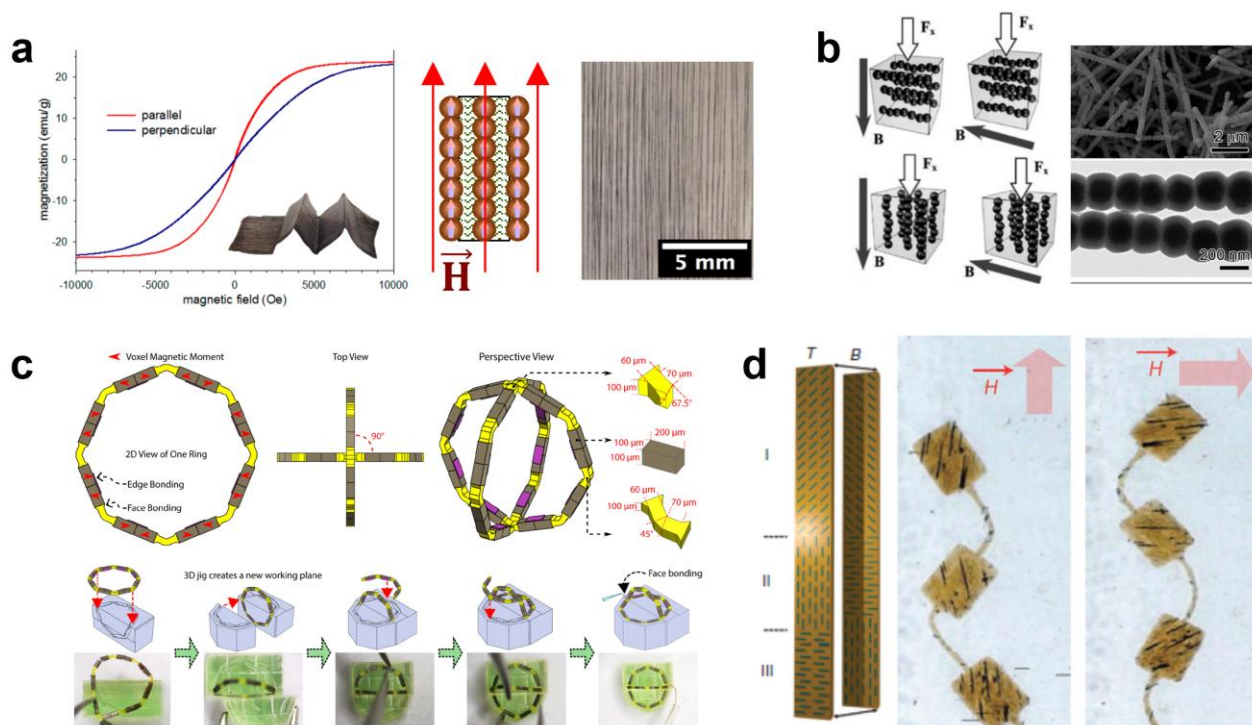


**Figure 1.3** Examples of magnetically embedded smart materials including (a) magnetically aligned embedded particles in elastomer films<sup>18</sup> (b) magnetically aligned and embedded particles in an elastomer matrix,<sup>19</sup> (c) microscale building blocks or “voxels” whose magnetic response is controlled by its complex structure<sup>20</sup> (d) polymeric nanocomposite actuators with heterogeneous magnetic anisotropy.<sup>21</sup>

## 1.4 Magnetic interactions and structures from anisotropic colloidal particles

Anisotropic colloidal particles are rapidly gaining research attention due to the large diversity of systems that can be synthesized and applied in directed assembly of such particles. Anisotropy can originate from particle shape but can also be a result of surface modification. Particles whose surface is patterned in a way that allows for programmed direction and selective interactions can find application in a variety of fields involving colloidal assembly.<sup>22</sup> Patchy particles, most commonly being particles with a single magnetic hemisphere also known as “Janus particles”, have gained interest in recent years because of their potential in building hierarchical structures for both fundamental and industrial applications.<sup>23, 24</sup> These particles can vary in size from 100 nm to 100  $\mu\text{m}$  and are being widely studied both experimentally and computationally.

Magnetic nanoparticles can be added to a particle that is already a non-magnetic patchy particle by adsorbing selectively onto one side of the patchy particle. This technique takes advantage of the particle’s differentiated surface properties. A magnetic component can also be introduced by depositing a thin magnetic film. An additional magnetic material can be incorporated in the patchy particle by adding a large single magnetic particle or a colloidal supraparticle. These elements could be embedded in the non-magnetic sphere, effectively slightly altering the particle shape. In Figure 1.4c, a sol-gel reaction is conducted in a mini-emulsion such that the nanoparticles are dispersed inside an organosilica “head” attached to a polystyrene “body,” producing one-patch magnetic polystyrene particles with a snowman-type shape.<sup>22</sup>

Our group has supplemented magnetic interaction with capillary bridging for assembling clusters of patchy particles.<sup>25</sup> By using selective metal vapor deposition, followed by lipid layer adsorption on the oxidized metal patches, we made lipid-patched polystyrene (PS) microspheres. We were able to modify the shape, iron-patch size, and the orientation of the particles by adjusting

the angle of deposition. By tuning these properties, we were able to successfully control the complex directional interactions between the particles, leading to clusters with varying morphologies that could serve as building blocks for complex structures. We performed Monte Carlo simulations to confirm the observed morphologies (Figure 1.4a).

The Velev group has also conducted microscale self-assembly to synthesize non-spherical microbot microclusters comprised of patchy magnetic cubes.<sup>26</sup> This was done by applying intermittent external magnetic fields using collinear pair of electromagnets. These clusters are considered patchy particles because one face of the microcube was selectively coated with cobalt film. Thus, when an external field was applied to a suspension of randomly dispersed microcubes, the magnetic patches acquired a dipole which led to cube chain assembly parallel to the applied magnetic field. In essence, the metal coated face acted as a structural director for the microcube assembly. As seen in figure 1.4b, the microcube chains demonstrated unusual dynamic rearrangement of the assembled chains into bundled or partially wrapped configurations every time the field was turned on or off. The ability of such soft robotic devices to reconfigure on-demand has great potential to leading to novel microrheometers or microswimmers for biological applications.

Other research groups have recently also studied magnetic soft micromachines composed of linked microactuators.<sup>23</sup> By using a two-photon polymerization system, they were able to apply 3D magnetic fields to their system to control the location of the microactuators and thus form the linked microactuator network. These microactuators were composed of Janus particles with a hemisphere being silica and the other hemisphere being polyethylene glycol (PEG) coated Au. By taking advantage of the anisotropy of the particles and the magnetic response they possessed, the research group was able to actuate these particles in complex ways.

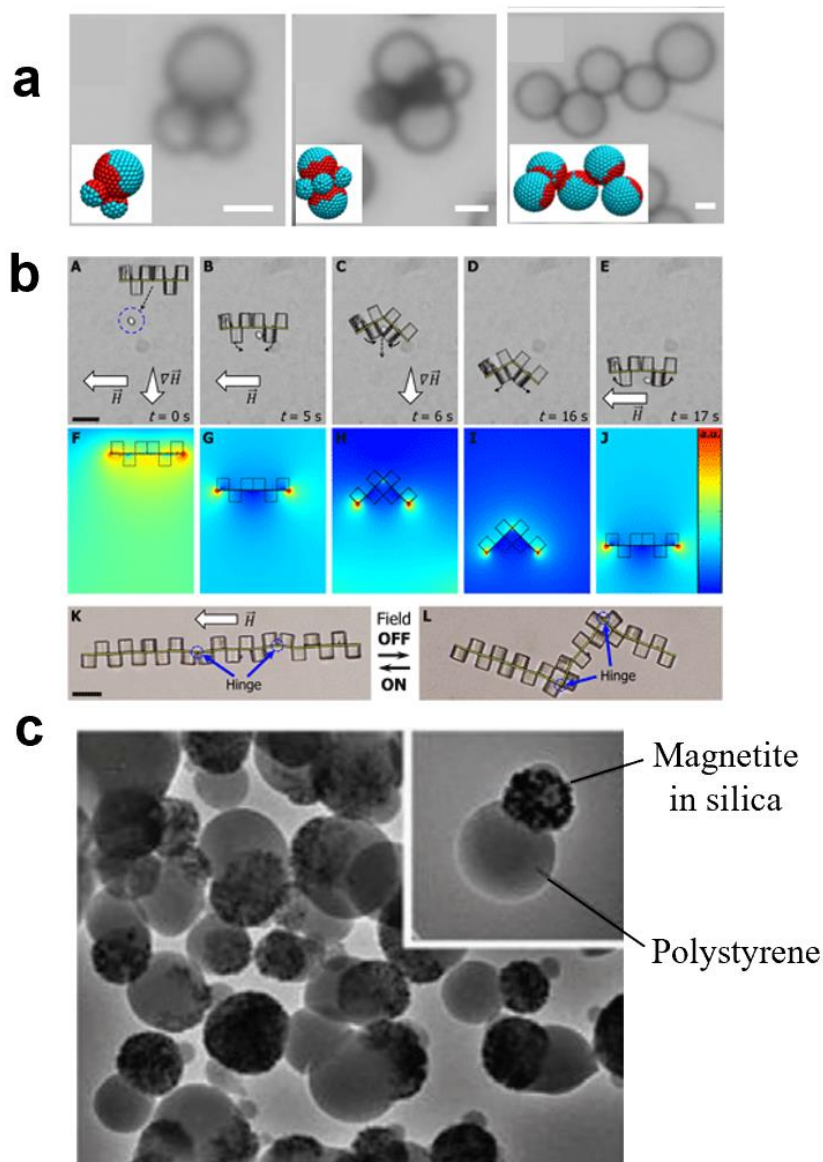


**Figure 1.4** Examples of patchy particles including Janus particles, microbots, and snowman shaped polystyrene/magnetite particles. (a) Magnetic interaction coupled with capillary bridging is used to assemble clusters of patchy particles and Monte Carlo simulations are performed to prove observed morphologies.<sup>25</sup> (b) Microscale self-assembly is used to synthesize non-spherical microbot microclusters comprised of patchy magnetic cubes with the corresponding COMSOL simulations<sup>26</sup> (c) A sol-gel reaction in a mini-emulsion produces one-patch magnetic polystyrene particles with a snowman-type shape<sup>22</sup>

## 1.5 Magnetically responsive foams, gels, and coatings

Fameau et al. introduced the first multi-stimuli responsive foams with thermo-photo-magneto-tunable stability.<sup>27</sup> Foams are typically thermodynamically metastable, therefore stability improvement and external manipulation are essential for any desired applications. By tuning a response with an external stimulus, one can reduce the need for additives such as chemical defoamers which would reduce chemical pollution. In order to get a thermo-photo-magnetic response, magnetic carbon black particles were added to the foam along with a thermoresponsive fatty acid. These particles are intense light absorbers that in turn result in a rise in temperature and can be manipulated by adding light and a magnetic field. Our group was thus able to destabilize the foam alternatively by either introducing light or by applying an external magnetic field. Since fresh foams have a higher weight content than aged foam samples, the movement of the magnetic particles did not result in foam breakdown whereas the aged foam samples would collapse readily under the presence of the magnetic field (Figure 1.5a).

Lee et al. present another method of programming the assembly of nonmagnetic colloidal particles dispersed in a ferrofluid by taking advantage of the ferrofluids' response to an external magnetic field.<sup>28</sup> The researchers allow the binary mixture of anionic surfactant coated-  $\text{Fe}_3\text{O}_4$  nanoparticles and surface-modified fluorescent polystyrene latex beads to partially dry before applying a uniform magnetic field. The remainder of the drying process is done in the presence of the magnetic field, which is applied in the direction normal to the plane containing the three-phase contact line of the droplet. By allowing the droplet to partially dry before applying the field, there is an initial migration of nanoparticles with average zero magnetic moment towards the edge of the droplet, creating a particle-rich state, which is then essentially reversed as the particles align in the direction of the applied field and migrate towards the center of the droplet. It should be noted

that after the removal of the field the nanoparticles continue to move towards the edge of the droplet. Through this magnetostatic micro convection technique, these authors could overcome the typical coffee ring drying pattern formation and instead are able to form functional surface coating (Figure 1.5c).

Magnetorheological gels (MRG) have also gained research interest due to their potential applications in sensors, magnetoresistors, brakes, vibration control, damping devices, and other electrical devices.<sup>29</sup> Structurally, MRGs can be considered as an intermediate of magnetorheological fluids (MRFs) and magnetorheological elastomers (MREs). This is largely because gels are more liquid-like than the solid elastomer matrices and allow for magnetic particle assembly, but they are also not as free flowing as in magnetorheological fluids. Castellanos et al. (Figure 1.5b) introduced magnetic-field induced gels composed of magnetically embedded and aligned  $\text{Fe}_2\text{O}_3$  nanoparticles in a PDMS bead matrix. This system's gel-like properties were observed microscopically by the presence of percolation network formation (see Figure 1.5b) and confirmed using rheology. Furthermore, in a yet unpublished work, Castellanos et al. have been able to successfully combine the magnetic and capillary interactions of magnetically embedded silicone beads or nanoparticles dispersed in fatty acid to form magnetically responsive capillary gels. Research conducted by Yu et al. showed that the magnetoresistance of their synthesized magnetorheological gels could be reversibly controlled by introducing a magnetic field.<sup>29</sup> These gels were composed of dispersed carbonyl iron particles in polyurethane gel matrix. Lalitha et al. presented the design and synthesis of stimuli responsive self-healing gels composed of renewable resources. They incorporated magnetic nanoparticles ( $\text{Fe}_3\text{O}_4$ ) by sonicating them into the gel matrix to make it magnetically responsive and were able to demonstrate successful self-repair of the gels both in air and water medium.<sup>30</sup>

Biodegradable magnetic polymer gels have also been studied by Chatterjee et al.<sup>31</sup> This research group used hydroxy propyl cellulose, a biopolymer commonly used in pharmaceuticals, and synthesized a nanomagnetic gel using an emulsion method. Magnetic particle distribution in magneto-anisotropic gels have also been studied using ferromagnetic resonance and a paramagnetic sensor technique.<sup>32</sup> Magnetic colloidal particles have also been embedded into a crosslinked polymer matrix<sup>33</sup> The end goal was to have them serve as model systems to investigate hyperthermal cancer treatment when magnetic particles are embedded into tumor tissue. Tarama et al. also demonstrate that the dynamic behavior of magnetic gels can be tuned by introducing an external field, through the magnetic particle distribution, and via magnetoelastic coupling.

Thermoresponsive magnetic colloidal gels have also been studied by researchers like Braim et al.<sup>34</sup> These researchers applied gels composed of PDEGMA/poly(chloromethylstyrene) microsphere and Fe<sub>3</sub>O<sub>4</sub> magnetic nanoparticles during successive rounds of 3D cell culture growth and separation. Their results showed good cytocompatibility with lab cells and could potentially be used as 3D scaffolds for *in vitro* expansion of cells and applications. In essence, magnetic foams, gels, and coatings can be used for a variety of fundamental, industrial, and biocompatible applications.

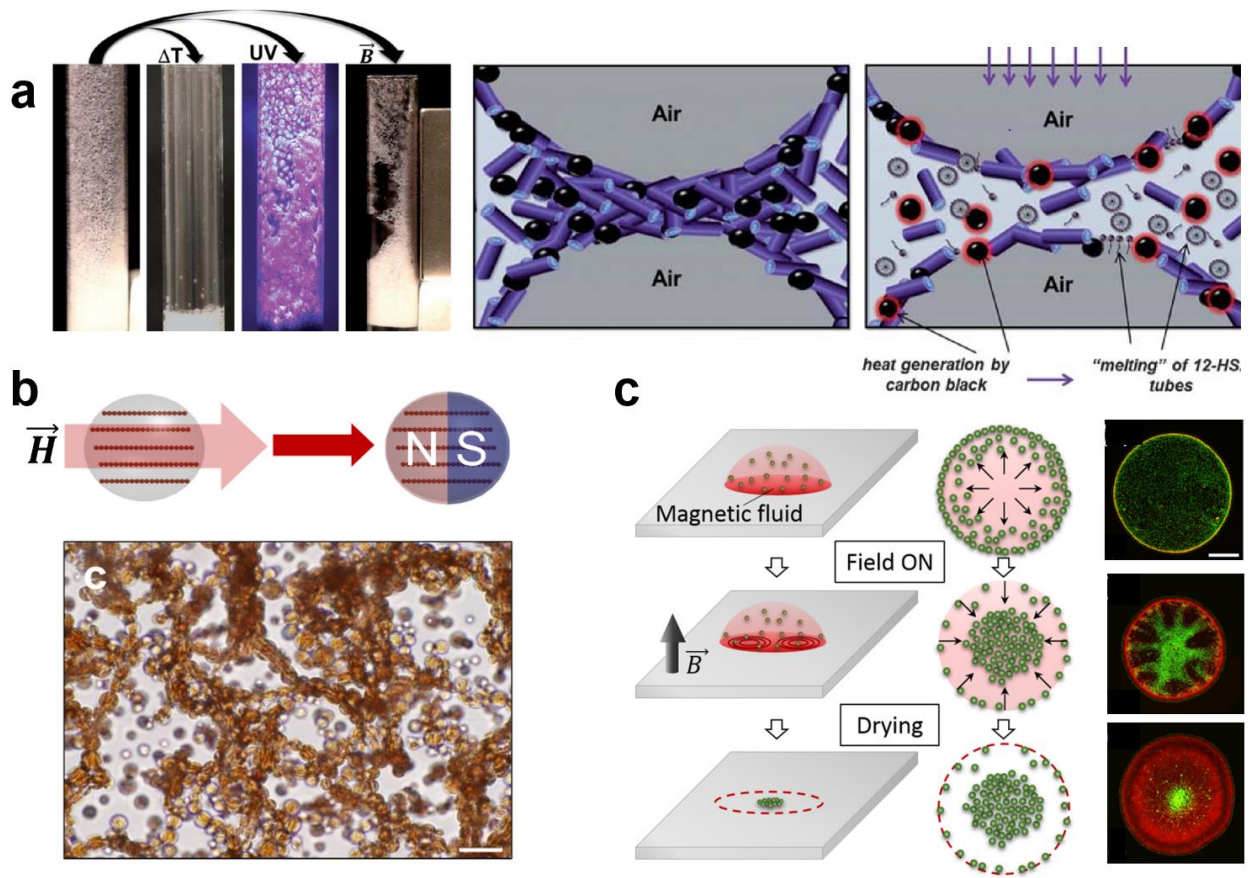


**Figure 1.5** Examples of a (a) thermophotomagnetic foam<sup>27</sup> (b) magnetic-induced gel<sup>16</sup> and a (c) magnetic field-driven coating.<sup>28</sup>

## 1.6 3D printing in magneto-capillary pastes

Capillary force is critical in the assembly of particles in that it is long ranged, can overcome repulsive electrostatic forces and is often larger than van der Waals forces, giving rise to materials that exhibit strong and cohesive structures. Previous research has shown that even a small fraction of immiscible secondary liquid can lead to capillary bridging between particles in a concentrated multiphase suspension.<sup>35-37</sup> In this way, the suspension can be transformed from a viscous fluid to a gel-like material due to a meniscus forming around the contact point between the particles, drawing them together and thus forming an elastic gel network. This can, understandably, result in dramatic changes to the rheological properties of a suspension. In particular, an increase in strength of materials can be observed with an increase in liquid content as long as the fluid remains confined in capillary bridges. Capillary force offers strong yet controlled binding and aggregation in a liquid medium meaning they exhibit highly reconfigurable and tunable properties by adjusting parameters such as temperature, wetting liquid properties, and particle size. This ability to tune the material properties is of interest in numerous fields such as biomedicine and soft robotics or for 3D printing materials such as capillary pastes<sup>38</sup>

Assembly of anisotropic particles by capillary interaction at fluid-fluid interfaces is of particular interest in making long-ranged 2D structures. Luwandowski et al. introduced work that focused on particle shape anisotropy using contact lithography to create the contact line undulation.<sup>39</sup> They studied cylindrical particles with varying cross sections. Botto et al. later looked at the interactions and assembly of differently shaped particles such as colloidosomes, ellipsoids, “binoculars”, and bent circular disks.<sup>40</sup>

Our research group has developed a technique for 3D printing capillary pastes.<sup>41,42</sup> By using this technique, we can obtain homocomposite 3D printed architectures via an extrusion

technique. Furthermore, by incorporating magnetic nano- or microparticles, we are able to obtain a magnetic response. These printed structures can be applied to a variety of industries such as the biomedical field.

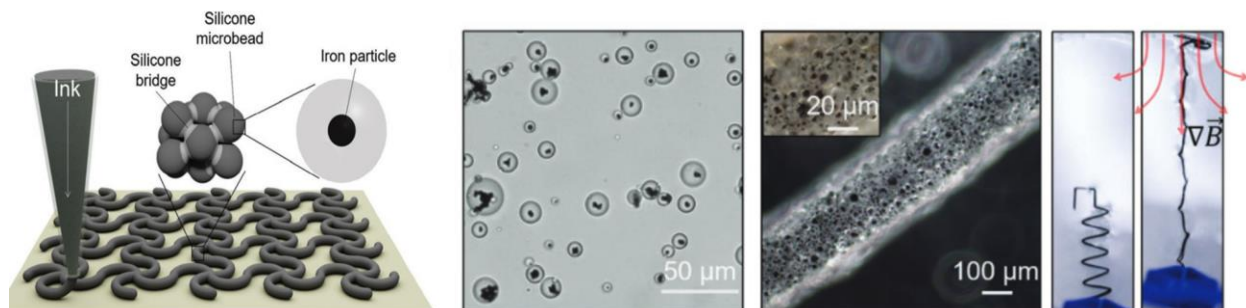


**Figure 1.6** Direct writing extrusion-based 3D printing of homocomposite magneto-capillary pastes previously introduced by the Velev group. <sup>41,42</sup>

## 1.7 Conclusions

The assembly of responsive particle structures by magnetic and capillary interactions is of scientific interest due to the rich variety of novel material structures that are encompassed by these two types of interactions and the large amount and variety of potential applications for these types of structures. Current research discussed above emphasizes the importance of studying these interactions, particularly as they pertain to dispersed magnetic particles, magnetic particles embedded in a matrix, patchy particles, magnetically responsive foams, gels and coatings, and 3D printing of magneto-capillary pastes. A large volume of research has already been conducted, however, the current research discussed also highlights the need for more work to ensure that the full potential of the magneto-capillary interactions is explored.

## **1.8 Dissertation Outline**

This dissertation provides the groundwork for the design, synthesis, and characterization of smooth spherical bead-based magnetically responsive gels and suspensions. In Chapter 2, we introduce the principles of the synthesis and characterization of the soft magnetic microbeads that form the basis of our studies. Our synthesis method was able to produce large batches of relatively monodisperse beads. We defined three distinct bead types, a control non-magnetic bead, a bead with randomly oriented embedded magnetic nanoparticles, and a bead with embedded magnetically aligned nanoparticles. Furthermore, we were able to observe key differences in the magnetic and physical network interactions of our magnetic beads depending on the placement of the embedded magnetic nanoparticles. In Chapter 3, we present the intersection of magnetic and capillary forces using our beads as building blocks for capillary-induced physical gels. We were able to observe physical differences in our gels depending on the location of the magnetic particles which were either embedded in the bead or dispersed in the capillary bridge. In Chapter 4, we discuss the application of our magnetically aligned microbeads in the 3D printing of magnetic, homocomposite structures used in magnetic anchoring for the improvement of the characterization of our magnetically aligned beads, specifically in rheological applications. Finally, in Chapter 5, we describe and summarize our findings as well as outline potential future research directions in this field of study.

## 1.9 References

1. Kim, M.W.; Han, W.J.; Kim, Y.H.; Choi, H.J. Effect of a hard magnetic particle additive on rheological characteristics of microspherical carbonyl iron-based magnetorheological fluid. *Colloids Surf.* **2016**, *506*, 812-820.
2. Wang, M. & Yin, Y. Magnetically Responsive Nanostructures with Tunable Optical Properties. *J. Am. Chem. Soc.* **2016**, *138*, 6315–6323.
3. He, L.; Yongxing, H.; Han, X.; Lu, Y.; Lu, Z.; Yin, Y. Assembly and Photonic Properties of Superparamagnetic Colloids in Complex Magnetic Fields. *Langmuir*, **2011**, *27*, 13444–13450.
4. Ge, J. & Yin, Y. Magnetically responsive colloidal photonic crystals. *J. Mater. Chem.*, **2008**, *18*, 5041–5045.
5. Pal, A. P.; Malik, V.; He, L.; Erne, B.H.; Yin, Y.; Kegel, W.K.; Petukhov, A. V. Tuning the Colloidal Crystal Structure of Magnetic Particles by External Field. *Angew. Chem. Int. Ed.* **2015**, *54*, 1803 –1807.
6. Byrom, J.; Han, P.; Savory, M.; Biswal, S.L. Directing Assembly of DNA-Coated Colloids with Magnetic Fields to Generate Rigid, Semiflexible, and Flexible Chains. *Langmuir*, **2014**, *30*, 9045–9052.
7. Korth, B.D.; Keng, P.; Shim, I.; Bowles, S.E.; Tang, C.; Kowalewski, T.; Nebesny, K.W.; Pyun, J. Polymer-Coated Ferromagnetic Colloids from Well-Defined Macromolecular Surfactants and Assembly into Nanoparticle Chains. *J. Am. Chem. Soc.* **2006**, *128*, 6562-6563.
8. Sherman, Z.M.; Ghosh, D.; Swan, J.W. Field-Directed Self-Assembly of Mutually Polarizable Nanoparticles. *Langmuir*, **2018**, *34*, 7117–7134.
9. Bharti, B.; Kogler, F.; Hall, C.K.; Klapp, S.H.L.; Velev, O.D. Multidirectional colloidal assembly in concurrent electric and magnetic fields. *Soft Matter*, **2016**, *12*, 7747-7758.

10. Schmidle, H.; Jager, S.; Hall, C.K.; Velev, O.D.; Klapp, S.H.L. Two-dimensional colloidal networks induced by a uni-axial external field. *Soft Matter*, **2013**, *9*, 2518-2524.
11. Bharti, B.; Fameau, A.-L.; Rubinstein, M.; Velev, O.D. Nanocapillarity-mediated magnetic assembly of nanoparticles into ultraflexible filaments and reconfigurable networks. *Nat. Mater.* **2015**, *14*, 1104-1109.
12. Spatafora-Salazar, A; Lobmeyer, D.M.; Cunha, L.H.P.; Joshi, K.; Biswal, S.L. Hierarchical assemblies of superparamagnetic colloids in time-varying magnetic fields. *Soft Matter*, **17**, *2021*, 1120 (1-37).
13. Swan, J.W.; Bauer, J.L.; Liu, Y.; Furst, E.M. Directed colloidal self-assembly in toggled magnetic fields. *Soft Matter*, **2014**, *10*, 1102-1109.
14. Mishra, S.R.; Dickey, M.D.; Velev, O.D.; Tracy, J.B. Selective and directional actuation of elastomer films using chained magnetic nanoparticles. *Nanoscale*, **2016**, *8*, 1309-1313.
15. Denkov, N.D.; Ivanov, I.B.; Kralchevsky, P.A.; Wasan, D.T. A possible mechanism of stabilization of emulsions by solid particles. *J. Colloid Interface Sci.* **1992**, *150*, 589-593.
16. Castellanos, N.I.; Bharti, B.; Velev, O.D. Field-Driven Reversible Alignment and Gelation of Magneto-Responsive Soft Anisotropic Microbeads *J. Phys. Chem. B*, **2021**, *125* (28), 7900–7910.
17. Shroyan, B.; Swan, J.W.; Puyvelde, P.V.; Vermant, J. Quantifying the dispersion quality of partially aggregated colloidal dispersions by high frequency rheology. *Soft Matter*, **2017**, *13*, 7897-7906.
18. Schmauch, M.M.; Mishra, S.R.; Evans, B.A.; Velev, O.D.; Tracy, J.B. Chained Iron Microparticles for Directionally Controlled Actuation of Soft Robots. *ACS Appl. Mater. Interfaces.* **2017**, *9*, 11895–11901.
19. Varga, Z.; Filipcsei, G.; Zrinyi, M. Magnetic field sensitive functional elastomers with tuneable elastic modulus. *Polymer*, **2006**, *47*, 227-233.

20. Zhang, J.; Ren, Z.; Hu, W.; Soon, R.H.; Yasa, I.C.; Liu, Z.; Sitti, M. Voxelated three-dimensional miniature magnetic soft machines via multimaterial heterogeneous assembly. *Sci. Robot.* **2021**, *6*, 1-14.
21. Kim, J.; Chung, S.E.; Choi, S-E.; Lee, H.; Kim, J.; Kwon, S. Programming magnetic anisotropy in polymeric microactuators. *Nat Mater.* **2011**, *10*, 747-752.
22. Yamine, E.; Souaid, E.; Youssef, S.; Abboud, M.; Mornet, S.; Nakhl, M.; Duguet, E. Particles with Magnetic Patches: Synthesis, Morphology Control, and Assembly. *Part. Part. Syst. Charact.* **2020**, *37*, 1-12.
23. Hu, X. et al. Magnetic soft micromachines made of linked microactuator networks. *Sci. Adv.* **2021**, *7*, 1-9.
24. Han, K.; Shields IV, C.W.; Velev, O.D. Engineering of Self-Propelling Microbots and Microdevices by Magnetic and Electric Fields. *Adv. Funct. Mater.* **2018**, *28*, 1705953 (1-14).
25. Bharti, B.; Rutkowski, D.; Han, K.; Kumar, A.U.; Hall, C.K.; Velev, O.D. Capillary Bridging as a Tool for Assembling Discrete Clusters of Patchy Particles. *J. Am. Chem. Soc.* **2016**, *138*, 14948–14953.
26. Han, K. et al. Sequence-encoded colloidal origami and microbot assemblies from patchy magnetic cubes. *Sci. Adv.*, **2017**, *3*, 1701108 (1-6)
27. Fameau, A.L.; Lam, S.; Velev, O.D. Multi-stimuli responsive foams combining particles and self-assembling fatty acids. *Chem. Sci.* **2013**, *4*, 3874-3881.
28. Lee, J.G.; Porter, V.; Shelton, W.A. Bhari, B. Magnetic Field-Driven Convection for Directed Surface Patterning of Colloids. *Langmuir*, **2018**, *34*, 15416–15424.
29. Yu, M.; Ju, B.; Liu, S.; Choi, S-B. Magnetoresistance Characteristics of Magnetorheological Gel under a Magnetic Field. *Ind. Eng. Chem. Res.* **2014**, *53*, 4704–4710.

30. Lalitha, K.; Prasad, Y.S.; Sridharan, V.; Maheswari, C.U.; John, G.; Nagarajan, S. A renewable resource-derived thixotropic self-assembled supramolecular gel: magnetic stimuli responsive and real-time self-healing behaviour. *RSC Adv.*, **2015**, *5*, 77589–77594.
31. Chatterjee, J.; Haik, Y.; Chen, C.J. Biodegradable magnetic gel: synthesis and characterization. *Colloid Polym. Sci.* **2003**, *281*, 892-896.
32. Sorokina, O.N.; Kovarski, A.L.; Lagutina, M.A.; Dubrovskii, S.A.; Dzheparov, F.S. Magnetic Nanoparticles Aggregation in Magnetic Gel Studied by Electron Magnetic Resonance (EMR). *Appl. Sci.* **2012**, *2*, 342-350.
33. Tarama, M.; Cremer, P.; Borin, D.Y.; Odenbach, S.; Lowem, H.; Menzel, A.M. Tunable dynamic response of magnetic gels: Impact of structural properties and magnetic fields. *Phys. Rev.* **2014**, *90*, 1-9.
34. Braim, S.A.; Shakesheff, K.M.; Saunders, B.R.; Alexander, C. Thermoresponsive magnetic colloidal gels via surface-initiated polymerisation from functional microparticles. *J. Mater. Chem. B*, **2016**, *4*, 962-972.
35. Koos, E. & Willenbacher, N. Capillary Forces in Suspension Rheology. *Science*, **2011**, *331*, 897-900.
36. Koos, E.; Johannsmeier, J.; Schwebler, L.; Willenbacher, N. Tuning suspension rheology using capillary forces. *Soft Matter*, **2012**, *8*, 6620-6628.
37. Koos, E. Capillary suspensions: Particle networks formed through the capillary force. *Current Opinion in Colloid & Interface Science*, **2014**, *19*, 575–584.
38. Schneider, M.; Koos, E.; Willenbacher, N. Highly conductive, printable pastes from capillary suspensions. *Sci. Rep.* **2016**, *6*, 1-10.
39. Lewandowski, E.P. Bernate, J.A.; Tseng, A.; Searson, P.C.; Stebe, K.J. Oriented assembly of anisotropic particles by capillary interactions. *Soft Matter*, **2009**, *5*, 886–890.

40. Botto, L.; Lewadowski, E.P.; Cavallaro, M.C. Jr.; Stebe, Stebe, K.J. Capillary interactions between anisotropic particles. *Soft Matter*, **2012**, *8*, 9957-9971.
41. Roh, S. & Velev, O.D. Nanomaterials Fabrication by Interfacial Templating and Capillary Engineering in Multiphasic liquids. *AIChE*. **2017**, *64*, 3558-3564.
42. Roh, S et al. 3D-printed Silicone Soft Architectures with Programmed Magneto-Capillary Reconfiguration. *Adv. Mater. Technol.* **2019**, *4*, 1800528 (1-6).

## CHAPTER 2

### Field-driven reversible alignment and gelation of magneto-responsive soft anisotropic microbeads

#### 2.1 Introduction

The ability to provide a structural response to environmental conditions is embedded in the genetic makeup of many living beings.<sup>1-3</sup> Enabling such response in synthetic colloidal matter holds the key to encode life-like features in the future generations of artificial materials.<sup>2,4-7</sup> One example of natural response to external fields is found in magnetotactic bacteria.<sup>1</sup> These bacteria synthesize iron oxide nanoparticles within their cytoplasm and create a permanent magnetic dipole that enables the bacteria to sense the surrounding magnetic field and to reconfigure and coordinate their movement accordingly. They can thus swim along the direction of Earth's magnetic field while seeking to find optimal conditions for their survival.<sup>6</sup> The chain(s) of magnetic nanoparticles internalized in the bacteria act as means of navigation to find favorable habitats.<sup>8</sup> An ability to incorporate micro and nanosized particles within beads mimicking magnetotactic orientation could provide new means for designing magneto-responsive materials, which reconfigure in response to external environments and stimuli.

Colloidal particles which change their physical and/or chemical state in response to external stimuli such as temperature<sup>9</sup>, electromagnetic and magnetic fields<sup>10</sup>, and pH<sup>7,11</sup> can find numerous applications such as targeted drug delivery<sup>6</sup>, biomolecular separations, smart structures and soft actuators.<sup>12-14</sup> One such class of responsive materials are magnetic colloids, which alter their assembled state in response to the presence of an external magnetic field.<sup>15-18</sup> Magnetic colloids dispersed in aqueous or non-aqueous medium, commonly known as ferrofluids, interact via magnetic forces in addition to conventional colloidal forces such as van der Waals and

electrostatics.<sup>19-21</sup> Programming these interactions and directing the morphology of colloidal assemblies coupled in space and time is one of the strategies of encoding non-equilibrium response in artificial matter. The assembly and reconfiguration of magnetic colloids is governed by the physical state of the constituting particles, which could be ferromagnetic, ferrimagnetic or superparamagnetic.<sup>21,22</sup>

Ferromagnetic materials refer to the class of magnetic materials which can retain their magnetic moment even after the external field is removed. These ferromagnetic materials have permanent dipole moment and behave as microscale magnets.<sup>6</sup> One problem that is often encountered with such particles in a dispersing medium is the lack of colloidal stability, i.e., the ferromagnetic particles are prone to spontaneous aggregation. The sum of van der Waals and magnetic dipolar forces exceeds the ability of Brownian motion to disrupt the strongly attractive structure.<sup>23</sup> To prevent this aggregation, it is necessary either to introduce a repulsive force barrier between the particles by adding surface adsorbed amphiphiles<sup>24</sup> or immobilizing the nanoparticles inside a larger matrix. In this article we find a way to use the latter strategy and investigate the impact of spatial distribution of magnetic nanoparticles (MNPs) within an elastomer matrix of carrier microbeads on their magnetic response.

Magnetorheological elastomers,<sup>21,25</sup> magneto-colloidal fluids,<sup>16,26,27</sup> gels,<sup>3,28-30</sup> and foams<sup>31-33</sup> comprise classes of smart materials, whose rheological properties can be controlled by an external magnetic field.<sup>8</sup> There is also big stride towards the formation of responsive soft materials with internal magnetic anisotropy, whose macroscopic response is guided by particle structures assembled within the soft composites. Such structures can be fabricated by assembly of particles inside polymerizable medium and later crosslinking the polymer matrix, so that the positions of the particles remain fixed within the embedding polymer network.<sup>34-36</sup> Thus, the

structural motif remains embedded after the external magnetic field applied during the synthesis step is removed.<sup>25</sup>

Under uniform magnetic fields or field gradients, the moments of the MNPs align, and the attractive magnetic dipolar forces pull them together, favoring magnetization along the direction of the field and leading to chaining.<sup>6,37-41</sup> These chain-like assemblies or percolated networks can, depending on the packing fraction of the sample of microbeads, span the whole sample because of the magnetically induced particle chaining within the matrix.<sup>5</sup> The magnetic and mechanical properties of such long-ranged assemblies can be strongly coupled to make magnetically controlled matrices where nano- or micron-sized magnetic particles have been embedded in the elastomers.<sup>42,43</sup> The MNPs within the soft composites can be either distributed randomly or organized in chains.<sup>30,34,43</sup> The MNPs used in such responsive composites are usually made of iron oxides (such as  $\gamma$ -Fe<sub>2</sub>O<sub>3</sub> and Fe<sub>3</sub>O<sub>4</sub>),<sup>16,39,44</sup> metals or alloys (containing metals such as Fe, Co, Ni, Fe, Pt) or iron nitride particles which can also be biologically compatible. Furthermore, in the absence of an external field, chainlike structures can form loops or arrangements that can lead to the formation of the gel phase.<sup>25</sup> Synthesizing such composite colloidal particles with tunable magnetic properties remains a challenge and is a key focus of this Chapter.

We present here the design, synthesis, and characterization of a class of soft microbeads (SMBs) made of elastomeric matrix containing either randomly distributed or aligned chains of MNPs. The suspensions of magneto-responsive soft particles are made by a scalable technique that enabled us to synthesize polydimethylsiloxane (PDMS) microbeads with embedded MNPs. The resulting SMBs show a number of distinctly different assembly modes, and rheological responses in the presence and absence of an external magnetic field. We describe how these soft microbeads exhibit responsive, switchable, and reversible binding driven by magnetic interactions. We

demonstrate and analyze their orientation, assembly, and disassembly in the presence of magnetizing and demagnetizing fields.

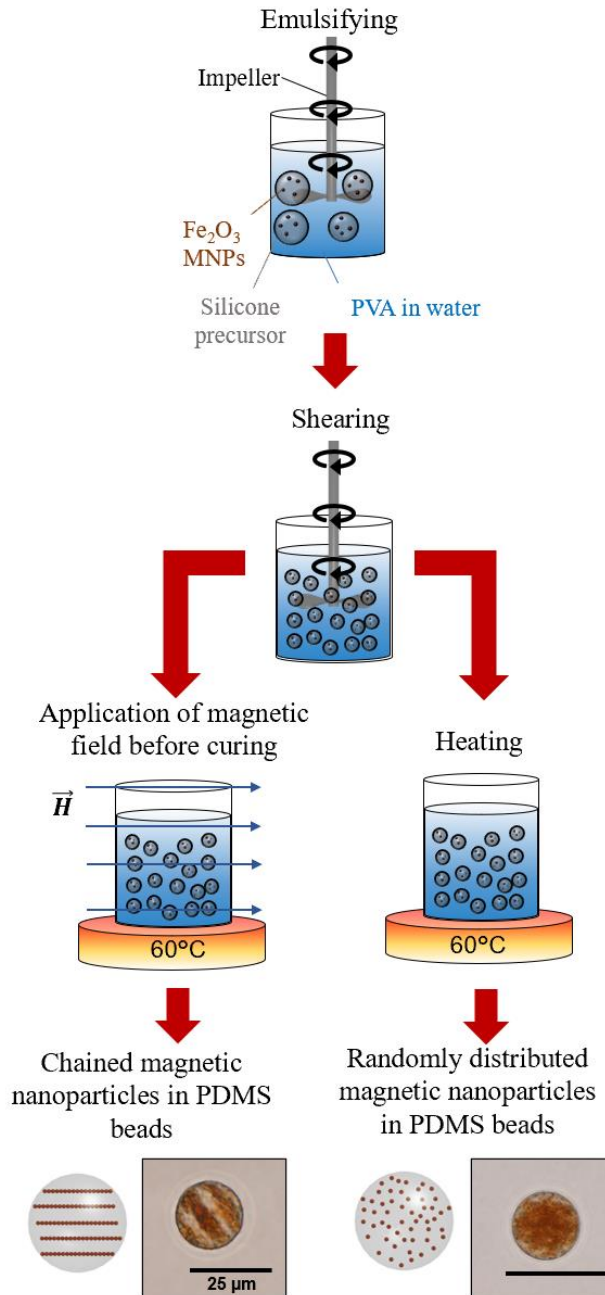


**Figure 2.1** Schematics of the method of synthesizing PDMS microbeads with embedded iron (III) oxide nanoparticles using an emulsification technique. The internal organization of the magnetic nanoparticles can be preserved if the soft microbeads (SMBs) are cured under a magnetic field. The SMB microscope image examples shown are bigger than those typically used for the experiments (10 μm) for better visualization.

## **2.2 Materials and Methods**

### ***2.2.1 Dispersing the magnetic nanoparticles within the PDMS precursor medium***

Depending on the desired weight percent of MNPs in the final PDMS microbead suspension, 2.5 wt%, 5 wt%, or 10 wt% iron (III) oxide nanoparticles (20 nm, MKNano) were added to 36 g tetrahydrofuran (THF) in a round bottom flask and sonicated for one hour. THF was added to temporarily reduce the viscosity of the PDMS precursor (Sylgard 184 obtained from Dow) such that the particles could be uniformly dispersed in the silicone emulsion. The required amount of PDMS prepolymer was then added to the round bottom flask and the mixture was further sonicated for 5 hours to ensure uniform distribution of particles in the solvent. The THF was then evaporated from the mixture, leaving the PDMS precursor with internalized MNPs.

### ***2.2.2 Synthesis of PDMS microbeads containing randomly distributed MNPs***

PDMS is a cross-linkable polymer with Young's modulus tunable by the molar ratio of PDMS base and the crosslinker. The synthesis of microbeads from PDMS includes emulsification and crosslinking of PDMS by precursor and curing agent. First, 14 wt% polyvinyl alcohol (PVA) solution was made by heating and stirring for two hours of 100 g of deionized (DI) water (18.2 M $\Omega$  cm at 25 °C, obtained from a Millipore Milli-Q Academic water purification system) at 120 °C, to which we added 16.28 g of polyvinyl alcohol (PVA) (Mowiol 18-88, Sigma-Aldrich) in a covered beaker. The exact weight percent of the PVA in solution was determined gravimetrically. The PVA-water solution (40 mL) was then placed in a beaker and mixed at 150 RPM in a mechanical mixer with an impeller, while the PDMS was mixed and degassed. The addition of the PVA was necessary because of the large mismatch of the high viscosity of PDMS (3500 cP) and the low viscosity of water (1 cP), which produces very polydisperse PDMS droplets during

shearing of the dispersion. The addition of the PVA to the water phase allowed the formation of much more uniform droplets.<sup>45</sup> The 10:1 mixture of PDMS/crosslinker Sylgard 184 was then injected into the 14% PVA solution while it was being mixed and the suspension was stirred at 150 RPM for ten minutes to ensure homogenization. The emulsion was then refined further by mixing at 250 RPM for an hour. Once the mixing was complete, the emulsion was placed in an oven at 60 °C overnight to accelerate the crosslinking process of the polymer matrix. The PDMS microbeads were then washed several times with an aqueous solution of Tween 20 (0.1 wt%) using a vortex mixer and a centrifuge. Determination of the final weight percent of the PDMS SMB dispersion was done gravimetrically and, in this report, our chosen final weight percent was 50 wt% magnetic PDMS microbeads in aqueous solution of 0.1 wt% Tween 20.

### ***2.2.3 Synthesis of PDMS microbeads containing magnetically aligned MNPs***

These microbeads were made by a process similar to the PDMS microbeads with randomly distributed embedded MNPs. The main difference was that an external magnetic field (19 mT) was applied parallel to the chamber walls during the whole curing duration, overnight. This resulted in the formation of PDMS microbeads with locked-in dispersed or magnetically aligned chains of the MNPs embedded in the silicone matrix (Figure 2.2, Figure 2.3). A table-top demagnetizer was used to demagnetize the beads.

### ***2.2.4 Rheological Analysis of magnetic microbead suspensions***

Rheological analysis of the suspensions was performed using a DHR-2, TA Instruments (New Castle, DE) rheometer with serrated parallel plate geometry (diameter = 40 mm with 0.5 mm gap size). Sandpaper was used to minimize the effect of wall slip during the experiments. Angular

frequency sweeps were conducted at 1% strain for 100 – 0.03 rad s<sup>-1</sup>. The amplitude oscillatory measurements were conducted within the linear viscoelastic regime of the samples. The linear viscoelastic regime was determined by performing oscillatory strain sweeps at a constant angular frequency of 10 rad sec<sup>-1</sup>. The samples were covered with a homemade solvent trap to prevent water evaporation. All tests were performed at a constant temperature of 25 °C.

### ***2.2.5 Optical Microscopy and Cell Orientation***

Optical microscopy (Olympus, BX-61) with an Olympus DP-70 digital CCD camera was used to characterize the morphology of the magnetic PDMS microbeads. Magnetization and demagnetization studies were also conducted and recorded with the chained microbeads suspension. The orientation of the Earth magnetic field in the location of the experimental chamber and throughout the laboratory were determined by a handheld iPhone 11 compass sensor.

### ***2.2.6 Magnetometry***

The magnetization of the MNP-containing gels was characterized using the Quantum Design MPMS 3 SQUID/VSM magnetometer. The device was calibrated using a reference sample made of Pd. The samples were run in DC mode at room temperature and at atmospheric pressure.

## 2.3 Results and Discussion

### 2.3.1 Bead Synthesis and Morphology

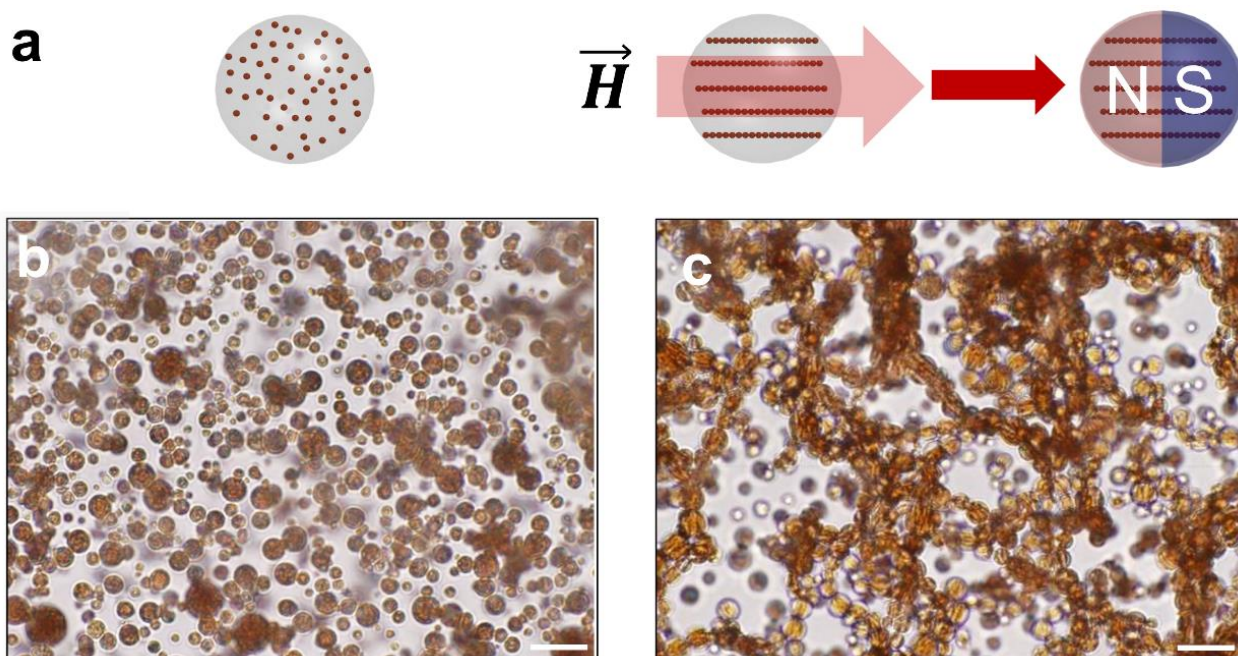


**Figure 2.2** (a) Magnetic elastomer spheres dispersed in water where the embedded MNPs can have two different orientations by having either (b) embedded randomly distributed iron (III) oxide nanoparticles (10 wt%, no field applied), or (c) magnetically aligned iron (III) oxide nanoparticles (10 wt%, field of 19 mT strength applied during curing). Scale bars are 20  $\mu\text{m}$ .

The microbead emulsion fabrication process, regardless of the application of external magnetic field or not, resulted in spherical PDMS microbeads with an average diameter of 10  $\mu\text{m}$  (Figure 2.2). The individual magnetic particles inside these microbeads could not be resolved in the microscopy images due to their small size. However, after the external magnetic field is applied during the synthesis (Figure 2.2a), magnetically aligned particle chains can be clearly observed as lines embedded in the PDMS microbeads (Figure 2.2c, Figure 2.3b, Figure 2.3c) as opposed to scattered or randomly distributed particle clusters in the microbead (Figure 2.2b, 2.3a). Based on

earlier experiments, we determined that the lowest amount of embedded MNPs that could be magnetically aligned during curing was 2.5 wt% MNPs. We synthesized PDMS beads with 1 wt% MNPs embedded and did not observe any chains or magnetic alignment. We also wanted to determine a range of maximum loading of MNPs possible such that no MNPs would be left in the water phase and outside of the PDMS beads. We were able to conclude that the maximum loading of MNPs in the PDMS beads was about 25 wt%. Details on this can be found in Appendix A.

Furthermore, before arriving at the shear rate of 250 RPM, we synthesized magnetic PDMS beads at shear rates ranging from 200 RPM to 1000 RPM. We were able to observe that the PDMS bead size decreased as the shear rate increased. Moreover, we noted that any shear rate past 800 RPM resulted in no magnetic particles being embedded with 10 wt% MNP samples. This is likely due to the small PDMS size ( $\sim 3 \mu\text{m}$ ). Based on these findings, we decided to synthesize the beads at 250 RPM with varying, but a minimum of 2.5 wt%, embedded MNPs.

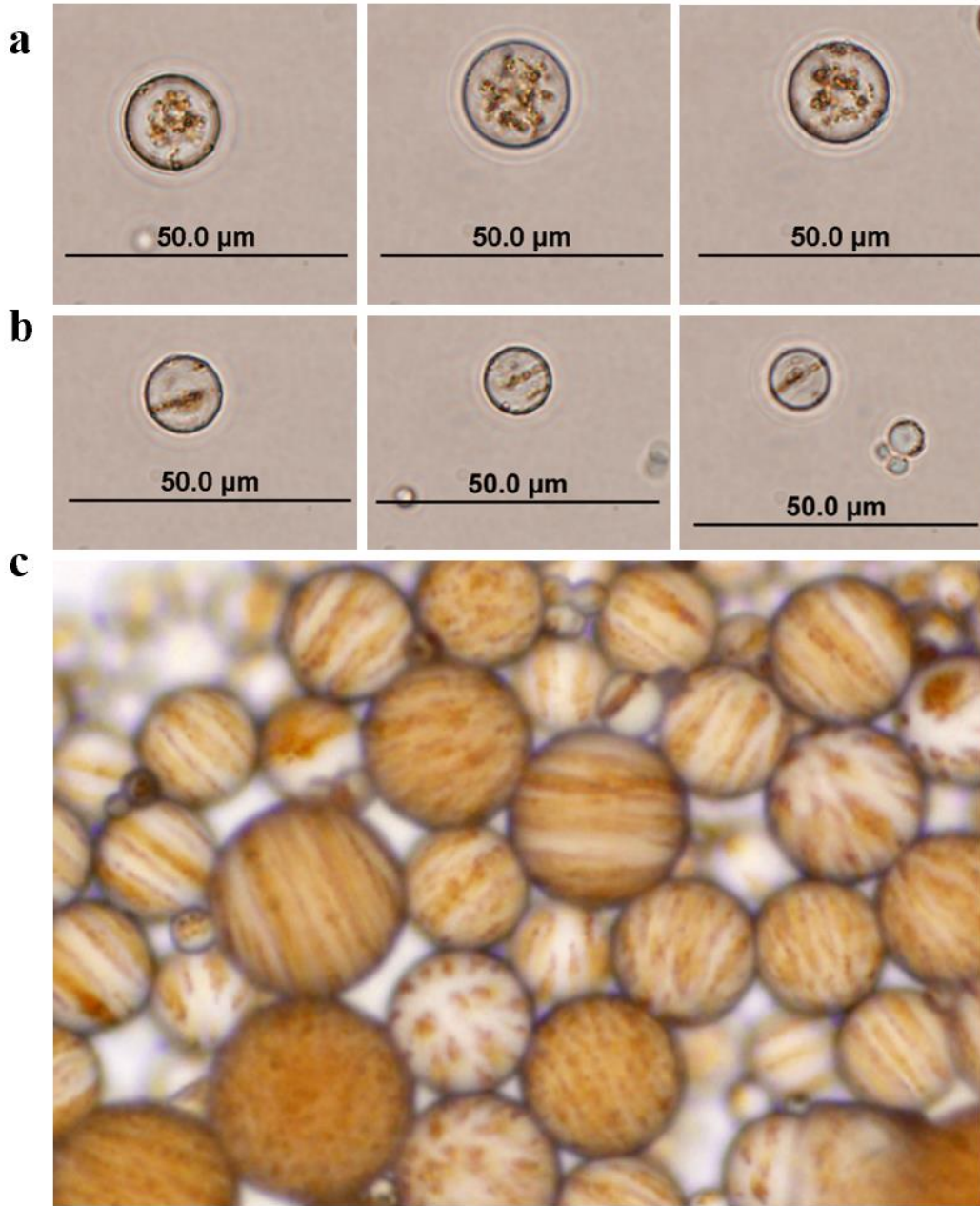


**Figure 2.3** Optical microscopy images of PDMS beads containing 2.5 wt% of magnetic nanoparticles in (a) randomly dispersed state and (b) polymerized after the MNPs have been aligned in the presence of magnetic field. Note that the MNPs in some beads can be aligned in the form of single chain traversing the host bead. (c) Optical microscopy image of a suspension of PDMS beads containing 10 wt% of aligned magnetic nanoparticles. The higher density chains in the beads are clearly distinguishable.

### ***2.3.2 Bead Magnetic Interaction***

After the magnetic field is turned off, these two types of SMB suspensions interact and assemble to form drastically different patterns, as seen in the microscopy images in Figure 2.2b and 2.2c. Although the concentration of both types of magnetic PDMS microbeads is high and attractive interactions between microbeads in both cases can be observed to lead to some clustering, the SMBs with randomly distributed MNPs remains generally dispersed in suspension and not interconnected on a longer scale (Figure 2.2b). The SMB suspensions with embedded aligned MNPs, on the other hand, display the formation of percolated or branched networks (Figure 2.2c).

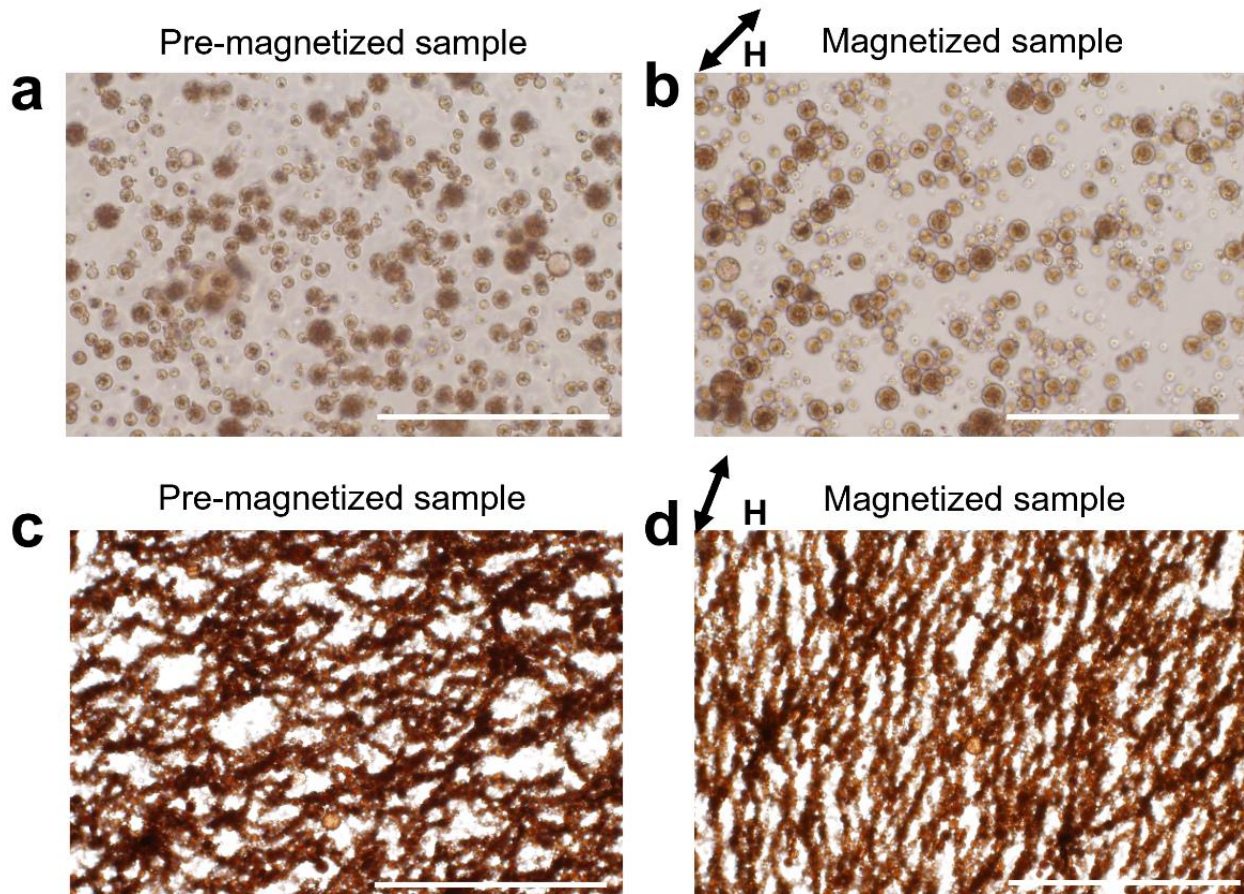


**Figure 2.4** The magnetic interactions in SMB suspensions (50 wt% PDMS microbeads in water, each containing 10 wt% MNPs) can vary as: (a) When MNPs are randomly dispersed inside, the microbeads do not appear to interact without the presence of an external magnetic field even when they have been subjected to external field earlier (“pre-magnetized”). (b) They demonstrate very weak chaining and branching only if the system is subjected to a magnetic field (19 mT). (c) Microbeads with embedded magnetically aligned MNPs form branched networks when pre-magnetized, even if external field is not applied, and (d) form organized percolated networks and align in the direction of an applied magnetic field (19 mT). Scale bars are 200  $\mu\text{m}$ .

This structure formation was investigated further by subjecting each microbead type to a permanent, external magnetic field of 19 mT. The SMBs with randomly distributed MNPs showed

little to no interaction before the application of the external field (Figure 2.4a). Once a field was applied, these microbeads became partially structured in as little as 15 s, forming a few short linear chains and bundles (Figure 2.4b). However, these structures were not uniform in the bulk suspension, and they easily and almost immediately broke apart if the suspension was mechanically disturbed or if the magnetic field was removed. The SMBs containing aligned MNPs clearly formed long-range linear flexible branched structures even when no additional external field was applied while in suspension (Figure 2.4c). This is a result of their remanent magnetization (pre-magnetization) during the application of the external field during the fabrication process. Once an external field was applied to the SMBs with aligned MNP chains, these initially randomly branched structures rapidly re-oriented and re-organized in the direction of the field in as little as three seconds (Figure 2.4d). Moreover, after being formed and magnetized with an external field (19 mT) the structures almost immediately ( $\approx 1$  s) re-assembled if the system was disturbed, indicating that the microbeads with aligned MNPs had residual polar magnetization or magnetic memory.

### ***2.3.3 Bead Assembly and Demagnetization***

The assembly of microbeads with non-aligned MNPs in external field is driven by the polarization of the nanoparticles within the SMB PDMS matrix. In the presence of external field, the magnetic domains within the embedded MNPs endow the SMBs with a net magnetic dipole moment. This induced dipole leads to the formation of well-known bead chain necklace type assembly of the SMBs. The assembled SMB structures with randomly internalized MNPs break-up upon switching off the external magnetic field. The observed SMB disassembly agrees with a previous study on the assembly/disassembly of superparamagnetic microspheres in response to

field on and off cycles.<sup>2</sup> The previously reported disassembly was attributed to the rapid decrease/disappearance of magnetic moment of the microparticles upon switching off the external magnetic field. In our case of microbeads with non-aligned MNPs, the origin of the observed disassembly is similarly a result of decrease in magnetic attraction upon switching off the external field, combined with the surface charge repulsions and hydrodynamic interactions.

In contrast, the SMB structures with pre-aligned chains do not disassemble upon switching off the external magnetic field but reconfigured to form a percolated network. The lack of disassembly is due to the magnetic retentivity of the microbeads with aligned chains, where the residual magnetization allows them to more readily interact with neighboring microbeads, leading to rapid percolation. Once magnetized, the SMB system with aligned MNP chains formed percolated networks even without the presence of an external field (Figure 2.4c). This local residual magnetization and corresponding structural relaxation into a percolated network of microbeads imparts specific viscoelastic and self-reassembly characteristics of the microbead suspension (discussed later). The formation of percolated networks in such types of interacting dipolar systems have been predicted and modelled theoretically earlier.<sup>5,46-51</sup> It can be noted that at high concentrations, the spontaneous chaining in systems without applied field is not in any specific direction and displays branching, often at the junction of one large and two smaller beads. Once we applied a magnetic field, however, the branched SMB network became much more uniformly aligned and structured, with chaining in the applied field direction (Figure 2.4d). The long-range permanently assembled structure of extended and in occasionally branched chains formed by the microbeads can be re-aligned by an application of fields in different directions.

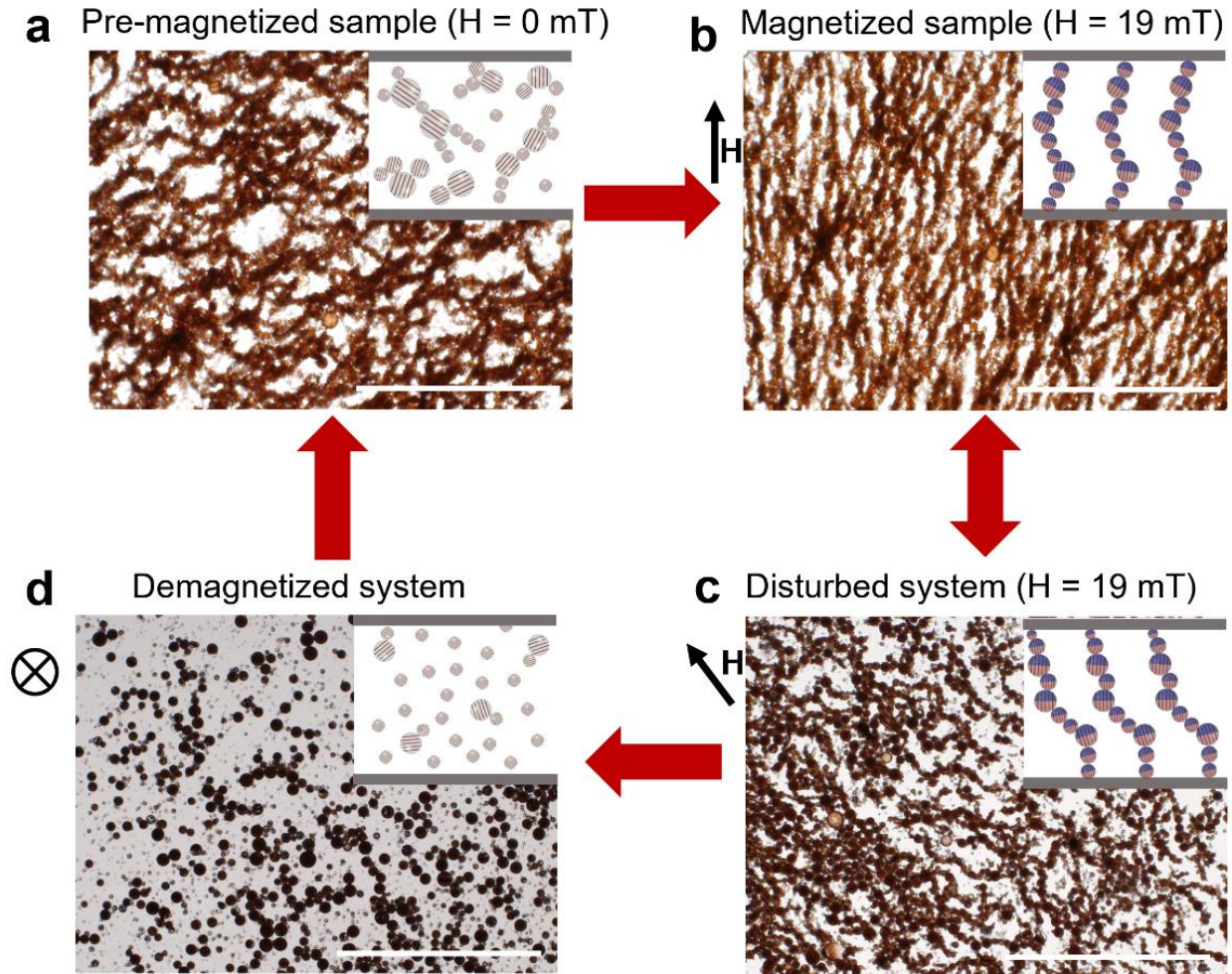


**Figure 2.5** The magnetically aligned microbead system demonstrated tunability by using reversible magnetization. (a) The aligned PDMS microbeads form branched networks even if no external magnetic field is applied due to the pre-magnetization during fabrication and (b) form more organized branched structures when an external field is applied ( $H = 19$  mT). (c) These long-ranged structures break apart when the system is disturbed but can re-form almost immediately. (d) They can break down into mostly individual microbeads if the suspension is demagnetized but can re-assemble when re-magnetized. The black arrows indicate the direction of the external magnetic field. Scale bars are  $200\ \mu\text{m}$ .

The percolated structures from internally aligned magnetic particles do not experience spontaneous disassembly over time as the particles can sustain their dipolar polarization. Even if such network is strongly disturbed by stirring or other mechanical disturbance, it re-forms. However, there is a simple and efficient technology solution for resetting this system to its original dispersed, weakly interacting state. Soft magnets can be demagnetized by applying an alternating magnetic field of decaying intensity through a demagnetizer coil operated by a corresponding circuit.<sup>52</sup> During this process, the ferromagnetic domains within the nanoparticles are 'forced' to reorient multiple times, while their moment is reduced in a preprogrammed way. This technique was used by us previously for triggered disassembly of magnetic Janus particles.<sup>53</sup> The use of the technique is illustrated in Figure 2.5. When the suspension of magnetically aligned PDMS microbeads (Figure 2.5a-c) was subjected to a demagnetizing field, it experienced a large reduction of the residual magnetization. The change is evident in the microscopy image in Figure 2.5d, where the initial chain-like structure was disassembled in the demagnetizer field, and a suspension of discrete, spatially separated microbeads was obtained. The magnetic moment of the microbeads can be regained by re-magnetization and a percolated structure of microbeads can be re-assembled to return to the initial state of the SMBS as shown in Figure 2.5a. Thus, we have a two-state switchable system, with long-range structuring capabilities.

#### ***2.3.4 Other types of magnetic material embedded in the PDMS beads***

We experimented with other magnetic material. NdFeB microparticles were embedded in the PDMS beads following a similar emulsification process. 10 wt% of NdFeB microparticles were dispersed in the PDMS base using THF to lower the viscosity of the PDMS in order to disperse the microparticles. The beads were synthesized using the same mixer; however, we synthesized

the beads using two different RPM. Figure 2.6a shows the resulting magnetic beads when the emulsion was sheared at 500 RPM. Figure 2.6b shows the resulting magnetic beads when the emulsion was sheared at 500 RPM. As can be observed, the bead size was similar using either RPM, thus we chose to use 500 RPM going forward. We knew that NdFeB microparticles have residual polar magnetization, which could potentially lead to bigger bead agglomerates. For this reason, we attempted to demagnetize the emulsion before curing. Figure 2.6c are the microscopy images of the beads with demagnetized embedded microparticles. No significant difference between these demagnetized beads and the beads that were not demagnetized prior to curing (Figure 2.6a and 2.6b) can be observed, thus we did not demagnetize the microparticles before curing for any future experiments.

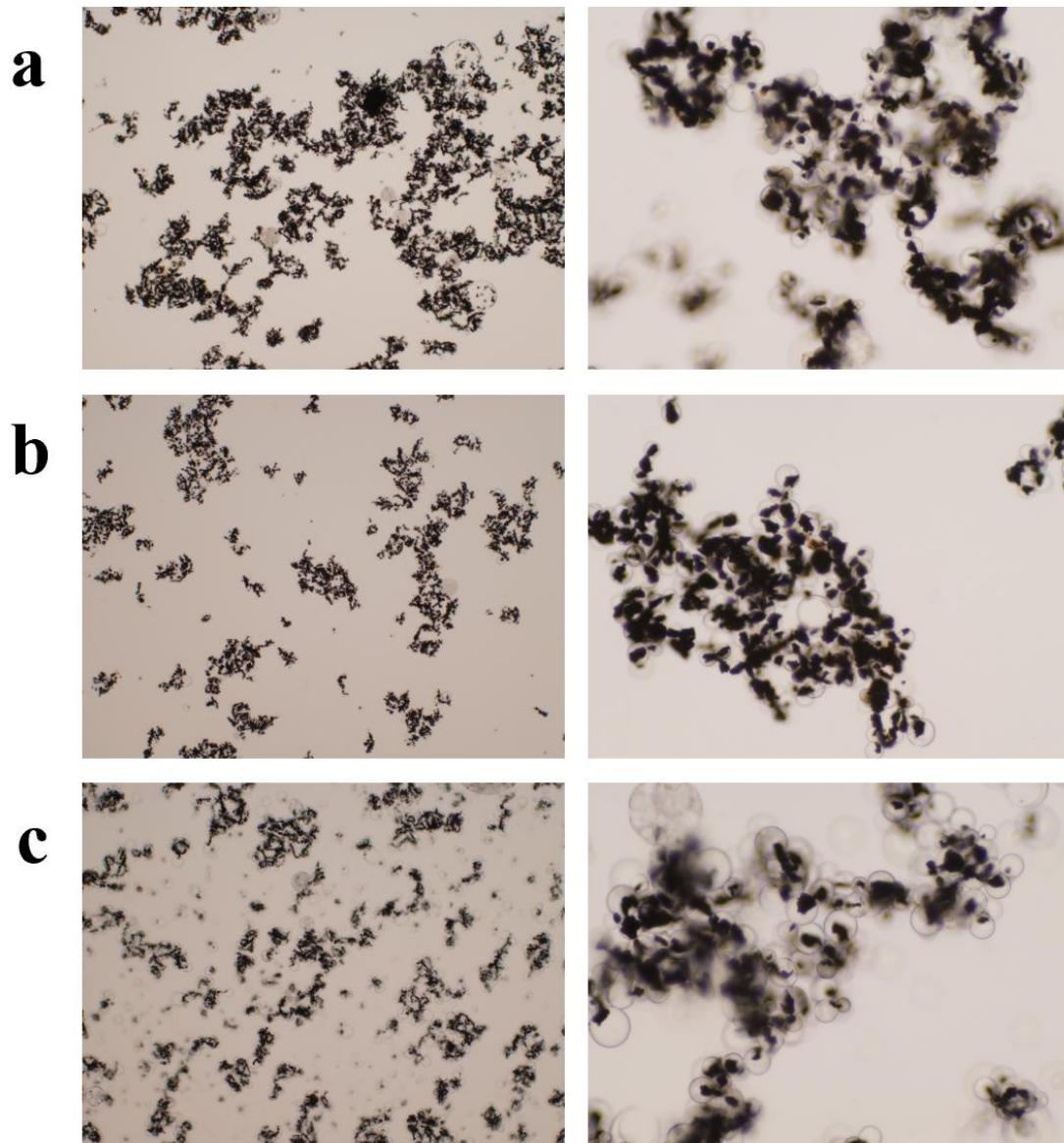


**Figure 2.6** Microscopy images of PDMS beads with embedded NdFeB microparticles sheared at (a) 500 RPM and (b) 1000 RPM during emulsification. (c) Microscopy images of magnetic PDMS beads with embedded NdFeB microparticles that were demagnetized before curing.

One of our goals was to be able to break the NdFeB PDMS beads apart as we had done with the  $\text{Fe}_2\text{O}_3$  PDMS beads. In order to accomplish this, we changed variables such as shear rate, demagnetization time, and magnetic alignment in our system. We demagnetized the beads for

different amounts of time and then tried either sonication or vortexing to determine which would be more effective at breaking the beads apart. Figure 2.7 has microscopy images that summarize the different demagnetization times and mixing techniques we attempted. Figure 2.7a shows the NdFeB beads that were demagnetized for 7 minutes and then sonicated for 5 seconds. Branches of PDMS beads were still present at this point. We next demagnetized the beads for an hour and either sonicated (Figure 2.7d) or vortexed (Figure 2.7e) for 5 seconds prior to imaging. We were not able to observe the beads breaking apart. There were still many visible structures of beads present in the sample, even more so than the sample we demagnetized for 7 minutes. We next picked a demagnetization time that was somewhere between 7 minutes and one hour, which was 20 minutes. We demagnetized the NdFeB PDMS beads for 20 minutes and then either sonicated for 5 seconds (Figure 2.7b) or vortexed the sample for 5 seconds (Figure 2.7c). The sample that was vortexed continued to have bead aggregation, suggesting vortexing the sample is not enough to break the beads apart. Figure 2.7c shows that the beads were only able to be effectively broken apart if the sample was demagnetized for 20 minutes and sonicated for 5 seconds. These results suggest that the beads should not be demagnetized for an extended period of time and that sonicating the sample can effectively lead to the bead structure being disrupted and broken apart.

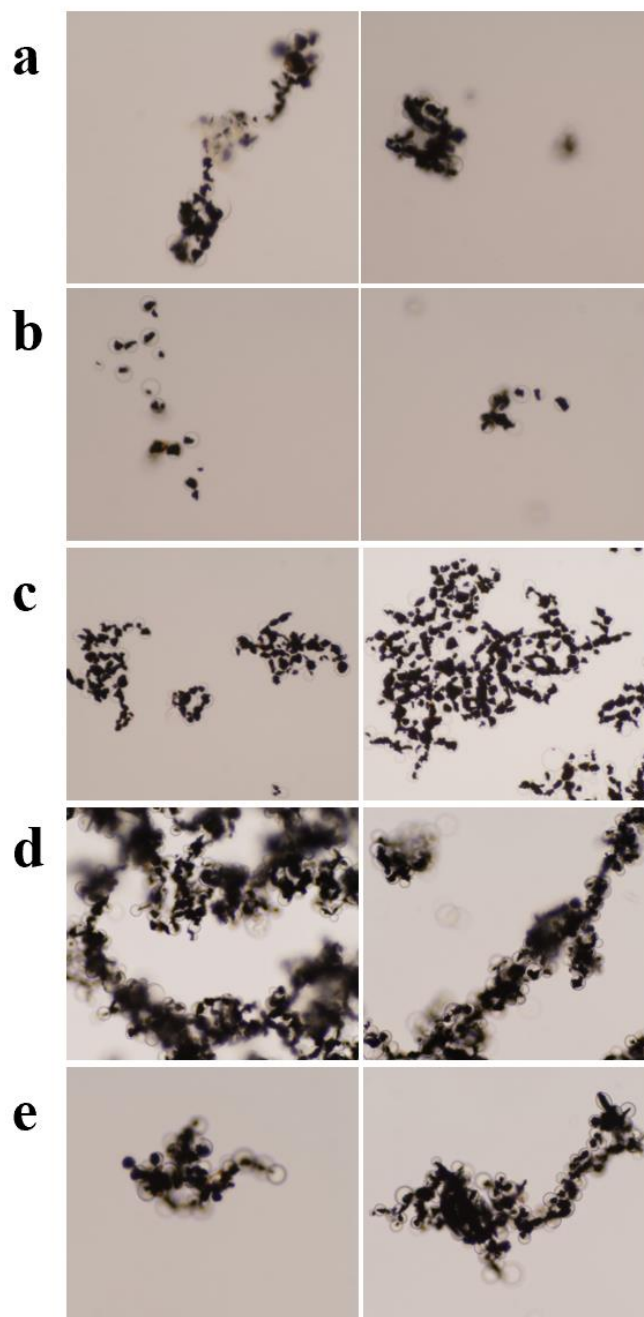


**Figure 2.7** Microscopy images of NdFeB PDMS beads that were (a) demagnetized for 7 minutes and then sonicated for 5 seconds prior to imaging, (b) demagnetized for 20 minutes and then sonicated for 5 seconds prior to imaging, (c) demagnetized for 20 minutes and then vortexed for 5 seconds prior to imaging, (d) demagnetized for an hour and then sonicated for 5 seconds prior to imaging, and (e) demagnetized for an hour and then vortexed for 5 seconds prior to imaging.

Another variable we tuned with the NdFeB PDMS beads was the alignment of the embedded NdFeB microparticles. We incorporated a magnetic field of 19 mT field strength during curing of the NdFeB PDMS beads as we had done with the PDMS beads with embedded  $\text{Fe}_2\text{O}_3$  MNPs. As can be observed in Figure 2.8, aggregated beads are observed regardless of whether a magnetic field is applied during curing (Figure 2.8b) or not (Figure 2.8a). The most noticeable difference in the suspensions of magnetized or not magnetized NdFeB beads can be observed in Figure 2.8c. Percolation network formation is confirmed in the case of the magnetized beads, which was not the case for the non-magnetized NdFeB PDMS beads. Furthermore, although percolation network formation was observed, it looked very different from the branch-like percolation network formation observed in the magnetically aligned  $\text{Fe}_2\text{O}_3$  PDMS beads. In some samples that were magnetized during curing, we can observe the microparticles appear to have some internal alignment (Figure 2.8b, right). However, this was not always the case. As can be seen in the sample imaged in Figure 2.8b, the microparticles did not always align even if the sample was cured under a magnetic field. This could be due to the size of these particles with respect to the bead size. Further work is needed to better understand how we can avoid this inconsistency in the alignment of the NdFeB microparticles. Thus, for the purpose of this dissertation, we remain focused on the PDMS beads with embedded  $\text{Fe}_2\text{O}_3$  MNPs for the rest of the work presented.

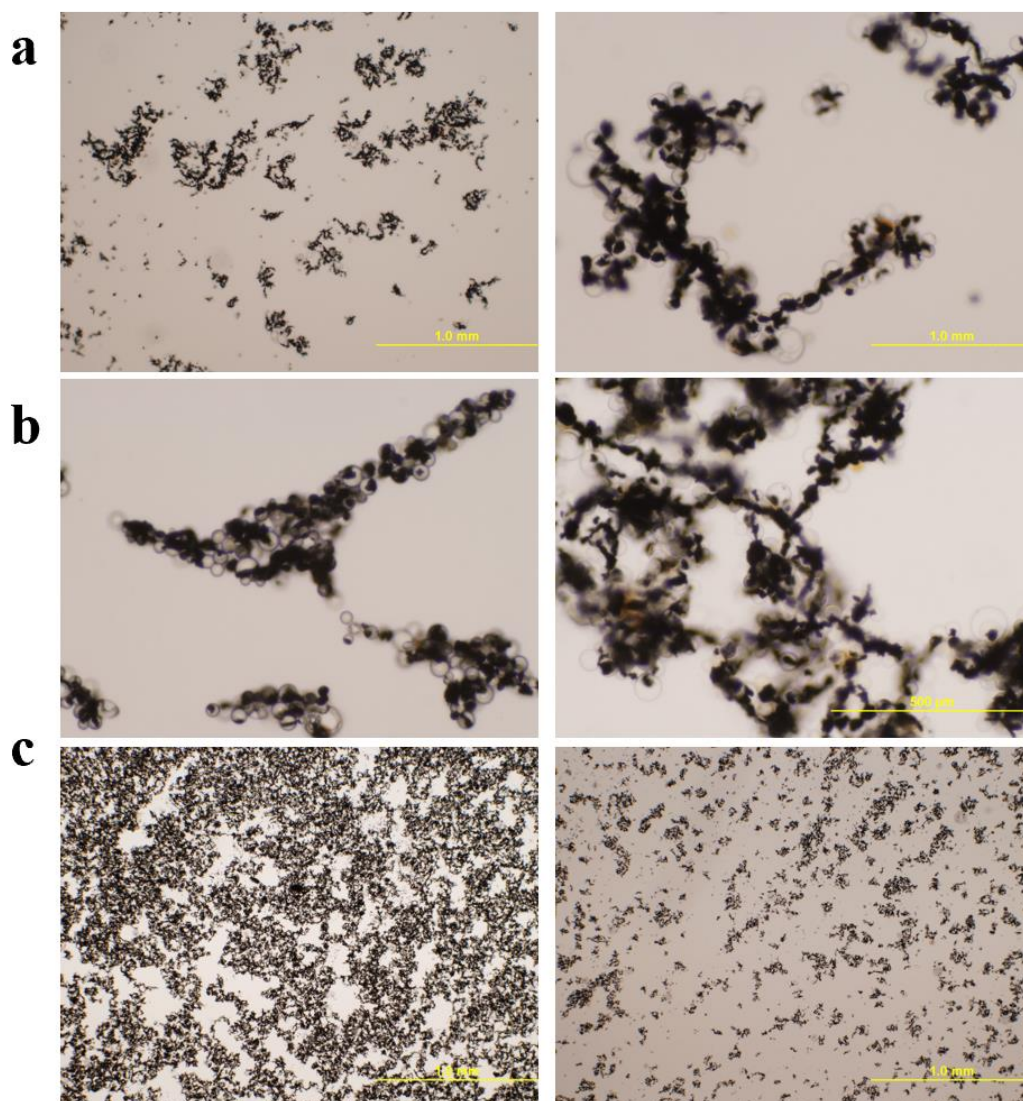


**Figure 2.8** Microscopy images of NdFeB PDMS beads (a) with no magnetic field applied during curing, (b) with a magnetic field of 19 mT field strength applied during curing, and (c) the percolation network formation of the NdFeB PDMS beads that were magnetized ( $H= 19$  mT) during curing.

### 2.3.5 Rheology of both types of magnetic ( $Fe_2O_3$ ) SMBs

The observed formation of large-scale percolated structures in the  $Fe_2O_3$  PDMS beads indicates the possible occurrence of phenomena such as gelation in macroscopic bulk systems. The formation of percolated and entangled particle networks is a common prerequisite for gelation.<sup>5,51,54</sup> The occurrence of gelation can be confirmed by macroscopic change in a few physical properties.<sup>55</sup> One common mechanical technique for characterizing the onset of gelation is rheology.<sup>56</sup> The magnetic alignment of the microbeads should affect their gelation, moreover it will be dependent on the type of particles present in the system. We investigated the rheological response of SMB systems with both non-aligned and aligned MNPs, subjected to small amplitude oscillatory shear experiments aimed to be within the linear viscoelastic regime of the suspensions. Their storage ( $G'$ ) and loss ( $G''$ ) moduli were measured as a function of the angular frequency ( $\omega$ ).

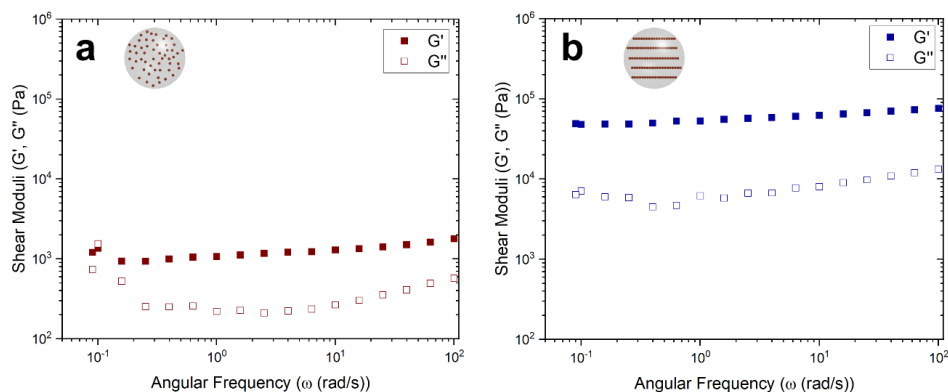


**Figure 2.9** Storage,  $G'$ , and loss,  $G''$ , moduli as a function of frequency for each type of magnetic microbead. (a) The lack of interactions between the SMBs with randomly distributed MNPs demonstrates lower  $G'$  and  $G''$  and more liquid-like properties whereas in (b) the weak interactions between the magnetically aligned SMBS with embedded chains lead to magnetic force-induced structuring or 'soft' gel-like properties (50 wt% PDMS microbead to water, 10 wt% embedded MNPs).

A comparison of the rheological response of the two types of microbead samples is presented in Figure 2.9. The sample of microbeads with randomly distributed MNPs appeared to be in a transition state, suggesting a very weak gel-like structuration, because  $G'$  is of the same magnitude and almost equal to  $G''$  at lower frequencies (Fig. 2.9a). The sample of SMBs with magnetically aligned MNPs demonstrated gel-like behavior with  $G' \gg G''$  at 50 wt% PDMS microbeads to water in the entire range of the frequency sweep (Fig 2.9b). These data suggest that the beads with aligned particles formed magnetic-induced gels with strong tolerance to external deformations/perturbations since it maintained its gel-like state throughout the whole frequency range (Figure 2.9). This sample has  $G'$  of approximately one order of magnitude higher than  $G''$  and hence  $\tan(\delta)$  of less than 1. The moduli of the microbead sample with aligned MNPs were several orders of magnitude greater than those of the sample with microbeads with randomly distributed nanoparticles, suggesting that the gel strength of the chained microbead sample is greater. This observation is further evidenced by the  $G'$  and  $G''$  of regular, nonmagnetic microbeads. These beads had a  $G'$  and  $G''$  several orders of magnitude lower than that of either type of magnetic microbeads (actual  $G' = 2.734$  Pa and  $G'' = 1.944$  Pa at 1 rad/s). This result indicates that the long-chain organization of the soft magnetic particles containing MNP chains with residual polarization assists with the formation of robust, magnetically actuable gels. However, these gels differ from common molecular gels in not showing any stretchability (due to which the Young's modulus could not be measured).

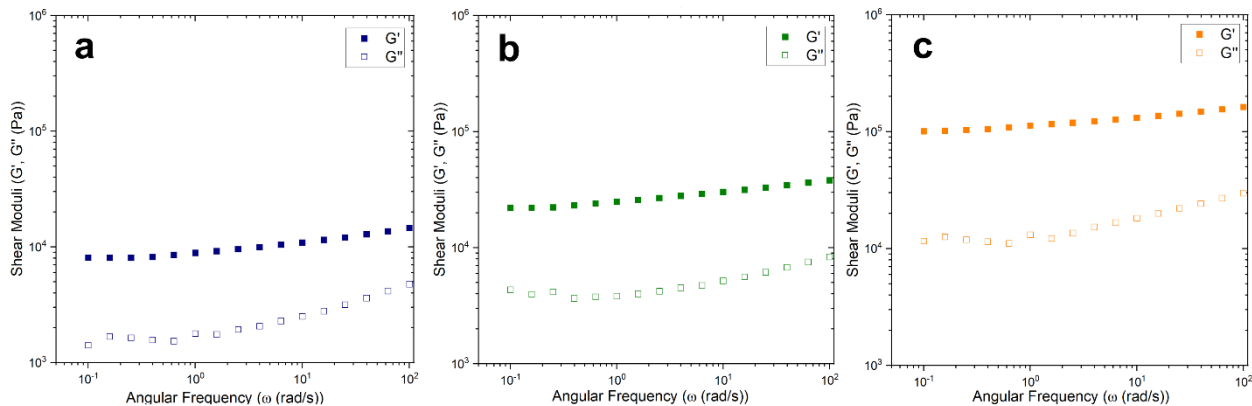


**Figure 2.10.** Storage,  $G'$ , and loss,  $G''$ , moduli as a function of frequency for magnetic microbeads with (a) 2.5 wt%, (b) 5 wt%, and (c) 10 wt% aligned MNPs embedded in the SMB PDMS matrix. The gel strength increases as the number of MNPs loaded in the microbeads increases.

The rheology experiments also made possible to determine the correlation between the fraction of magnetic material loaded into the SMBs and gel stiffness. The properties of SMB gels with increasing concentrations of magnetic particles embedded in the PDMS bead matrix, 2.5 wt%, 5 wt%, and 10 wt%, were characterized, while preserving the overall SMB concentration at 50 wt% with respect to the aqueous Tween 20 (Figure 2.10). That is, all three bead types had the same, constant 50 wt% SMB concentration and varied only by the amount of MNPs embedded in the beads. By comparing the frequency sweep of each concentration of magnetic nanoparticles, we observed an increase in moduli with the microbead concentration. This is expected as an increase in the volume fraction of the MNPs will increase the attractive interactions and the gel strength of the magnetically aligned microbead system. This trend was also observed in the randomly distributed MNPs microbead system (2.12b), which suggests that this trend is independent of the orientation of the MNPs. We hypothesize that this increase is a result of the increasing magnetic

attraction when more magnetic material is embedded in the microbeads leading to magnetically induced gel strength. One simple, albeit semi-quantitative, way of checking this hypothesis is to normalize the shear moduli by the weight % of the MNPs that are used to lace them. For example, in the case of the microbeads with 2.5 wt% of MNPs, the overall weight of the MNPs in the gel was 1.25 wt% since the beads were 50 wt% in suspension. The curves for all normalized shear and loss moduli are plotted in Figure 2.11. As seen, the re-normalizing the rheology data resulted in good (but not complete) clustering of the curves highlighting a heuristic correlation between the weight % of MNPs in the microbeads and the viscoelasticity of the dispersion. This allows to design simple rules for gel formulation. Further interpretation of the magnetic gelation data required measurement of the magnetic polarizability of the soft microbead system, which is described in the next section.

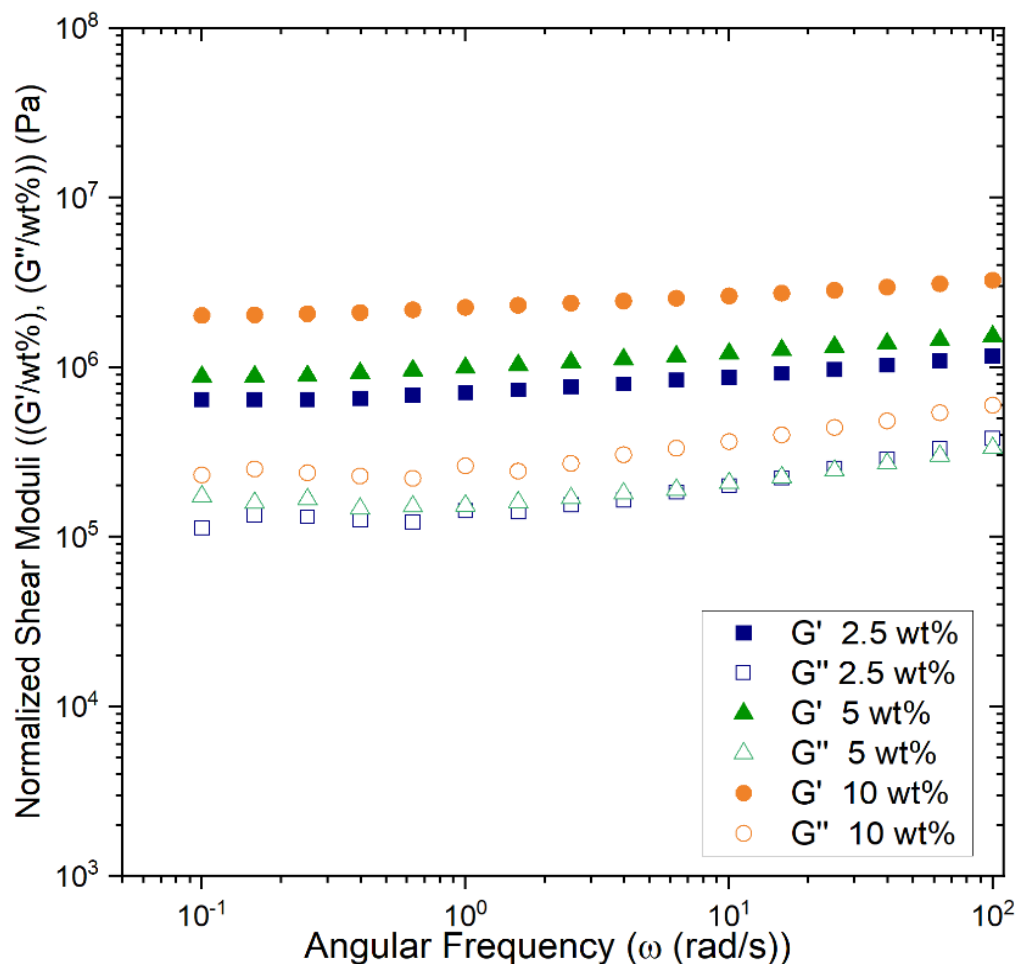


**Figure 2.11.** Normalized storage,  $G'$ , and loss,  $G''$ , moduli for magnetic microbeads with 2.5 wt%, 5 wt%, and 10 wt% aligned MNPs embedded in the SMB PDMS matrix. The normalization of the rheology data (by dividing the moduli by the wt% of MNPs) results in good (but not complete) clustering of the curves, highlighting a general correlation between the weight % of MNPs in the microbeads and the viscoelasticity of the dispersion.

### 2.3.6 Magnetometry characterization of the microbeads

The data for particle structuring and gelation indicate the key role of the particle polarizability and remanent magnetic polarization in governing the viscoelastic properties of the suspensions. In order to evaluate these effects, the magnetic properties of the particle suspensions were

investigated with a SQUID magnetometer. The samples were measured in unidirectional magnetic field ( $\pm 2$  T) at room temperature, atmospheric pressure in a water/glycerol liquid mixture to reduce sedimentation during the experiment. The magnetization curve is determined by measuring the change in the net moment of the suspension upon increasing and decreasing external magnetic field cycles.

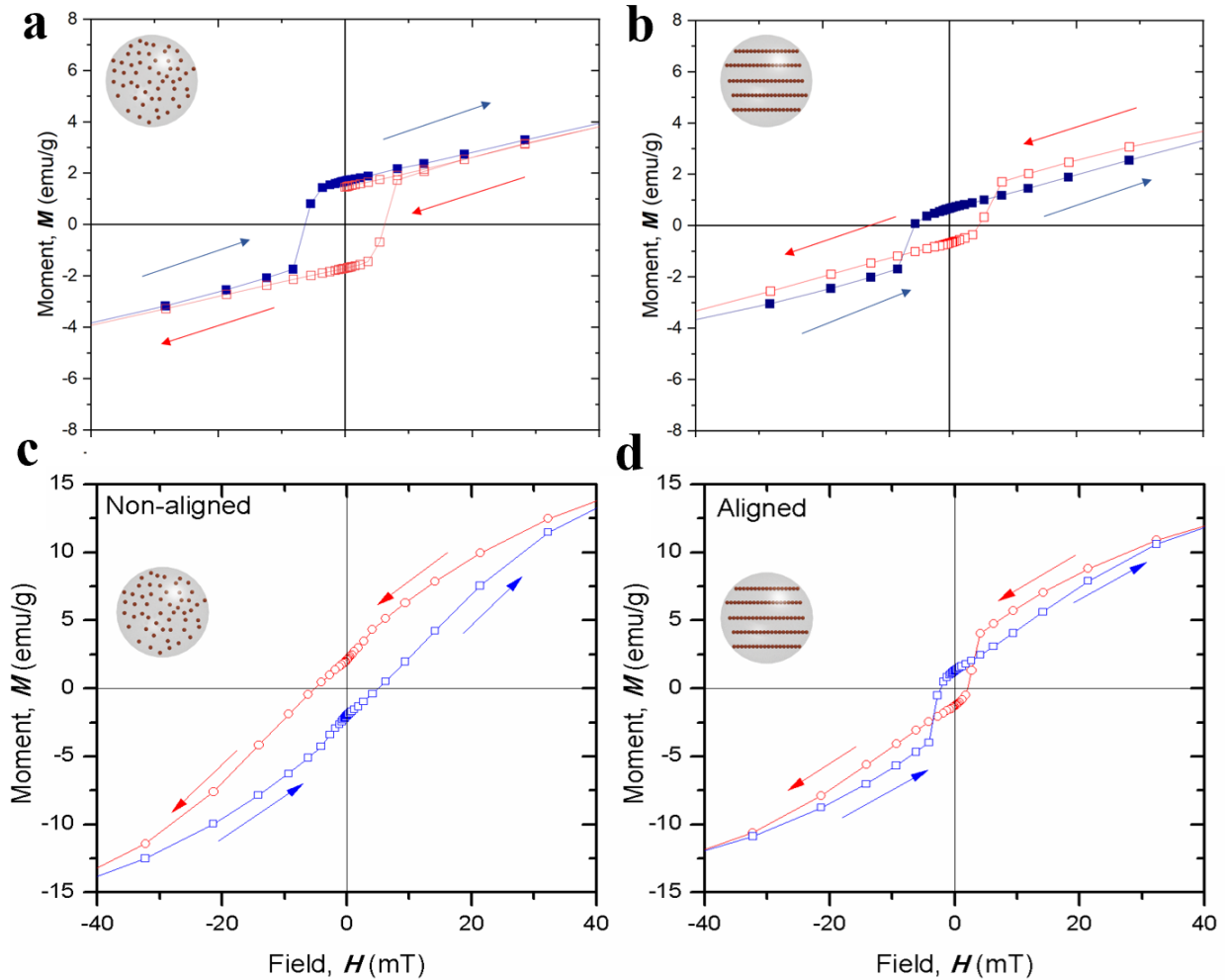


**Figure 2.12** These curves represent the normalized magnetic moment of the beads containing either 5 wt% (a,b) or 10 wt% (c,d) of MNPs as a function of the applied magnetic field. The arrows indicate the scan direction, when the applied field goes up or down during the measurement. Magnetization curves for (a) microbeads with 5 wt% randomly distributed MNPs and the (b) microbeads with 5 wt% embedded, magnetically aligned MNPs, (c) microbeads with 10 wt% randomly distributed MNPs and the (d) microbeads with 10 wt% embedded, magnetically aligned MNPs.

The magnetization curves for microbeads containing 10 wt% MNPs in the non-aligned configuration show hysteresis which is characteristic of ferromagnetic material (Figure 2.12c). The residual moment of a microbead can be evaluated from this data by  $\mu_r = M(\text{at } H = 0) \times m$ , where  $M(\text{at } H = 0)$  is the residual magnetic moment and  $m$  is the mass of MNPs within a microbead. We estimate that the residual moment in each microbead with non-aligned MNPs is  $\mu_r \sim 3.3 \times 10^{-14} \text{ Am}^2$ . The determination of magnetic moment of a bead with aligned chains is non-trivial due to an anomaly in the magnetometry (discussed below). By assuming a linear decrease of the moment in the demagnetizing field in the region  $H < 20 \text{ mT}$ , we estimate a retentivity by extrapolating magnetometry data to  $H = 0 \text{ mT}$ . We find that the residual magnetic moment of a bead with aligned nanoparticle chains (10 wt%) is  $\mu_r \sim 1.8 \times 10^{-13} \text{ Am}^2$ . Here we use point-dipole approximation to estimate the interparticle interaction between two SMBs (of diameters =  $10 \mu\text{m}$ ). According to point-dipole approximation, the interaction energy ( $U_{\text{mag}}$ ) between two interacting dipoles  $i$  and  $j$  is given as<sup>57</sup>

$$U_{\text{mag}} = \frac{1}{r_{ij}^3} \left[ \mu_i \cdot \mu_j - 3 \frac{(\mu_i \cdot \mathbf{r}_{ij})(\mu_j \cdot \mathbf{r}_{ij})}{r_{ij}^2} \right]$$

where  $\mu$  is the dipole moment, and  $\mathbf{r}_{ij}$  is the position vector joining the centers of the interacting particles. We recognize that the point-dipole approximation only provides a crude estimation of the interaction energy, and the effects of mutual polarization and multibody interactions of the beads should be taken into account for a precise determination of the energy, especially at short separations.<sup>58-60</sup> Here we use the point-dipole model to provide a qualitative relationship between the interaction energy among beads with aligned and non-aligned MNPs, and a more comprehensive analysis would be necessary for obtaining absolute magnetic energy of the ensemble, which is beyond the scope of this dissertation.

### ***2.3.7 Interaction Energy of the Microbeads***

The calculated interaction energy as a function of the separation between two identical microbeads of diameter 10  $\mu\text{m}$  with non-aligned and aligned MNPs is plotted in Figure 2.13. We find that the interaction energy between the microbeads at surface contact is significantly higher than the thermal energy (i.e.,  $kT$ ,  $k$  being the Boltzmann constant and  $T$  the temperature) but it rapidly decreases upon increasing the interparticle separation. The larger moment of the beads with aligned MNPs in comparison to beads with non-aligned MNPs results in a much stronger interaction which leads to the persistence of the chained network-like structure of beads with aligned MNPs even upon turning off the magnetic field (Figure 2.4 and Figure 2.13). However, the interaction energy calculations based on magnetometry data suggest that the microbeads with non-aligned MNPs would retain their assembled structure, as interaction energy exceeds thermal fluctuations, which is not observed in the experiments (Figure 2.4). This discrepancy points to the role of non-magnetic repulsive interactions such as electrical double layer repulsions and localized hydrodynamic interactions in the microbead suspensions,<sup>2</sup> which lead to disruptive energies larger than simple thermal diffusion. Further work on mathematical modeling of such interactions would be necessary to fully understand the unusual experimental behavior of the microbeads.

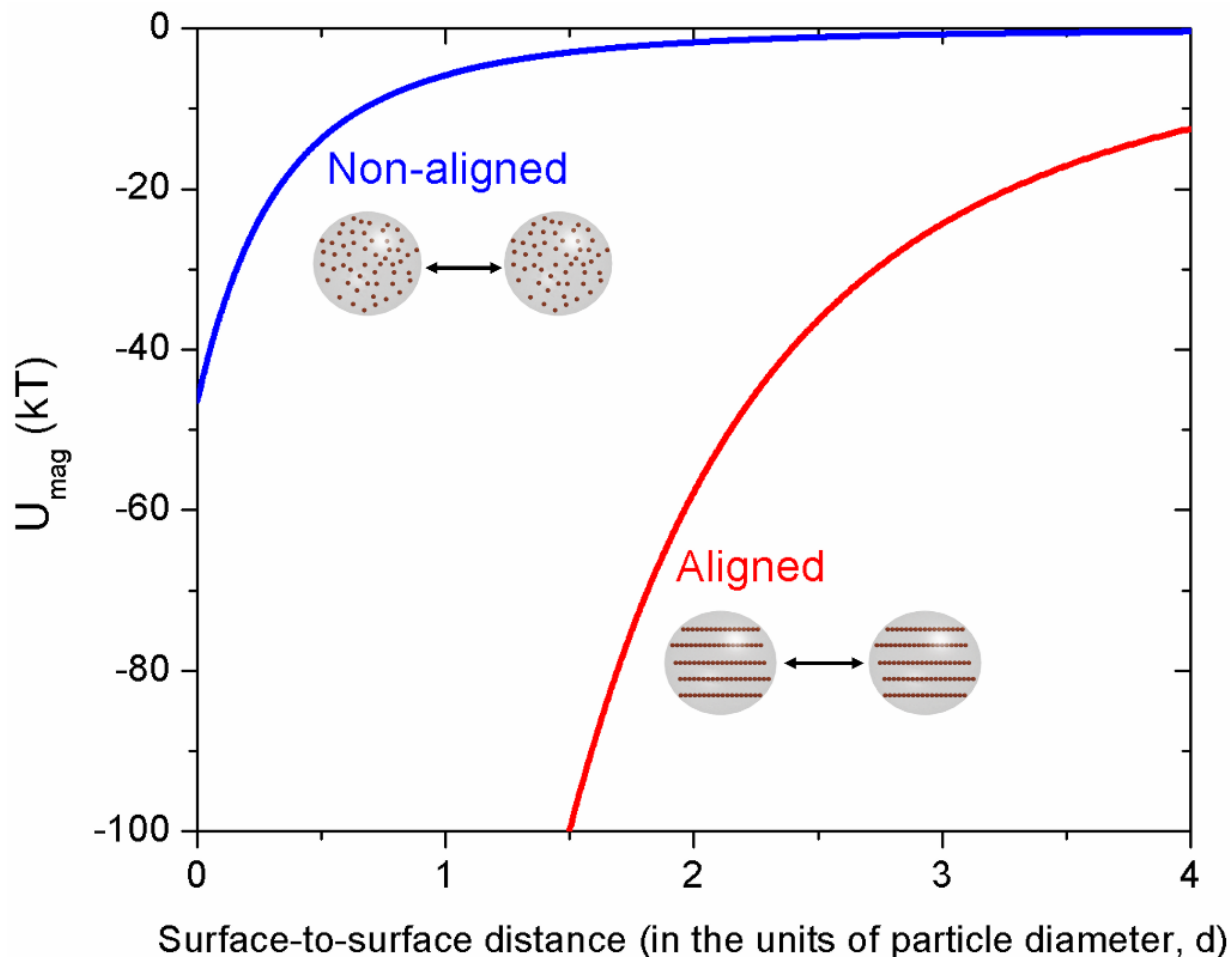


**Figure 2.13** Estimated interaction energy between two PDMS microbeads with 10 wt%, non-aligned and aligned MNPs embedded in the PDMS matrix ( $d = 10 \mu\text{m}$ ).

The microbeads with aligned MNPs show a peculiar split hysteresis loop (Figure 2.12d). This unusual loop is a signature of dynamical changes occurring in the liquid suspension during the magnetization and de-magnetization cycles. It is to be noted that no such split hysteresis has been reported previously for colloidal dispersions and the origin of this behavior has not been reported. We were, however, able to observe the same split hysteresis for our sample of 5 wt% magnetically aligned PDMS beads as well (2.12b). The alignment of the MNP chains within the PDMS matrix render the particle magnetically anisotropic. We believe that following two factors

may contribute to split hysteresis: (a) Free rotation and reorientation of the microbeads in the suspension upon decreasing the field from the magnetic saturation (at  $\sim 100$  mT); and (b) Reversal of magnetization via domain wall movement. In our case, the magnetometry was performed in liquid suspensions where the particles are free to reorient. Here upon decreasing the magnetic field from its saturation point, the particles may reorient while partially preserving their magnetic moment, thus leading to the observed split hysteresis where at low field  $\sim 10$  mT, an inversion of the magnetic polarity is observed. Additionally, it has been shown that for magnetically anisotropic films the split hysteretic loop exists due to the reversal of magnetization at the edges of the film due to domain wall movement upon decreasing the field.<sup>61-63</sup> In our case the SMBs possess magnetic anisotropy. Due to the presence of aligned MNPs in the SMBS, the edges of the particles may show a reversal of magnetization in demagnetizing field and such effect dominates near the switching fields i.e.,  $-10$  to  $+10$  mT. We recognize that based on our experiments it is not feasible to predict the relative contributions of the two factors mentioned above leading to the observed split hysteretic behavior of microbeads with aligned MNPs chains. Further experimental and theoretical investigations are necessary to interpret the unusual observed magnetic behavior of our colloidal SMBs in magnetization-demagnetization-re-magnetization cycles.

### 2.3.8 Long-range organization of the microbeads in weak magnetic fields

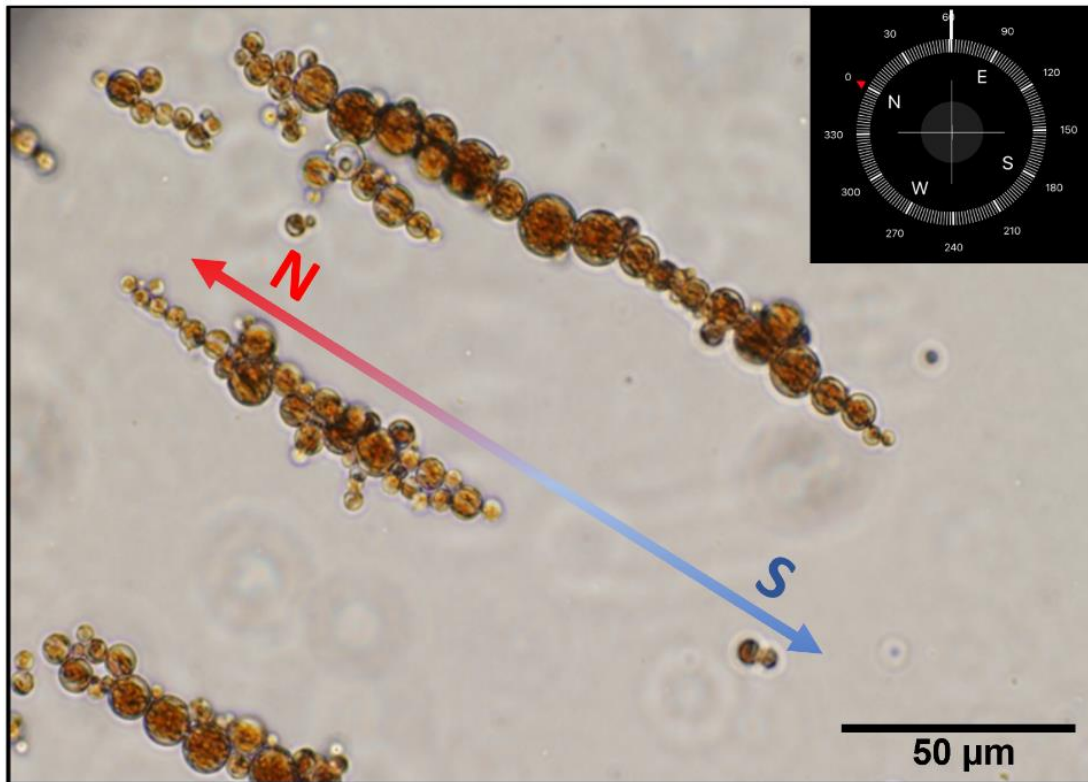


**Figure 2.14** The magnetic microbeads orient and organize in ways so that the embedded magnetic particle chains face the same direction and form linear structures that align in the direction of Earth's magnetic field (sample is 10 wt% MNPs in SMBs, the direction of the Earth' field is shown in the compass sensor image). Such orientation presents a fascinating analogy with the one observed with magnetotactic bacteria in nature.

One of the intriguing behaviors observed with the PDMS beads with aligned particle chains is the long-distance alignment of both the particle chains and the MNP chains inside them in the same angular direction. This phenomenon, which is observed in dilute systems with distinct individual microbead chains is illustrated by the micrograph in Figure 2.14. We hypothesized that

the alignment is caused by the Earth magnetic field, similarly to the orientation of compass needles. To check that prediction, a compass was used to determine the direction of Earth's magnetic field and it was confirmed that the microbeads align colinearly with the Earth magnetic north-south axis.

The origin of this alignment requires theoretical evaluation, as the beads and even their assemblies are orders of magnitude smaller than the typical compass magnet. Thus, we evaluated the energy of orientation of the beads in the Earth's magnetic field. The energy of a magnetic dipole ( $\mu$ ) in a uniform magnetic field ( $\mathbf{B}$ ) is given as  $U_d(\theta) = -\mu \cdot \mathbf{B} = -\mu B \cos \theta$ , where  $\theta$  is the angle between the dipole moment vector and the direction of the magnetic field.<sup>64</sup> Therefore, the change in energy upon rotating a dipole from orientation  $\theta_1$  to  $\theta_2$  is estimated as  $\Delta U_d = -\mu B (\cos \theta_2 - \cos \theta_1)$ . The origin of the reorientation of a dipole in the external field is the lowering of configuration energy given by  $\Delta U_d$ . Here we assume that  $\Delta U_d = kT$  i.e., at least 1  $kT$  energy is required to reorient the dipole. The minimum dipole moment of such a particle which will reorient from  $45^\circ$  to  $0^\circ$  in Earth's magnetic field ( $\sim 4 \times 10^{-5}$  T) is  $\sim 3.5 \times 10^{-16}$  A m<sup>2</sup>, which is  $\sim 1/100^{\text{th}}$  of the dipole moment of our microbeads (see previous section). Therefore, in dilute systems where the microbeads could rotate freely, they would align along the magnetic north-south axis.

The phenomenon of long-range arrangement has a fascinating biomimetic analogy. As mentioned in the introduction, a broadly similar phenomenon of MNPs chains orientation in living matter is observed in the alignment of magnetotactic bacteria in Earth's magnetic field. The SMBs' response to the Earth's magnetic field due to their residual magnetic polarization could also influence the physical understanding and interpretation of the structure formation in such systems. The modeling of dipolar particles structuring to date assumes a system with random initial dipolar orientation.<sup>5,18</sup> The imposition of Earth's or other weak fields could affect both the directionality

and length scale of the resulting percolated structures. At this stage it is not immediately clear whether the alignment of the individual SMB chains along the Earth magnetic field, observed in the thin chamber, would affect the properties and behavior of the dense 3D SMB systems such as the gels described in the previous section. While this effect is much weaker than the electromagnetic actuation in the experimental cell, the structural impact of the beads' pre-alignment by the Earth's field, or other weak fields, warrants further theoretical and experimental investigation.

## **2.4 Concluding remarks**

The work presented in this Chapter was made possible by the introduction of a class of soft magnetic beads that combines two useful features of their constituent materials – the use of matrix of common PDMS elastomer and the magnetic responsivity of the embedded MNPs. Notably, the synthesis of these soft beads by emulsification procedure is nontrivial in addressing the need to produce droplets of uniform size and relatively narrow size distribution in this size range. We produced relatively uniform droplets by shearing of the liquid silicone precursor in PVA solution with matching viscosity.<sup>45</sup> The elastomer microbeads were proven to be a colloidal system that is easy to make and scale up to macroscopic quantities, while the internal structure of the MNPs in the SMBs could be controlled by external field.

These magnetic microbeads can serve as an experimental toolbox for modelling interactions in dipolar systems, leading to various percolated networks, novel magneto-rheological materials, and smart gels. The formation of percolated networks in similar types of interacting dipolar systems has been predicted and modelled theoretically by Hall and collaborators.<sup>46-50,54</sup> We showed that the interactions and structure formation of the SMB systems could be drastically

changed by aligning the embedded magnetic nanoparticles. We proved through microscopy that the microbeads formed different percolated networks structures depending on the magnetically alignment of the MNPs. It was demonstrated that an external magnetic field could direct the assembly of the system and that the aligned microbeads re-assembled into long-ranged chains after dispersion. We showed that these soft micromagnet SMBs with aligned MNPs have residual polar magnetization and gel-like properties. We proved the tunability of this system by conducting magnetization, demagnetization, and re-magnetization experiments that were evidence of the reformation of percolating networks.

The use of these beads as model systems in understanding and controlling the magnetic interactions could in the future be enhanced in a variety of ways. First, further improvements of the particle synthesis procedures could enable more precise control and uniformity of the MNP chains in the SMB matrix (including making SMBs with a single coaxial MNP chain). It might be possible to incorporate microfluidics in order to increase monodispersity in the SMBs size, if desired or even to be able to visualize the individual MNPs embedded in the SMBs as done by Chen et al.<sup>65</sup> The chain structure and distribution in the SMBs can be visualized by using 3D electron tomography. Second, better understanding of the fundamentals of two-body and multibody interactions could benefit the modeling and control. Two-bead interactions could be measured by methods such as analysis of distribution of distances between particles or by capturing beads with optical tweezers and AFM. Finally, pre-alignment with weak fields could be used to improve the connectivity and other structural aspects of the final soft gel materials.

These beads can also be used in several applied areas. The transparent beads with aligned chains can serve as convenient microprobes in visualizing even very weak magnetic fields on the microscale. Such particles can also be used in biomedical applications, as particles that can be

magnetically moved and guided are promising in applications such as drug delivery and cancer therapies<sup>66,67</sup> Our microbeads with aligned MNPs have the potential to be used as vehicles for applications such as targeted delivery, as they can be easily loaded with molecular “cargo” and their alignment and location can be precisely controlled by an external magnetic field. Finally, as the method is easily scalable, these classes of elastomeric magnetic beads can find applications in larger-scale “smart” stimuli-responsive materials with switchable phase transitions.

## **2.5 Acknowledgements**

The authors express gratitude to Professor Carol K. Hall for numerous research collaborations, collegial interactions, inspiration, and leadership. NC and OV acknowledge financial support from the National Science Foundation (NSF) awards CBET-1604116 and CBET-1935248. The contributions to the manuscript by BB were supported by NSF award CBET-2038305. We thank Dr. Lilian Hsiao for the use of the rheometer, Dr. Lewis Reynolds for assistance with magnetometry measurements and discussions, and Dr. Joseph Tracy for the valuable discussions on magnetic properties of the MNPs and SMBs.

## 2.6 References

1. Blakemore, R.P. Magnetotactic Bacteria. *Ann. Rev. Microbiol.* **1982**, *36*, 217-238.
2. Bharti, B. and Veleev, O.D. Assembly of Reconfigurable Colloidal Structures by Multidirectional Field-Induced Interactions. *Langmuir* **2015**, *31*, 7897-7908.
3. Lalitha, K.; Prasad, Y.S.; Sridharan, V.; Maheswari, C.U.; John, G.; Nagarajan, S. A renewable resource-derived thixotropic self-assembled supramolecular gel: magnetic stimuli responsive and real-time self-healing behaviour. *RSC Adv.* **2015**, *5*, 77589–77594.
4. Ahn, S-K.; Kasi, R.M.; Kim, S-C. Sharma, N.; Zhou, Y. Stimuli-responsive polymer gels. *Soft Matter* **2008**, *4*, 1151-1157.
5. Goyal, A.; Hall, C.K.; Veleev, O.D. Bicontinuous gels formed by self-assembly of dipolar colloid particles. *Soft Matter* **2010**, *6*, 480–484.
6. Huang, H-W.; Huang, T-Y.; Charilaou, M.; Lyttle, S.; Zhang, Q.; Pané, S.; Nelson, B.J. Investigation of Magnetotaxis of Reconfigurable Micro-Origami Swimmers with Competitive and Cooperative Anisotropy. *Adv. Funct. Mater.* **2018**, *1802110*, 1-9.
7. Prileszky, T.A. and Furst, E.M. Magnetite nanoparticles program the assembly, response, and reconfiguration of structured emulsions. *Soft Matter* **2019**, *15*, 1529-1538.
8. Erb, R.M.; Martin, J.J.; Soheilian, R.; Pan, C.; Barber, J.R. Actuating Soft Matter with Magnetic Torque. *Adv. Funct. Mater.* **2016**, *26*, 3859–3880.
9. Hodaei, A.; Akhlaghi, O.; Khani, N.; Aytas, T.; Sezer, D.; Tatli, B.; Menciloglu, Y.Z.; Koc, B.; Akbulut, O. Single Additive Enables 3D Printing of Highly Loaded Iron Oxide Suspensions. *ACS Appl. Mater. Interfaces* **2018**, *10*, 9873–9881.
10. Tracy, J.B. & Crawford, T.M. Magnetic field-directed self-assembly of magnetic nanoparticles. *MRS Bulletin.* **2013**, *28*, 915-920.
11. Ponton, A.; Bee, A.; Talbot, D.; Perzynski, R. Regeneration of thixotropic gels studied by mechanical spectroscopy: the effect of pH. *J. Phys. Condens. Matter.* **2005**, *17*, 821–836.

12. Wang, M. and Yin, Y. Magnetically Responsive Nanostructures with Tunable Optical Properties. *J. Am. Chem. Soc.* **2016**, *138*, 6315–6323.
13. Zhang, J.; Huang, Q.; Du, J.; Recent advances in magnetic hydrogels. *Polym. Int.* **2016**, *65*, 1365–1372.
14. Suwa, M.; Uotani, A.; Tsukahara, S. Alignment and small oscillation of superparamagnetic iron oxide nanoparticle in liquid under alternating magnetic field. *J. Appl. Phys.* **2019**, *125* (123901), 1-12.
15. Bharti, B.; Fameau, A.-L.; Velev, O.D. Magnetophoretic assembly of flexible nanoparticle/lipid microfilaments. *Faraday Discuss.* **2015**, *181*, 437-448.
16. Korth, B.D.; Keng, P.; Shim, I.; Bowles, S.E.; Tang, C.; Kowalewski, T.; Nebesny, K.W.; Pyun, J. Polymer-Coated Ferromagnetic Colloids from Well-Defined Macromolecular Surfactants and Assembly into Nanoparticle Chains. *J. Am. Chem. Soc.* **2006**, *128*, 6562-6563.
17. Schmidle, H.; Jäger, S.; Hall, C.K.; Velev, O.D., Klapp, S.H.L. Two-dimensional colloidal networks induced by a uni-axial external field. *Soft Matter* **2013**, *9*, 2518-2524.
18. Schmidle, H.; Hall, C. K.; Velev, O.D.; Klapp, S.H.L. Phase Diagram of two-dimensional systems of dipole-like colloids. *Soft Matter* **2012**, *8*, 1521-1531.
19. Bharti, B.; Fameau, A.-L.; Rubinstein, M.; Velev, O.D. Nanocapillarity-mediated magnetic assembly of nanoparticles into ultraflexible filaments and reconfigurable networks. *Nat. Mater* **2015**, *14*, 1104-1109.
20. Schmauch, M.M.; Mishra, S.R.; Evans, B.A.; Velev, O.D.; Tracy, J.B. Chained Iron Microparticles for Directionally Controlled Actuation of Soft Robots. *ACS Appl. Mater. Interfaces* **2017**, *9*, 11895–11901.
21. Bharti, B.; Kogler, F.; Hall, C.K.; Klapp, S.H.L.; Velev, O.D. Multidirectional colloidal assembly in concurrent electric and magnetic field. *Soft Matter* **2016**, *12*, 7747-7758.

22. Spatafora-Salazar, A.S.; Lobmeyer, D.M.; Cunha, L.H.P.; Joshi, K.; Biswal, S.L. Hierarchical assemblies of superparamagnetic colloids in time-varying magnetic fields. *Soft Matter* **2021**, *17*, 1120-1155.
23. Wang, M.; He, L.; Yin, Y. Magnetic field guided colloidal assembly. *Mater. Today* **2013**, *16* (4), 110-116.
24. Roh, S. & Velev, O.D. Nanomaterials Fabrication by Interfacial Templating and Capillary Engineering in Multiphasic liquids. *AIChE* **2018**, *64*, 3558-3564.
25. Byrom, J. and Biswal, S.L. Magnetic field directed assembly of two-dimensional fractal colloidal aggregates. *Soft Matter* **2013**, *9*, 9167-9173.
26. Kim, M.W.; Han, W.J.; Kim, Y.H.; Choi, H.J. Effect of a hard magnetic particle additive on rheological characteristics of microspherical carbonyl iron-based magnetorheological fluid. *Colloids and Surf.A: Physiochem. Eng. Aspects* **2016**, *506*, 812-820.
27. Liu, X.; Ceballos, A.; Streubel, R.; Jiang, Y.; Chai, Y.; Kim, P.Y.; Forth, J.; Hellman, F.; Shi, S.; Wang, D.; Helms, B.A. Ashby, P.D.; Fischer, P.; Russell, T.P. Reconfigurable ferromagnetic Liquid droplets. *Science* **2019**, *365*, 264–267.
28. Yu, M.; Ju, B.; Liu, S.; Choi, S-B. Magnetoresistance Characteristics of Magnetorheological Gel under a Magnetic Field. *Ind. Eng. Chem. Res.* **2014**, *53*, 4704–4710.
29. Sorokina, O.N.; Kovarski, A.L.; Lagutina, M.A.; Dubrovskii, S.A.; Dzheparov, F.S. Magnetic Nanoparticles Aggregation in Magnetic Gel Studied by Electron Magnetic Resonance (EMR). *Appl. Sci.* **2012**, *2*, 342-350.
30. Menzel, A.M. Bridging from particle to macroscopic scales in uniaxial magnetic gels. *J. Chem. Phys.* **2012**, *141* (194907), 1-13.
31. Fameau, A.L.; Lam, S.; Velev, O.D. Multi-stimuli responsive foams combining particles and self-assembling fatty acids. *Chem. Sci.* **2013**, *4*, 3874-3881.

32. Lam, S.; Blanco, E.; Smoukov, S.K.; Velikov, K.P.; Velev, O.D. Magnetically Responsive Pickering Foams. *J. Am. Chem. Soc.* **2011**, *133*, 13856-13859.
33. Blanco, E.; Lam, S.; Smoukov, S.K.; Velikov, K.P.; Khan, S.A.; Velev, O.D. Stability and Viscoelasticity of Magneto-Pickering Foams. *Langmuir* **2013**, *29*, 10019–10027.
34. Mishra, S.R.; Dickey, M.D.; Velev, O.D.; Tracy, J.B. Selective and directional actuation of elastomer films using chained magnetic nanoparticles. *Nanoscale* **2016**, *8*, 1309-1313.
35. Tarama, M.; Cremer, P.; Borin, D.Y.; Odenbach, S.; Lowem, H.; Menzel, A.M. Tunable dynamic response of magnetic gels: Impact of structural properties and magnetic fields. *Phys. Rev.* **2014**, *90*, 1-9.
36. Biswal, S.L.; Gast, A.P. Micromixing with Linked Chains of Paramagnetic Particles. *Anal. Chem.* **2004**, *76*, 6448-6455.
37. Faraudo, J.; Andreu, J.S.; Calero, C.; Camacho, J. Predicting the Self-Assembly of Superparamagnetic Colloids under Magnetic Fields. *Adv. Funct. Mater.* **2016**, *26*, 3837–3858.
38. Tokarev, A.; Gu, Y.; Zakharchenko, A.; Luzinov, I.; Kornev, K.G.; Minko, S. Reconfigurable Anisotropic Coatings via Magnetic Field-Directed Assembly and Translocation of Locking Magnetic Chains. *Adv. Funct. Mater.* **2014**, *24*, 4738–4745.
39. Tadic, M.; Kralj, S.; Kopanja, L. Synthesis, particle shape characterization, magnetic properties and surface modification of superparamagnetic iron oxide nanochains. *Mater. Charact.* **2019**, *148*, 123-133.
40. Kralj, S. and Makovec, D. Magnetic Assembly of Superparamagnetic Iron Oxide Nanoparticle Clusters into Nanochains and Nanobundles. *ACS Nano* **2015**, *9* (10), 9700-9707.
41. Huang, S.; Pessot, G.; Cremer, P.; Weeber, R.; Holm, C.; Nowak, J.; Odenbach, S.; Menzel, A.M.; Auernhammer, G.K. Buckling of paramagnetic chains in soft gels. *Soft Matter*, **2016**, *12*, 228-237.

42. He, L.; Hu, Y.; Han, X.; Lu, Y.; Lu, Z.; Yin, Y. Assembly and Photonic Properties of Superparamagnetic Colloids in Complex Magnetic Fields. *Langmuir* **2011**, *27*, 13444-13450.
43. Zubarev, A.Y.; Chirikov, D.N.; Borin, D.Y.; Stepanov, G.V. Hysteresis of the magnetic properties of soft magnetic gels. *Soft Matter* **2016**, *12*, 6473-6480.
44. Oh, J.K.; Park, J.M. Iron oxide-based superparamagnetic polymeric nanomaterials: Design, preparation, and biomedical application. *Prog. Polym. Sci.* **2011**, *36*, 168–189.
45. Roh, S.; Okello, L.B.; Golbasi, N.; Hankwitz, J.P.; Liu, J. A.-C; Tracy, J.B.; Velev, O.D. 3D-Printed Silicone Soft Architectures with Programmed Magneto-Capillary Reconfiguration. *Adv. Mater. Technol.* **2019**, *4* (1800528), 1-7.
46. Goyal, A.; Hall, C.K.; Velev, O.D. Self-assembly in binary mixtures of dipolar colloids: Molecular dynamics simulations. *J. Chem. Phys.* **2010**, *133* (064511) 1-10.
47. Rutkowski, D.M.; Velev, O.D.; Klapp, S.H.L.; Hall, C.K. Simulation study on the structural properties of colloidal particles with offset dipoles. *Soft Matter* **2017**, *13*, 3134-3146.
48. Liao, G-J.; Hall, C.K.; Klapp, S.H.L. Dynamical self-assembly of dipolar active Brownian particles in two dimensions. *Soft Matter*, **2020**, *16*, 2208-2223.
49. Rutkowski, D.M.; Velev, O.D.; Klapp, S.H.L.; Hall, C.K. The effect of charge separation on the phase behavior of dipolar colloidal rods. *Soft Matter*, **2016**, *12*, 4932-4943.
50. Maloney, R.C.; Hall, C.K. Clustering and Phase Separation in Mixtures of Dipolar and Active Particles in an External Field. *Langmuir*, **2020**, *36*, 6378–6387.
51. Kogler, F.; Velev, O.D.; Hall, C.K.; Klapp, S.H.L. Generic model for tunable colloidal aggregation in multidirectional fields. *Soft Matter* **2015**, *11*, 7356-7366.
52. Baynes, T.M.; Russell, G.J.; Bailey, A. Comparison of Stepwise Demagnetization Techniques. *IEEE Trans. Magn.*, **2002**, *38*, (4), 1753-1758.

53. Smoukov, S.K.; Gangwal, S.; Marquez, M.; Velev, O.D. Reconfigurable responsive structures assembled from magnetic Janus particles. *Soft Matter* **2009**, *5*, 1285–1292.
54. Goyal, A.; Hall, C.K.; Velev, O.D. Phase diagram for stimulus-responsive materials containing dipolar colloidal particles. *Phys. Rev. E* **2008**, *77* (031401), 1-6.
55. Winter, H.H. and Chambon, F. Analysis of Linear Viscoelasticity of a Crosslinking Polymer at the Gel Point. *J. Rheol.* **1986**, *30* (2), 367-382.
56. Barrera, C.; Florián-Algarin, V.; Acevedo, A.; Rinaldi, C. Monitoring gelation using magnetic nanoparticles. *Soft Matter* **2010**, *6*, 3662-3668.
57. Harraq, A.A.; Lee, J.G.; Bharti, B. Magnetic field-driven assembly and reconfiguration of multicomponent supraparticles. *Sci. Adv.* **2020**, *6* (19), 1-9.
58. Komarov, K.A.; Kryuchkov, N.P.; Yurchenko, S.O. Tunable interactions between particles in conically rotating electric fields. *Soft Matter*, **2018**, *14*, 9657-9674.
59. Komarov, K.A. & Yurchenko, S.O. Colloids in rotating electric and magnetic fields: designing tunable interactions with spatial field hodographs *Soft Matter*, **2020**, *16*, 8155—8168.
60. Komarov, K.A.; Yarkov, A.V.; Yurchenko, S.O. Diagrammatic method for tunable interactions in colloidal suspensions in rotating electric or magnetic fields *J. Chem. Phys.* **2019**, *151*, (244103) 1-16.
61. Oepen, H.P.; Millev, Y.T.; Ding, H.F.; Pütter, S.; Kirschner, J. Field-driven reorientation in ultrathin ferromagnetic films with uniaxial anisotropy. *Phys. Rev. B.* **2000**, *61* (14), 9506-9512.
62. Tao, X.D.; Wang, H.L.; Miao, B.F.; Sun, L.; You, B.; Wu, D.; Zhang, W.; Oepen, H.P.; Zhao, J.H.; Ding, H.F. Unveiling the Mechanism for the Split Hysteresis Loop in Epitaxial  $\text{Co}_2\text{Fe}_{1-x}\text{Mn}_x\text{Al}$  Full-Heusler Alloy Films. *Sci. Rep.* **2015**, *6* (18615), 1-9.

63. Dumm, M.; Zölfl, M.; Moosbühler, R.; Brockmann, M.; Schmidt, T.; Bayreuther, G. Magnetism of ultrathin FeCo (001) films on GaAs(001). *J. Appl. Phys.* **2000**, *87*, 5457-5459.
64. Urone, P. P.; Hinrichs, R.; Dirks, K.; Sharma, M. *College Physics*. Houston, Texas: OpenStax College, Rice University, 2013. Print.
65. Chen, C-H.; Abate, A.R.; Lee, D.; Terentjev, E.M.; Weitz, D.A. Microfluidic Assembly of Magnetic Hydrogel Particles with Uniformly Anisotropic Structure. *Adv. Mater.* **2009**, *21*, 3201–3204.
66. Nair, B.G.; Nagaoka, Y.; Morimoto, H.; Yoshida, Y.; Maekawa, T.; Kumar, D.S. Aptamer conjugated magnetic nanoparticles as nanosurgeons. *Nanotechnology*, **2010**, *21* (455102), 1-8.
67. Weeber, R.; Hermes, M.; Schmidt, A.M.; Holm, C. Polymer architecture of magnetic gels: a review. *J. Phys. Condens. Matter*, **2018**, *30*, 1-26.

## CHAPTER 3

### Design and Characterization of Novel Magnetocapillary Gels

#### 3.1 Introduction

Capillary forces can be described as the result of interactions between particles that are mediated by fluid interfaces.<sup>1,2</sup> The importance of these types of forces has been acknowledged for decades due to their relevance in the self-assembly of microscopic particles. Capillary forces can be described in terms of two sub-categories: normal capillary bridge forces and lateral capillary forces.<sup>1</sup> For the purpose of this Chapter, we will be focusing on capillary bridging forces. In this type of capillary force, the liquid phase forms capillary bridges between two particles and the capillary forces are thus normal to the planes of the contact lines in the particles' surface.<sup>1,3</sup>

Gels can be classified as chemical or physical. Physical gels are formed by interactions such as van der Waals interactions, electrostatic interactions, and capillary forces.<sup>4</sup> One way to characterize gel suspensions and gels is through rheology, which provides a way to study the sample's mechanical properties. A sample is characterized by the presence of a storage modulus  $G'(\omega)$  and a loss modulus  $G''(\omega)$  which are a function of angular frequency,  $\omega$ . A physical solid-like gel such is a sample with  $G'(\omega)$  being considerably greater than  $G''(\omega)$  in the plateau region and with the absence of an equilibrium modulus.<sup>5</sup> Capillary gels can be classified as particle suspensions with an immiscible secondary liquid.<sup>6</sup> By introducing this secondary liquid, the system is able to form capillary bridges between the spherical particles such that a structure formation is obtained. The amount of secondary fluid required can vary depending on the system being studied but has been shown to be as little as 0.1 wt%.<sup>7</sup>

Stimuli-responsive or "smart" polymer gels are a new class of soft matter that can be designed to respond to applied stimuli<sup>5,8</sup> such as pH, thermal, and an electrical or magnetic field.

These types of gels are of interest because they can find applications in a variety of industries including therapy agents and drug delivery.<sup>9</sup> Incorporating magnetic nanoparticles into a gel enables the gels to be magnetically responsive. Gels with a stimuli response to a magnetic field have gained interest because they allow for tunability with the applied, external applied field and can thus be remotely actuated.<sup>10-12</sup> Typical magnetic gels incorporate materials that include  $\text{Fe}_2\text{O}_3$ ,  $\text{Fe}_3\text{O}_4$  as well as iron nitride particles and metal alloys that include Fe, Ni, or Fe. Magnetic elastomer materials, specifically, are one type of responsive structures. These composite magnetic materials are convenient to make and use due to the decrease in nanoparticle aggregation caused by the introduction of the elastomer matrix.<sup>13</sup> By incorporating components such as magnetic nanoparticles, the system's assembly can be controlled with the application of an external magnetic field.<sup>8</sup>

In the previous Chapter, we introduced two types of soft magnetic microbeads (SMBs) which differ by the alignment of the embedded iron oxide ( $\text{Fe}_2\text{O}_3$ ) nanoparticles.<sup>13</sup> In this Chapter, we aim to prepare and use SMBs without embedded magnetic alignment as well as the control PDMS beads with no magnetic component into two types of magnetically responsive capillary gels (MRCGs). We investigate their rheological and magnetic properties to determine if the location of the magnetic material, as well as the capillary interactions, can control their properties depending on the location of the MNPs.

## **3.2 Materials and Methods**

**3.2.1 Non-magnetic PDMS beads** The synthesis of microbeads from PDMS includes emulsification and crosslinking of PDMS by precursor and curing agent. Just as in Chapter 2, we use the recommended 10:1 PDMS precursor base: crosslinker ratio. First, 14 wt% polyvinyl

alcohol (PVA) solution was made by heating and stirring for two hours to 100 g of deionized (DI) water (18.2 M $\Omega$  cm at 25 °C, obtained from a Millipore Milli-Q Academic water purification system) at 120 °C, to which we added 16.28 g of polyvinyl alcohol (PVA) (Mowiol 18-88, Sigma-Aldrich) in a covered beaker. The exact weight % of the PVA in solution was determined gravimetrically. The PVA-water solution (40 mL) was then placed in a beaker and mixed. The addition of the PVA to the water phase allowed the formation of much more uniform droplets.<sup>14</sup>

The 10:1 mixture of PDMS: crosslinker Sylgard 184 was then injected into the 14% PVA solution while it was being mixed and the suspension was stirred at 150 RPM for 10 minutes to ensure homogenization. The emulsion was then refined further by mixing at 250 RPM for an hour. Once the mixing was complete, the emulsion was placed in an oven at 60 °C overnight to accelerate the crosslinking process of the polymer matrix. The PDMS microbeads were then washed several times with a 0.1 wt% aqueous solution of Tween 20 using a vortex mixer and a centrifuge. Determination of the final weight percent of the PDMS dispersion was done gravimetrically and, in this Chapter, our chosen final weight percent was 50 wt% PDMS microbeads in an aqueous solution of 0.1 wt% Tween 20.

### ***3.2.2 Dispersing the magnetic nanoparticles within the PDMS precursor medium***

10 wt% iron (III) oxide nanoparticles (20 nm, MKNano) were added to 36 g tetrahydrofuran (THF) in a round bottom flask and sonicated for one hour. THF was added to temporarily reduce the viscosity of the PDMS precursor (Sylgard 184 obtained from Dow) such that the particles could be uniformly dispersed in the silicone base. The required amount of PDMS prepolymer was then added to the round bottom flask and the mixture was further sonicated for 5 hours to ensure uniform distribution of particles in the solvent. The THF was then evaporated from the mixture,

taking care that no magnetic component would affect the MNPs, leaving the PDMS precursor with internalized MNPs.

### ***3.2.3 Synthesis of PDMS beads containing randomly distributed MNPs***

The target loading of magnetic nanoparticles was 10 wt% with respect to the PDMS bead. That is, a magnetic bead contained 90 wt% PDMS and 10 wt% embedded MNPs. The synthesis of microbeads from PDMS includes emulsification and crosslinking of PDMS by precursor and curing agent like the non-magnetic PDMS beads described above. First, the 14 wt% PVA-water solution (40 mL) was placed in a beaker and mixed at 150 RPM in a mechanical mixer with an impeller, while the PDMS was mixed and degassed. Again, the addition of the PVA was necessary because of the large mismatch of the viscosity of PDMS in order to reduce polydispersity. The 10:1 mixture of PDMS/crosslinker Sylgard 184 was then injected into the 14% PVA solution while it was being mixed and the suspension was stirred at 150 RPM for ten minutes. The emulsion was then refined further by mixing at 250 RPM for 1 hour. The emulsion was placed in an oven at 60 °C overnight. PDMS microbeads were then washed several times with an aqueous solution of Tween 20 (0.1 wt%) using a vortex mixer and a centrifuge. Determination of the final weight percent of the PDMS beads dispersion was done gravimetrically and, in this chapter, our chosen final weight percent for these magnetic PDMS beads was also 50 wt% in aqueous solution of 0.1 wt% Tween 20.

### ***3.2.4 Synthesis of MRCG type 1: capillary bridging with MNPs***

#### **Magnetic oleic acid dispersion**

Most lipids with a melting point below room temperature may be used for the formation of capillary bridges between the PDMS microbeads and thus have an oil in water emulsion.<sup>15</sup> In this report, we chose oleic acid as the liquid phase. Spheroidal, 20 nm sized  $\gamma$ -Fe<sub>2</sub>O<sub>3</sub> superparamagnetic nanoparticles (MNPs, mkNANO) were added to the oleic acid (10% of the oleic acid mixture) and sonicated for 1 hour. Once sonicated, we were able to get a well dispersed suspension of magnetic oleic acid.

In this Chapter, we focus on making gels containing 10 wt, 20 wt%, 30 wt%, and 40 wt% magnetic oleic acid dispersed in PDMS bead suspension. In order to form the capillary network, we mixed the target amounts of the magnetic oleic acid described above with the PDMS bead suspension with a mechanical mixer with an impeller at high speed (650 RPM) for twenty minutes to make the gels. Then, we ground the gels with a mortar and pestle for five minutes to ensure complete mixing and gelation.

### ***3.2.5 Synthesis of MRCG type 2: Capillary bridging without MNPs***

These gels were composed of the PDMS beads with the embedded randomly distributed MNPs, and the capillary bridges were composed of non-magnetic oleic acid. These types of gels were also formed to contain 10 wt%, 20 wt%, 30 wt%, and 40 wt% oleic acid in the capillary bridges with respect to the total weight composition of the gels.

### ***3.2.6 Rheological Analysis of Capillary Gels***

Rheological analysis of the capillary gels was performed using a DHR-2, TA Instruments (New Castle, DE) rheometer with serrated parallel plate geometry (diameter = 40 mm with 0.5 mm gap size). Angular frequency sweeps were conducted at 1% strain for 0.01–100 rad s<sup>-1</sup>. The amplitude oscillatory measurements were conducted within the linear viscoelastic regime of the gels, which is the range where the storage ( $G'$ ) and the loss ( $G''$ ) moduli are independent of strain. The linear viscoelastic regime was determined by performing oscillatory strain sweeps at a constant angular frequency of 10 rad sec<sup>-1</sup>. All tests were run at a constant temperature of 25 °C.

### ***3.2.7 Optical Microscopy***

Optical microscopy (Olympus, BX-61) with an Olympus DP-70 digital CCD camera was used to characterize the morphology of the magnetic PDMS microbeads and the presence of the oleic acid capillary bridges.

### ***3.2.8 Self-Repair Testing***

Self-repair tests were conducted to determine if our capillary gels could reform their structure into a one-piece material after being cut into two equal pieces. We wanted to ensure that the gels were self-repairing due to the magnetic interactions of the incorporated MNPs while they were stimulated by the application of an external magnetic field ( $H= 50$  mT) and not simply self-adhering. That is, we wanted to see how the sample healed through adhesion as compared to through an external magnetic field-assisted repair. In order to do this, we applied an equivalent force exerted by the applied field using glass slides. The force exerted on the capillary gels by the applied magnetic field was measured and the required weight of the glass slides was calculated in

order to use a comparable weight during the adhesion test. The force data and calculations were as follows:

**Table 3.1** Force calculations for sample self-repair experiment

Force of sample when no magnet was applied	1.14 N
Force of set up when the magnetic field was applied	1.21 N
Force of magnet when applied	0.07 N

Hence, by using the equation for force,  $F = m * a$  we input the known values and rearranged the equation to solve for the mass  $m = 0.00714 \text{ kg} = 7.14 \text{ g}$ . This meant that the glass slides we applied to the cut gel during the self-repair experiments would need to weigh 7.14 g. The samples were disrupted by shaking the Petri dish containing the sample.

### ***3.2.9 Magnetometry specifications***

The magnetization of the magnetic capillary gels was characterized by using the Quantum Design MPMS 3 SQUID/VSM magnetometer. The device was calibrated using a reference sample made of Pd. The device works by applying a DC field on a sample inside of the chamber. The sample interacts with the applied field by magnetizing in a certain way. The magnetization of the sample interacts with the Josephson junction, creating a voltage in the coil. This voltage is proportional to the total magnetization. All samples were run at 25 °C.

### ***3.2.10 Temperature rheology study specifications***

Rheological analysis of the capillary gels that were stored at different temperature conditions was performed using a DHR-2, TA Instruments (New Castle, DE) rheometer with serrated parallel plate geometry (diameter = 40 mm with 0.5 mm gap size). Gels studied were MRCG type 1 and 2 gels at 10 wt%, 20 wt% and 30 wt% OA that were stored either in the oven at 60°C, in the fridge at 4 °C or in the freezer at -15 °C. Angular frequency sweeps were conducted at 1% strain for 0.09–100 rad s<sup>-1</sup>. The amplitude oscillatory measurements were conducted within the linear viscoelastic regime of the gels. All tests were run at a constant temperature of 25 °C.

## **3.3 Results and Discussion**

To determine the feasibility of making new capillary-based gels with tunable properties, we began by making control gels without magnetic particles present in the PDMS microbeads or within the oleic acid capillary bridges. To do so, the oleic acid and PDMS beads were mixed at high shear rate of 650 RPM and were imaged using brightfield microscopy to confirm the network formation (Figure 3.3). PDMS microbeads with no MNPs were synthesized as described above. As is the case with the magnetic beads discussed in Chapter 2 of this dissertation, the size of the microbeads can be tuned by varying the RPM at which the beads are emulsified. In the microscopy images in Figure 3.1, it can be observed that an increase in shear rate leads to a decrease in particle size as well as a noticeable decrease in polydispersity. For this Chapter and in most of this dissertation, we determined that we wanted to study beads that were approximately 10 μm. For this reason, we kept the RPM ≈ 250 throughout our bead syntheses.

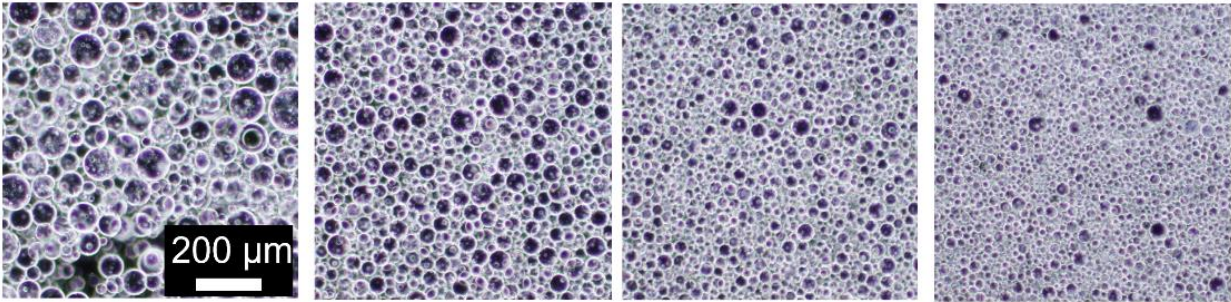


**Figure 3.1** Bright field microscopy images of PDMS beads without internalized MNPs synthesized at increasing RPM varying from 500 RPM to 3000 RPM (left to right).

For the control gel, we simply added oleic acid to the non-magnetic PDMS bead suspension to get a predetermined final gel weight of 5 g. Once the gel structure was confirmed, the actual gels of interest with magnetic nanoparticles in either the PDMS beads or in the oleic acid capillary bridges were synthesized. In order to synthesize the magneto-capillary gels with nanoparticles in the capillary bridges, MRCG1, we added the magnetic oleic acid described in the methods section in the desired ratio to get a final gel weight of 5 g. Lastly, for the capillary gels with the randomly distributed MNPs embedded in the PDMS, MRCG2, we added regular oleic acid in a predetermined ratio to be able to get the desired final concentration of bridging material and a final gel weight of 5 g. All gel types were synthesized and imaged. The magnetic PDMS beads can be observed in the microscopy images in Figure 3.2.

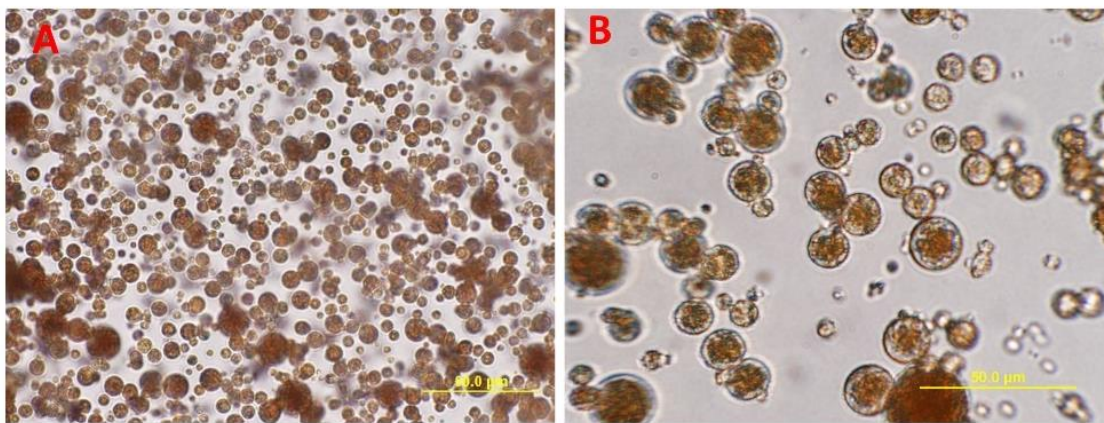


**Figure 3.2** Brightfield microscopy images of composite PDMS beads containing randomly distributed  $\text{Fe}_2\text{O}_3$  MNPs.

The morphology of all three capillary gel types was observed again using both brightfield and fluorescence microscopy with the oleic acid dyed with Coumarin 6 (C6), a hydrophobic fluorescent dye that does not dissolve in the water where the PDMS beads were suspended (Figure 3.3).

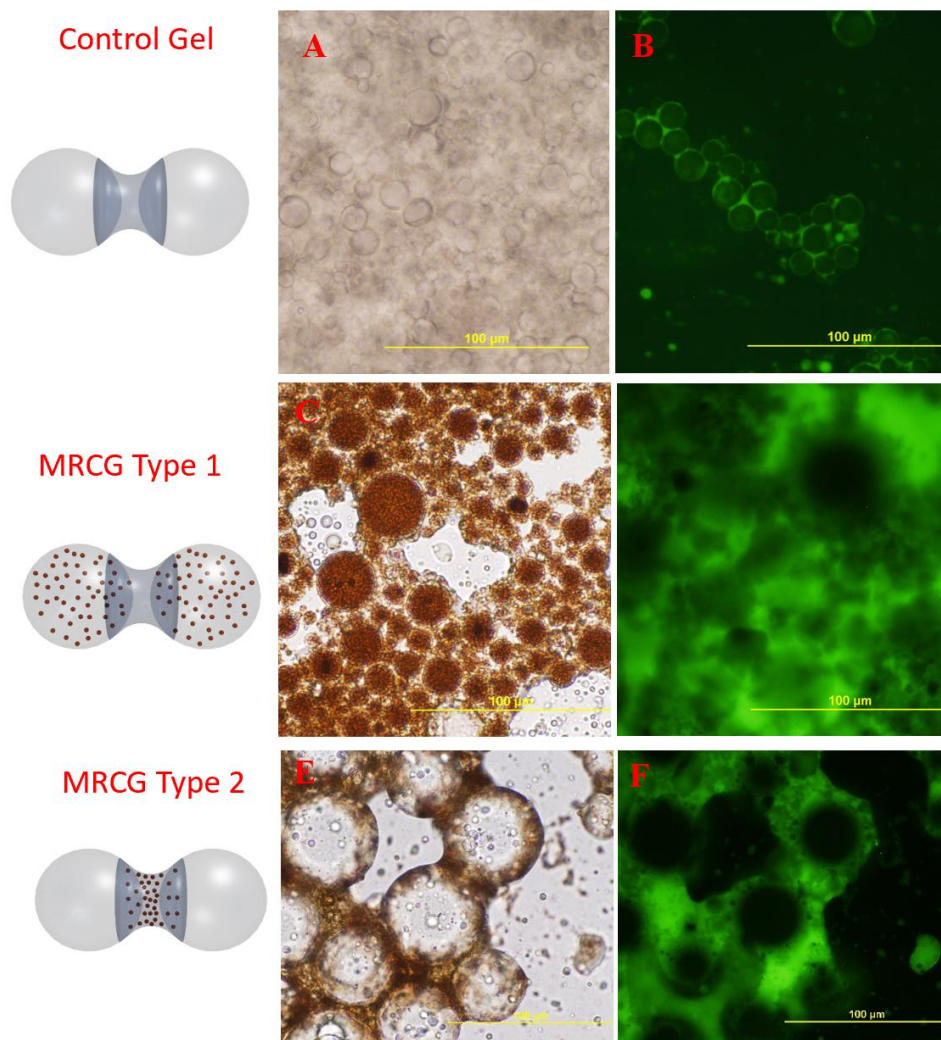


**Figure 3.3** Summary of the magnetocapillary gels synthesized, which differed by the location of the magnetic iron oxide nanoparticles (MNPs) as well as the control capillary gel. The Magnetically Responsive Capillary Gel (MRCG) type 1 was the gel type with MNPs in the PDMS beads, MRCG type 2 was the gel type with MNPs in the oleic acid capillary bridges. (a) Bright field image of control gel, (b) Fluorescence microscopy image of control gel, (c) Bright field image of MRCG type 1, (d) Fluorescence microscopy image of MRCG type 1, (e) Bright field image of MRCG type 2, (f) Fluorescence microscopy image of MRCG type 2.

The bridging of PDMS particles with oleic acid can be observed in the spaces between the PDMS beads in the gels. In the case with the gels containing the MNPs in the OA, the MNPs were well dispersed in the fatty acid capillary bridges. Container tube inversion tests were performed to confirm that the samples demonstrated physical gel-like behavior <sup>16</sup> From Figure 3.4, it can be noted that all gels passed the vial inversion test. Figure 3.4a-d show the gels with MNPS within the OA capillary bridges and denote increasing concentrations of capillary bridge material from 10 wt% (3.4a) to 40 wt% (3.4d). Figure 3.4e-h show the gels with randomly distributed MNPs in the PDMS beads, with varying amounts of oleic acid ranging from 10 wt % (3.4e) to 40 wt% (3.4d). All gels were considered to have passed the vial inversion test because the samples stayed in one piece as an intact structure even when the vials were turned upside down.

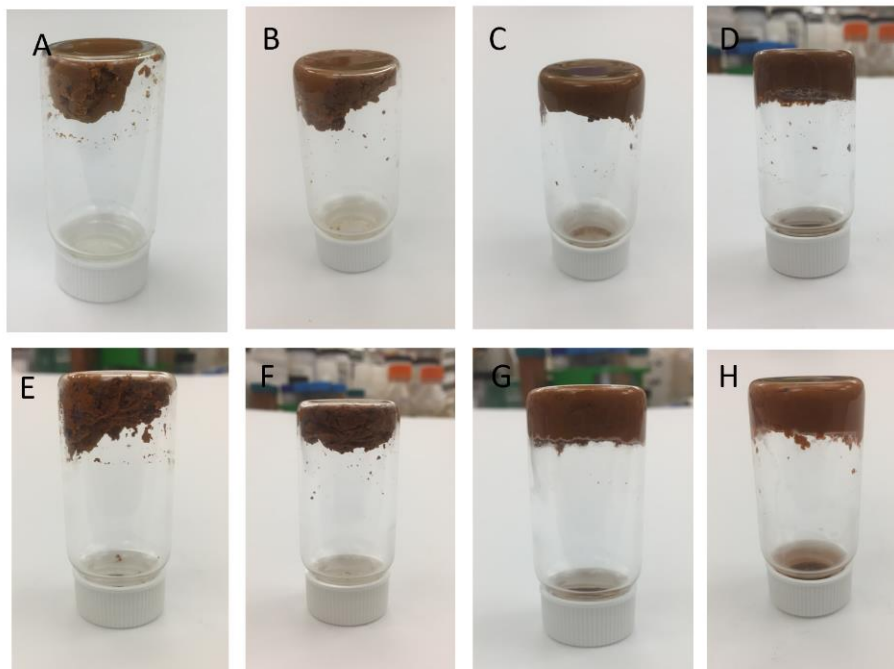


**Figure 3.4** Gels with randomly dispersed MNPs in (a-d) the OA and (e-h) the PDMS beads with 10 wt%-40 wt% OA (left to right). All samples passed the gel inversion test by staying in one piece even when sample was turned upside down.

The capillary gels' magnetic response was also confirmed by placing a permanent NdFeB magnet close to a sample vial. The sample consisted of several pieces of a gel composed of 20 wt% OA with magnetic PDMS beads in water medium. The gel was cut into several pieces to see if all pieces would respond to the magnetic field. The sample was easily manipulated with the magnet and responded to the field by a prompt reconfiguration in the direction of the field lines. Since the magnet and thus the field was applied vertically, the gel moved down, in the direction of the applied field, in as little as 3 seconds (Figure 3.5).

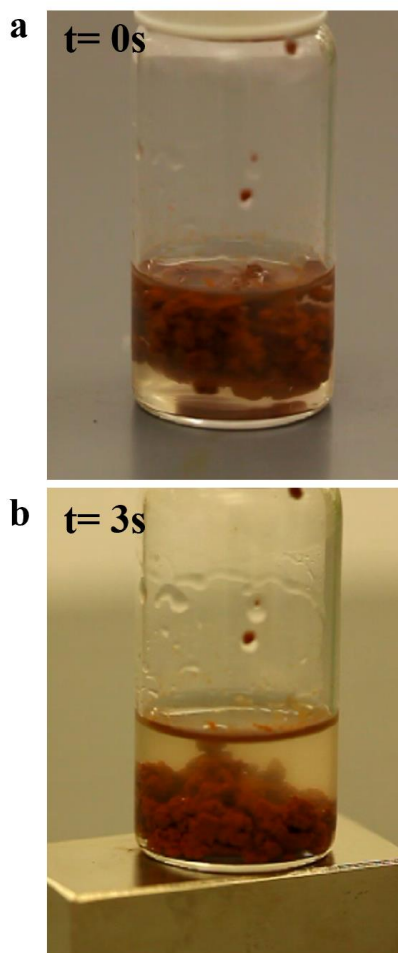


**Figure 3.5:** An example of the magnetic response of the gel samples in the presence of a permanent magnet with (a) the sample being initially cut into several pieces and (b) then merged back into one piece in response to the proximity of the magnet in as little as 3 seconds.

Rheological measurements demonstrated that the viscoelasticity of the prepared gels can be tuned with the fraction of capillary bridging material.<sup>16-18</sup> Solid-like gels are characterized by the presence of a storage modulus,  $G'(\omega)$  that has a plateau, or relatively flat region with a loss modulus,  $G''(\omega)$  that is considerably smaller than the storage modulus within this region. In this case  $\omega$  is the angular frequency that serves as a variable in a frequency sweep rheology experiment. These types of gel-like materials also do not exhibit an equilibrium modulus, or a crossover point between the storage and loss moduli. The elastic behavior of a gel can be evaluated on the basis of the difference between the storage and loss moduli. Furthermore, the cohesion of beads bound by capillary bridges is noticeably increased up to a certain liquid content, much like the formation of a sandcastle.<sup>19</sup> However, past this liquid content, higher liquid volume fractions result in softening of the samples and a decrease in their stability.<sup>20</sup> This phenomenon of liquefaction is comparable in nature to a landslide.

This series of phenomena was observed in our samples. As can be noted in Figure 3.6, all gel types of all concentrations demonstrated solid gel-like behavior with  $G' \gg G''$  in the entire range of frequency sweep, suggesting that these gels are formed with strong tolerance to external forces. That is, regardless of whether the gels had internalized magnetic material or not, where the magnetic material was located within the sample, all samples were gel-like. This can be attributed to the capillary bridges that form between the PDMS beads regardless of the magnetic material.

It was also observed that the values of  $G'$  and  $G''$  decreased with increasing amount of OA, denoting a less elastic gel. When looking at the data for the same amount of bridging material (each graph in Figure 3.6), it can be observed that the gels with the MNPs in the OA always displayed the larger moduli, followed by the samples with MNPs randomly dispersed in the PDMS beads, and lastly with the control samples with no MNPs exhibiting the lowest moduli. This trend

was present among gels of all three weight % of OA that were studied (20 wt%, 30 wt%, 40 wt%). This indicates that the strongest gels are those with the MNPs dispersed in the OA. We hypothesize that this is due to the increased stiffness of the sample that is obtained by having the MNPs coated by the OA. Dispersed magnetic material or MNPs can be considered a gel-like sample in itself due to the strengthening and stiffening effect that the nanoparticles have on the capillary bridges because they are coated by the fatty acid.<sup>21,22</sup> This is also similarity with the system studied by Bharti et al., where the magnetic nanoparticles were dispersed or coated in a fatty acid.<sup>21,22</sup>

Lastly, we can note from the rheology data that the difference between the storage and loss moduli of the control gels and the gels with MNPs embedded in the PDMS beads remain relatively constant across all weight % of OA. However, this does not appear to be the case for the gels with MNPs in OA. These gels presented a decreasing difference between the storage and loss moduli with increasing amount of OA. That is, as the amount of capillary bridge of OA increases from 20 wt% to 40 wt% of gel compositions, the difference between  $G'$  and  $G''$  in each frequency sweep for this gel type decreases. This result leads us to believe that the gels are losing their stability due to the increase in the volume of the liquid capillary bridges. This implies that at 40 wt% OA, the PDMS beads are beginning to get oversaturated by the OA. Furthermore, it is likely that as the amount of liquid in the bridges increases, it enables the local reorganization of the nanoparticles and assists in forming true equilibrium configurations that exhibit stronger interactions than the ones between nanoparticles constrained inside the PDMS beads. Lastly, the increase in liquid content of the gels makes this sample soft, with a larger yield comparable to a landslide, as the gel is weakened by the oversaturation of the beads with the magnetic OA.

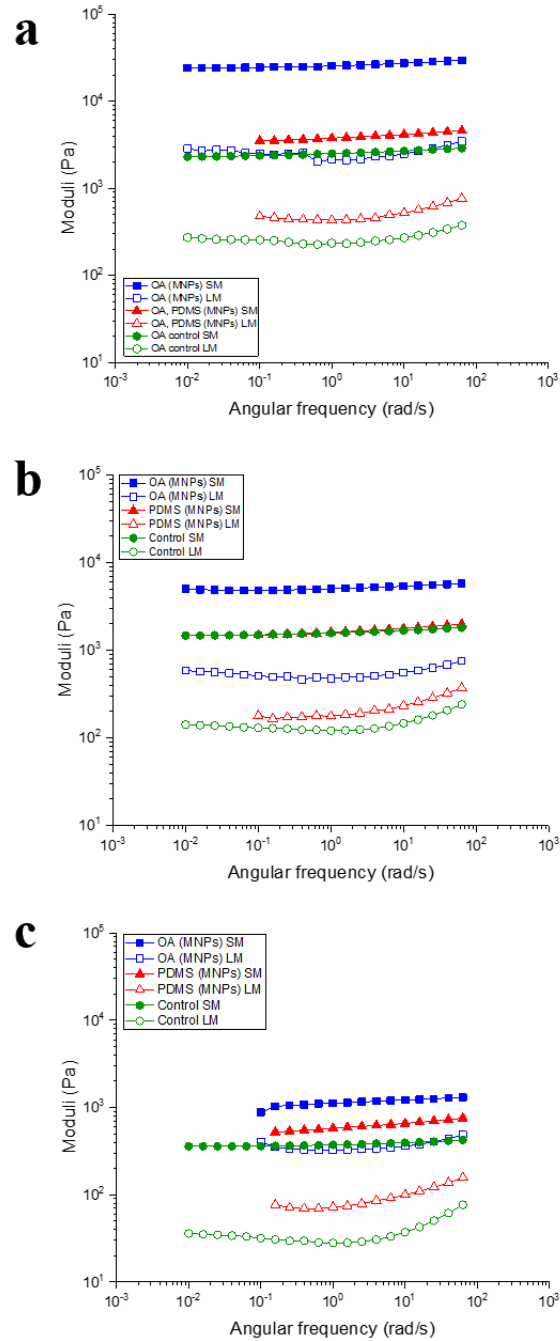


**Figure 3.6** Angular frequency dependence of elastic (storage) modulus (filled symbols) and viscous (loss) modulus (open symbols) in the linear viscoelastic regime of our control samples (green), samples with randomly dispersed magnetic nanoparticles in the PDMS beads (red) and samples with magnetic nanoparticles in the oleic acid (blue) at varying weight percent of oleic acid (a) 20 wt% (b) 30 wt% and (c) 40 wt%.

Figure 3.7 below summarizes the results obtained from Figure 3.6. Again, as the amount of oleic acid present in the gels increased, the overall gel strength decreased regardless of the gel type. We can more clearly observe through this figure that the  $G'$  of the control gel and the gel with MNPs in the beads are very similar and that the  $G'$  of the gel with the MNPs in the liquid bridges is considerably higher.

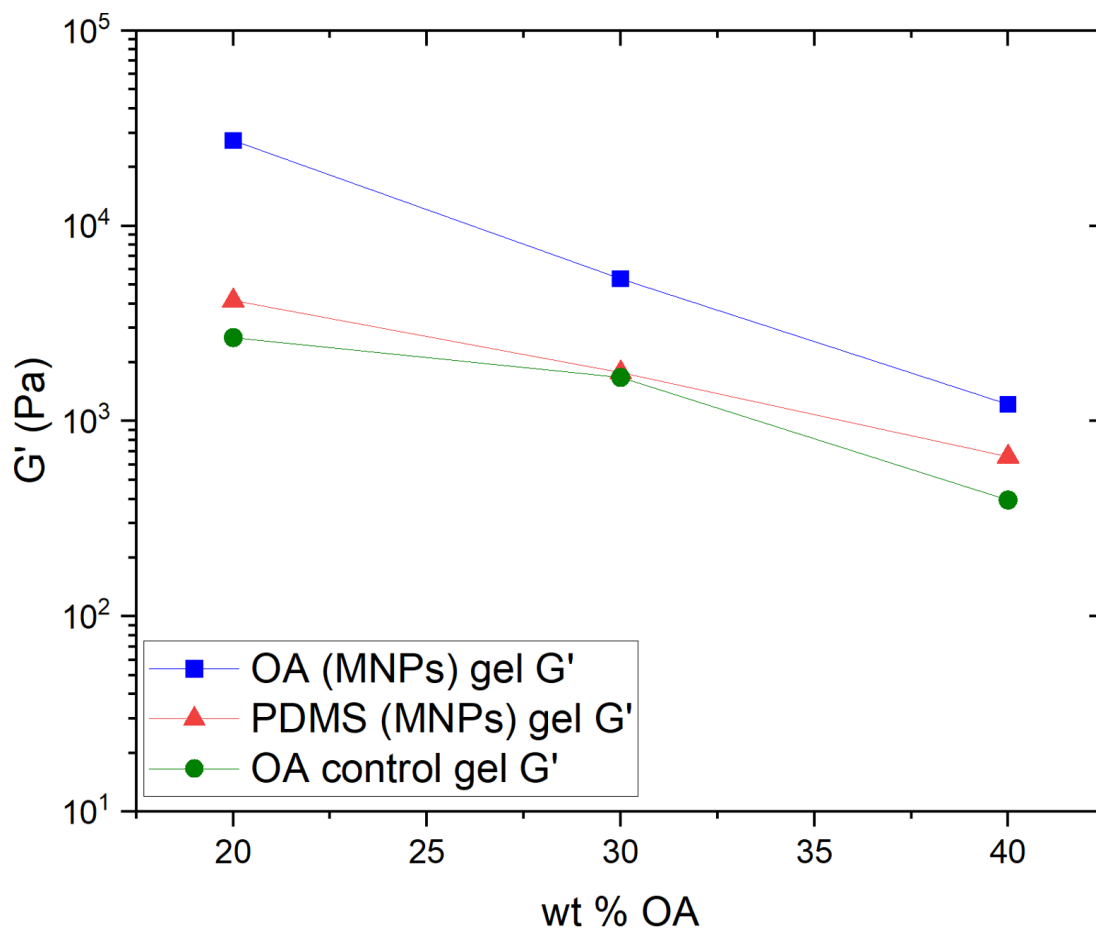


**Figure 3.7** Relationship between the amount of oleic acid present in the gels and the elastic (storage,  $G'$ ) modulus in the linear viscoelastic regime (when frequency= 1 rad sec<sup>-1</sup>) of our control samples (green), samples with randomly dispersed magnetic nanoparticles in the PDMS beads (red) and samples with magnetic nanoparticles in the oleic acid (blue).

It is understandable that these gels have moduli orders of magnitude larger than the more liquid-like magnetically induced gels from Chapter 2 (with and without MNPs) due to the added OA, which is immiscible with the PDMS beads and the continuous phase, water. The OA forms small capillary bridges, resulting in strong cohesive forces between the particles and giving rise to samples of excellent strength and stability.

### ***3.3.1 Magnetic characterization of the magneto-capillary gels***

The magnetic forces induced in the system will dominate other interparticle forces including van der Waals, electrostatic and steric forces, hence characterizing these forces within the gels is essential.<sup>23,24</sup> For this reason, the magnetic properties of the magneto-capillary gels were studied with a superconducting quantum interference device (SQUID) magnetometer. The magnetization curves show some residual magnetic moment in all gel samples (Figure 3.8). Here we assumed that the PDMS, OA, and water did not interact with magnetic field and therefore all had a magnetic susceptibility of  $\chi=0$ . Thus, any hysteresis present in the sample and shown in the magnetometry graphs should be attributed solely to the interaction of the MNPs within each magneto-capillary gel and not any of their other components. As a reminder, in the MRCG Type 1, the nanoparticles are dispersed in the liquid phase in the capillary bridges between the elastomer particles. These gels have a magnetic responsivity that results from magnetic and magnetophoretic forces applied to the nanoparticles in the liquid bridges. These MNPs could be organized into chains by alignment inside the liquid between the beads. Alternatively, the MRCG Type 2 consists of magnetically responsive PDMS beads with embedded randomly distributed MNPs. MRCG gel Type 2 does not allow macroscopic directional polarization of the MNPs that are embedded because they are randomly distributed and thus not aligned. Hence, the magnetic force operates on the MNPs

embedded in the microspheres in the second gel type whereas it operates on the liquid bridges that can re-arrange following their dynamics in the first gel type.

Magnetometry confirmed that all these hybrid samples were weakly ferromagnetic at room temperature. The curves plotted in Figure 3.8 show that the magnetic moment normalized with the mass of the MNPs present in the sample as a function of magnetic field. Magnetic materials can be classified as either soft, intermediate, or hard. Soft materials have low coercivities ( $H_c$ ), usually less than 1 Oe, whereas hard materials have high coercivities, usually greater than 10 kOe. A hard magnet has remanence ( $M_r$ ) values that are about 50% or more of saturation magnetization ( $M_s$ ) in randomly oriented samples or that have a squareness ratio ( $M_r/M_s$ ) of approximately 0.5 or greater.<sup>25</sup> All gels samples can be classified as intermediate magnetic materials. The squareness ratios for all gels studies is reported in Table 3.2 below.

**Table 3.2** Squareness ratio of magneto-capillary gels

	<b>20 wt% OA</b>	<b>30 wt% OA</b>	<b>40 wt% OA</b>
<b>MRCG Type 1: OA (MNPs)</b>	0.186	0.189	0.182
<b>MRCG Type 2: PDMS (MNPs)</b>	0.170	0.148	0.151

Furthermore, all gel samples had an  $H_c$  of approximately 0.125. These values of  $H_c$  and squareness ratio are favorable for applications that would require tuning of the magnetization such as magnetization and demagnetization studies since materials with these range of values can be easily magnetized and demagnetized.

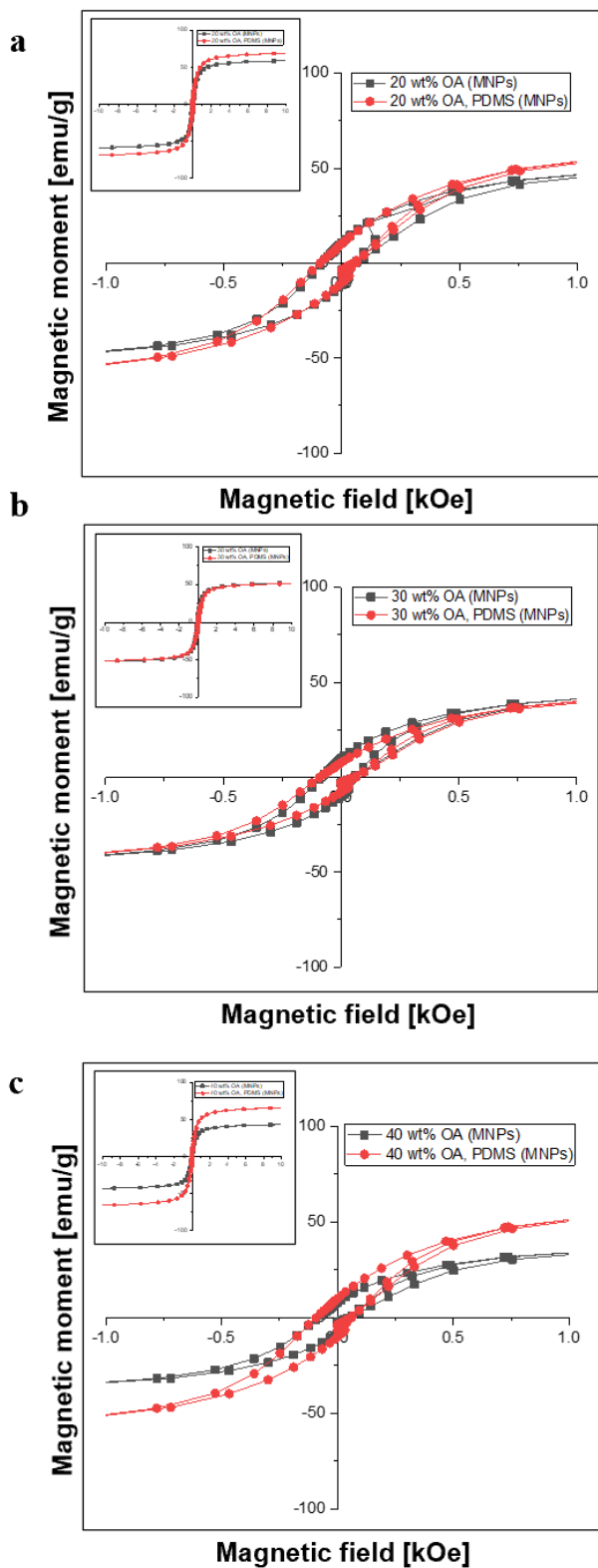


**Figure 3.8** Overlay of magnetization graphs of (a) 20 wt% OA gels, (b) 30 wt% OA gels, and (c) 40 wt% OA gels. Insets show an expanded graph in the region from -10 to 12 kOe.

It can be noted that the MRCGs of type 1 weren't noticeably different in terms of the squareness ratio and that the MRCGs of type 2 varied slightly in ratio values but without overall trend with regards to the increasing amount of oleic acid. Further magnetometry studies would need to be conducted in order to better understand if there are any trends in the different types of gels, possibly by magnetizing or demagnetizing the samples before measurements are taken.

### ***3.3.2 Magnetically assisted self-repairing***

The phenomenon of magnetic gel self-repairing was also studied. We were able to study this type of self-repair both in air and in a water medium. For the experiment in air, a square-shaped piece of gel (composed of 20 wt% MNPs in the PDMS beads) was placed on top of a microscope slide and was sliced in half using a cover glass. We ensured that the two pieces of cut gel were fully separated. We next stacked the pieces back where they had been sliced and applied a vertical magnetic field of  $H = 50$  mT. Upon introducing this NdFeB permanent magnet, the gel regained its one-piece cohesivity. We were able to pick up and handle the repaired gel, thus demonstrating successful self-repair. Since there was no other interaction occurring in the system or any other stimuli being applied besides the magnetic field, we conclude that the gel regained its original structure due to the magnetic attraction of the MNP-laced PDMS within the capillary gel. When the PDMS beads across the gap became attracted due to the externally applied field, the capillary bridges were able to reform between the magnetic beads, effectively repairing them and reforming the one-piece structure. This experiment is highlighted in Figure 3.9.

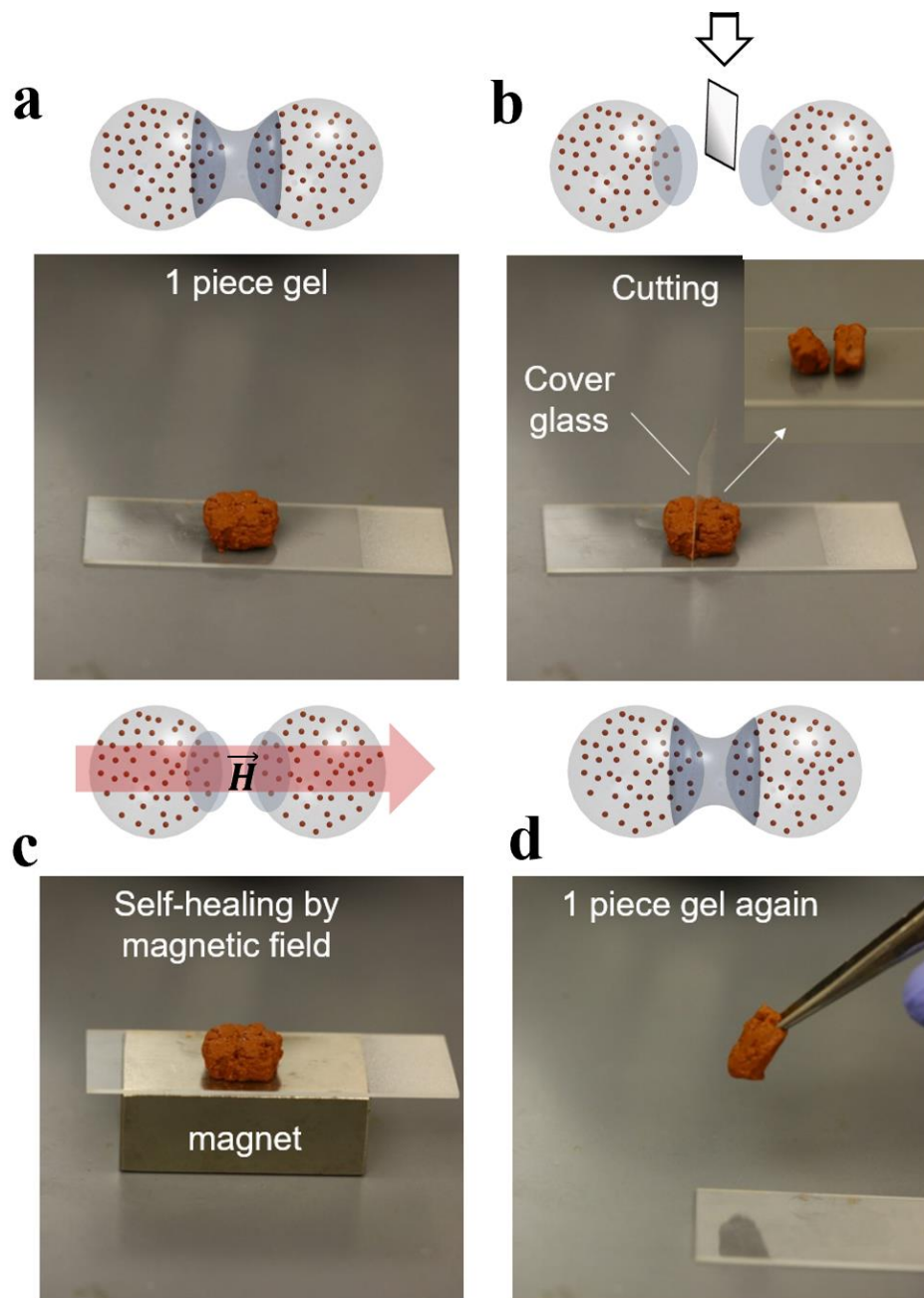


**Figure 3.9** Illustration of a magnetic gel self-repair driven by a permanent magnet, which enabled the capillary gel to regain its one-piece integrity.

In order to ensure that the achieved repair was a result of actual magnetic reconstitution and not simply due to self-adhesion of the gel on contact, another set of experiments was conducted

in water medium. The gel structure repair was done either by introducing a rectangular permanent magnet ( $H= 50$  mT) or a glass slide of a weight that exerted the same force on the gel as the evaluated force exerted on the gel by the permanent magnet. We hypothesized that a small piece of gel in water could be systematically aligned and self-repaired under the action of an externally applied magnetic field. Self-adhesion could potentially also occur by adding weight to the sample when the gel pieces come into contact in water medium in order to reduce the overall interfacial free energy. These tests were conducted with all gel type samples. That is, we looked at both types of MRCGs, with MNPs in the OA or in the PDMS beads. We also studied most of the concentrations of bridging material that were also studied using rheology: 30 wt% or 40 wt% OA. We conducted experiments with at least two different batches of each gel type of the same composition for a total of 72 samples to ensure reproducibility. Each gel type had 9 samples that were tested.

We then determined self-repair effectiveness. A key requirement for a sample to be completely self-repaired was that it had to not only regain its one-piece structure once the required force was applied to it. It also had to remain in one-piece even if the sample was disturbed. This would prove that the self-repair was permanent and not just the sample sticking at contact points due to the gel's stickiness. Hence, if the consolidated gel sample broke apart after it was disturbed, it would be considered ineffective at self-repairing and not counted towards the effectiveness percent. Self-repair was observed with varying effectiveness as we will discuss below. As an example, in the case of magnetically induced self-repair for the gels with MNPs within the OA at 30 wt% OA, the effectiveness was calculated as 22.2 wt%. This value means that of the 9 total gels studied, 2 of the gels not only reformed the capillary bridges to give a one-piece structure but also were able to remain in one piece after being disturbed (Table 3.3).

The level of self-repair seemed to depend strongly on the amount of OA in the capillary bridges of the gel. In general, the 40 wt% OA gels appeared to have better self-repair effectiveness than the gels with 30 wt% OA. This could potentially be attributed to the fact that these gels have more liquid bridging material that can more readily move around to reform the capillary bridges. Moreover, the self-repair did not seem to depend on the location of the MNPs within the gels. For both types of repairs, the gels with 30 wt% OA had slightly higher sample repair effectiveness for the gels with MNPs in the PDMS beads than the gels with the MNPS in the OA. The 40 wt% gels, however, displayed a different trend, with the gels with MNPs in the OA displaying higher sample repair than the gels with MNPs in the PDMS beads. The differences between the self-repaired samples of MRCG type 1 and 2 were thus inconclusive. We believe this is likely because the same amount of magnetic material is present in both types of gels, thus the magnetic response of the gels to the applied magnetic field should be very similar.

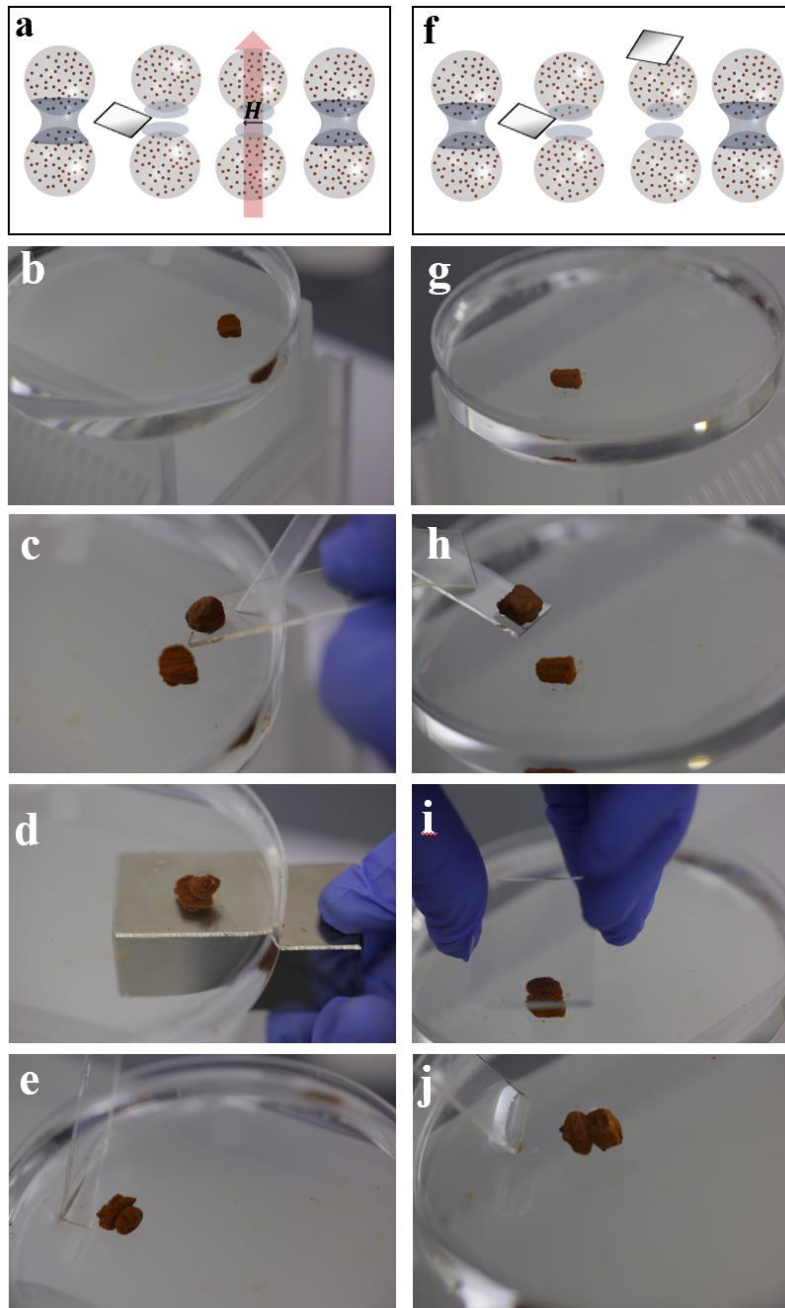


**Figure 3.10** Illustration of self-repair experiments conducted either with an external magnetic field or with a force exerted on the sample and with samples in water medium. (a) Schematic of magnetically assisted self-repair and (b-e) Images of the steps in corresponding experiment. (f) Schematic of how the self-repair of a gel is conducted using the same force applied through a glass slide and (g-j) Images of the steps in corresponding experiment.

Overall, although there is not a significant difference in the number of times the gels self-repaired by the applied weight versus by the applied magnetic field, the samples that were self-repaired by a magnet seemed to retain their one-piece structure better after disturbing the gel. This means that the self-repair effectiveness of the gels with the applied field was higher than that of the gels repaired by applying a weight of comparable force (Table 3.3). This is likely because the two sliced pieces of gel, once in close proximity due to the magnetic interactions with the applied field, began healing by reformation of the capillary bridges, thus making the gel strong enough to be picked up or swirled without breaking apart. We believe that the magnetic field-induced self-repair is longer lasting and thorough. This is evidenced in the higher percent of effectiveness for the gels with this type of repair. We think this is the case because there are a greater number of points of contact in the gap between the cut gels, allowing for the capillary bridges to reform when nearby beads are pulled together by magnetic interactions. Thus, the external magnetic field helps accelerate the capillary aggregation through the magnetic attraction between the particles and their directional alignment. This leads to a strong binding between the PDMS beads which is characteristic of capillary bridging.<sup>26,27</sup>

On the other hand, the case with weight added above the pre-cut sample is more physically similar to self-adhesion on contact. This is because the force exerted on top is pushing one piece of gel into contact with the other and forcing immediate repair. In summary, we presume the number of points of contact present in the gels as well as the hydrophobic interaction of the gel in the water medium were responsible for the general self-repair. Further studies with more batches of each gel type could help determine better the effectiveness of self-repairing of both systems as discussed above. It's also important to ensure that the disruption of each repaired gel is uniformly applied.

**Table 3.3** Summary of the gel repair effectiveness by adhesion or the application of a magnetic field

	<b>Magnetic-field induced sample repair</b>		<b>Adhesion sample repair</b>	
	<b>30 wt% OA</b>	<b>40 wt% OA</b>	<b>30 wt% OA</b>	<b>40 wt% OA</b>
<b>MNPs in OA</b>	22.2%	88.8%	11.1%	77.7%
<b>MNPs in PDMS</b>	33.3%	66.7%	33.3%	55.6%

### ***3.3.3 Rheology self-repair study***

We wanted to prove the efficiency of gels self-repairing in a quantitative way. This was done by rheological characterization of the gel strength before and after deformation. A frequency sweep can reveal physical properties such as if a sample is more gel-like or liquid-like. By measuring a frequency sweep before and after the sample is deformed, you are able to determine if (1) the sample is still a gel and (2) the potential difference in moduli that could have been caused by the sample's deformation. One way to deform a sample is to run a strain sweep experiment on it. This type of experiment is commonly done to determine the linear viscoelastic regime of a material before running a frequency sweep to ensure that the properties of the material are within the relevant frequency range, when  $G'$  and  $G''$  are parallel and  $G'$  is greater than  $G''$ . These types of experiments show when the sample is deformed at the point in which  $G'$  and  $G''$  intersect. A time sweep is a different type of rheological experiment looking at the  $G'$  of the sample that can tell you how long it takes the sample to stabilize or equilibrate. When the time sweep has a flat  $G'$ , the material has stabilized.

We combined all three of these rheology experiments to confirm that our magneto-capillary gels do indeed self-repair. In order to do this, we first ran a frequency sweep to see the relation between  $G'$  and  $G''$ . We then ran a strain sweep to deform the gels, effectively breaking the capillary bridging apart. We then ran a time sweep to confirm that the gel was equilibrated or repaired and to see how long it took to do so. Lastly, we ran a second frequency sweep to see how the moduli of the gel compared to the original moduli. By doing this, we sought to find if the gel repaired and formed capillary bridges to the same extent that it was originally. We studied both types of MRCGs at 10 wt%, 20 wt%, 30 wt% and 40 wt% OA composition. In Figure 3.11, one can observe our results for the gels with the MNPs in the oleic acid. Figure 3.11a presents the results for the 10 wt% OA sample and Figure 3.11d presents the results for the 40 wt% OA sample. As can be noted in the figure, all gels were able to self-repair to the same properties that they had originally. This can be confirmed by looking at both frequency sweep results for all of the gels. All of these almost overlap, indicating that the gel strength is the same before and after the deformation. Furthermore, we confirmed the gel deformation with the strain sweep for all gels can be noted by the yield point or intersection of  $G'$  and  $G''$  in all of the strain sweep graphs. Lastly, all time sweep experiments confirmed that the gels equilibrated after varying amounts of time. These times are marked for each gel by a vertical blue line in the time sweep graph (Figure 3.11, right graphs).

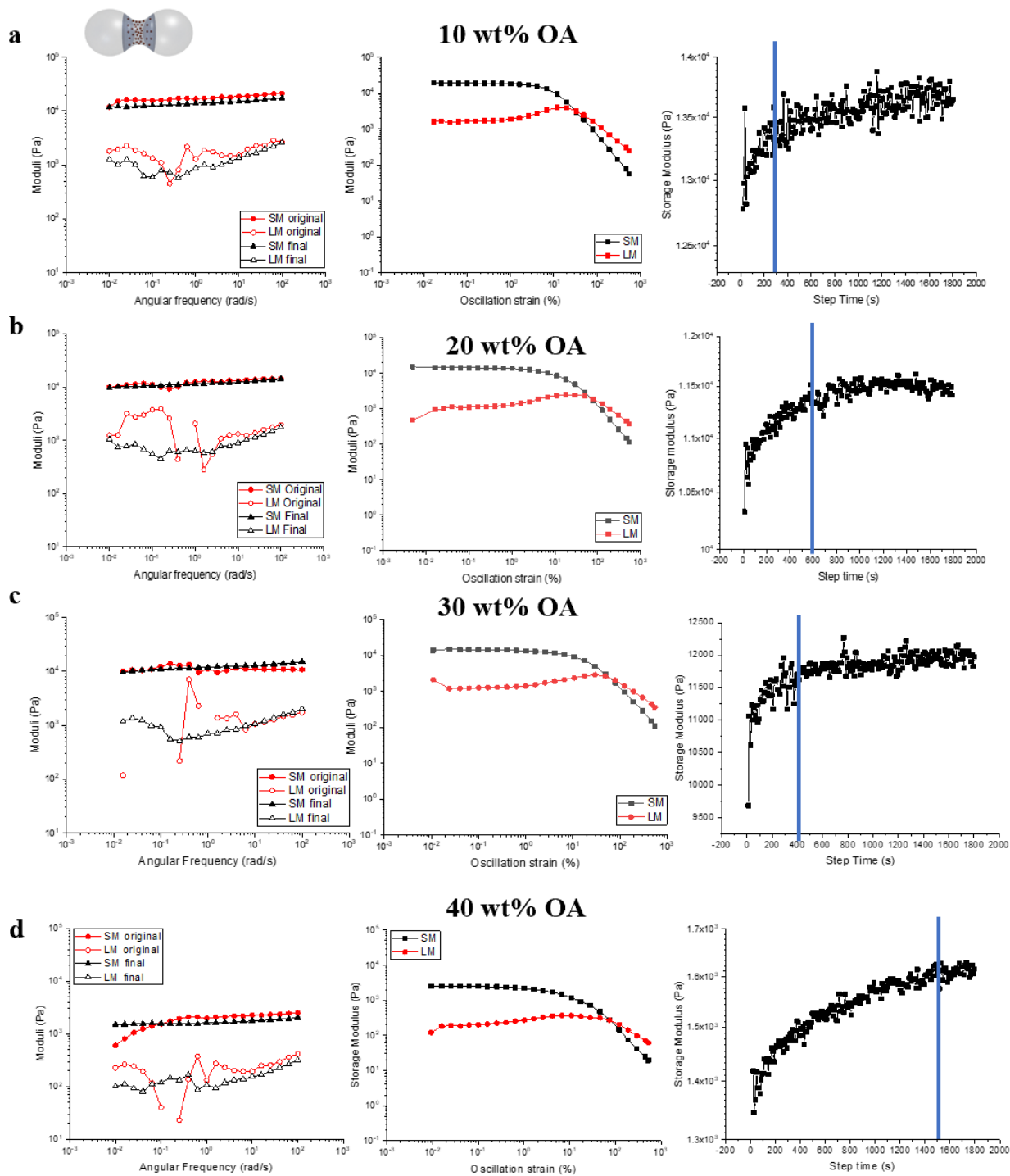


**Figure 3.11** Rheological data for the capillary gels of varying concentrations of OA with MNPs in the OA capillary bridges. These experiments were conducted to confirm gel self-repair. (a) 10 wt% OA, (b) 20 wt% OA, (c) 30 wt% OA, and (d) 40 wt% OA.

We observed similar results for the capillary gels with the MNPs in the PDMS beads (Figure 3.12). All gels repaired to almost the same strength they had originally. All gels were deformed, and all gels equilibrated. It can be observed in both types of gels that the amount of strain required to deform the gels increased as the amount of oleic acid increased. That is, the yield point increased as the amount of oleic acid increased. This could be due to the fact that there is so much oleic acid at 40 wt%, that it is difficult to deform the gel in such a way that the beads are not coated or bridged by the oleic acid. The second gel type also had varying amount of time for its self-repair, as can be observed in the time sweep graphs.

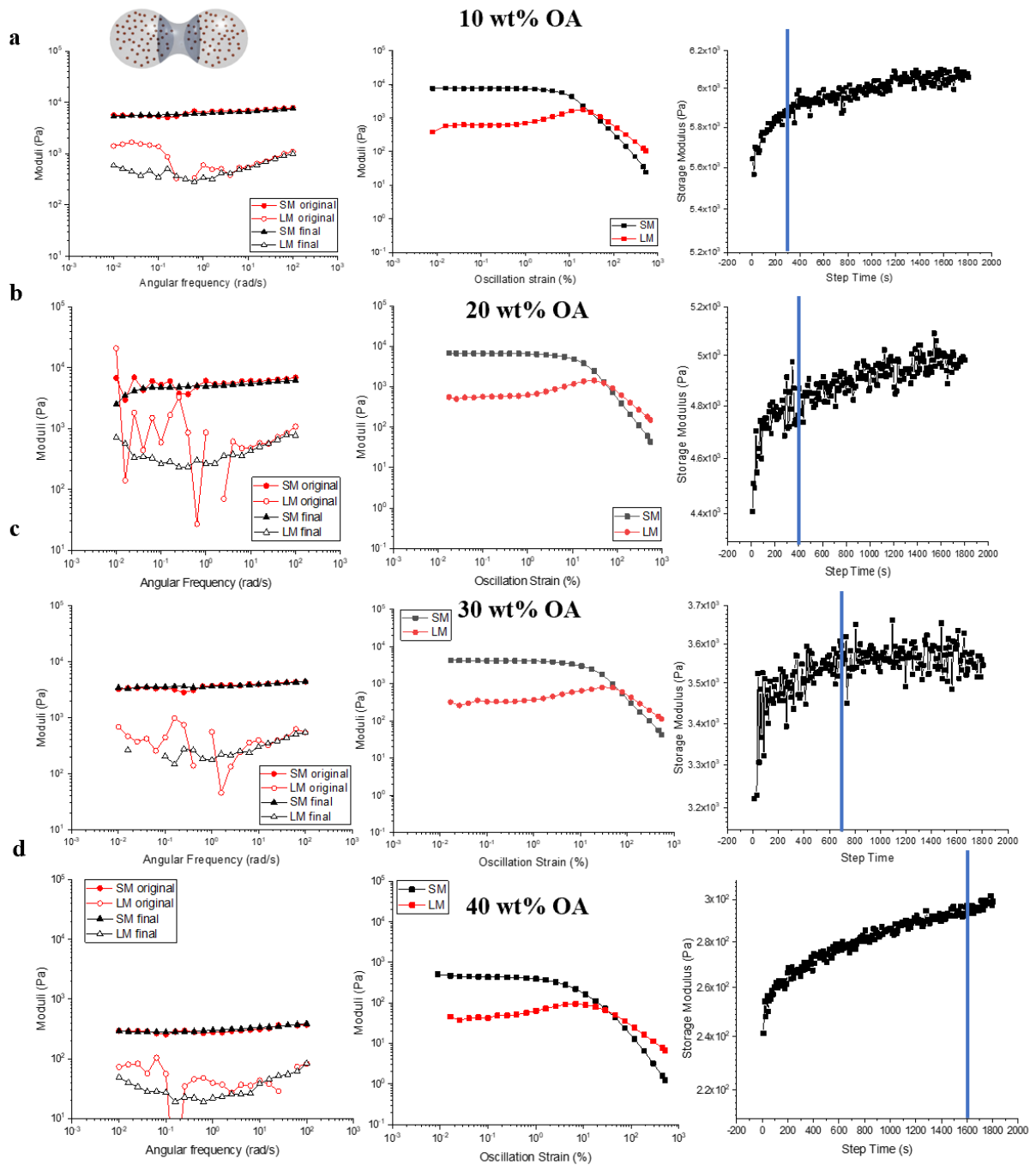


**Figure 3.12** Rheological data gathered for the capillary gels of varying concentrations of OA with 10 wt% MNPs in the PDMS beads. These experiments were conducted to confirm gel self-repair. (a) 10 wt% OA, (b) 20 wt% OA, (c) 30 wt% OA, and (d) 40 wt% OA.

We have summarized all of the time sweep stabilization times for all gels in Table 3.4 below. From this table, we can speculate on a few noticeable trends. First, the self-repair times are similar for both gel types at each concentration. For example, it takes five minutes for both gel types to repair when the gel has 10 wt% OA capillary bridges. Next, in the case of the gel with the magnetic beads, the time for self-repair appear to increase as the concentration of OA present in the gel increases. This was unexpected as we hypothesized that because the gels with higher OA content are weaker gels (discussed earlier in the Chapter), it would be easier to break them apart and reform them. However, based on these data, the gels with higher OA content take longer to break apart and reform. This trend is not readily observed in the case of the gels with the MNPs in the OA. The gels with the least amount of OA stabilize the fastest and the gels with the highest amount of OA also stabilize the slowest as with the other gel type. However, the 20 wt% and 30 wt% gel data do not align with the trend observed with the other gel type. This leads us to believe that having the MNPs in the liquid phase allows the magnetic interactions to play a role in the stability of the gel.

**Table 3.4** Summary of the self-repair time of the magnetic gels during the rheology measurements.

	<b>MNPs in OA</b>	<b>MNPs in PDMS bead</b>
<b>10 wt%</b>	5 minutes	5 minutes
<b>20 wt%</b>	10 minutes	6.5 minutes
<b>30 wt%</b>	6.7 minutes	16.7 minutes
<b>40 wt%</b>	25 minutes	26.7 minutes

### ***3.3.4 Temperature study of the magnetic gels***

We characterized both MRCG gel types using angular frequency sweeps from 0.01-100 rad/s after storing them in different temperature conditions. We studied gels with 10 wt% OA, 20 wt% OA, and 30 wt% OA. Figure 3.13 shows the data for the gel samples with 10 wt% OA after having been stored at 60°C, -4°C, and -15°C. Figure 3.13a is the data for the gels with 10 wt% MNPs in the PDMS beads with 10 wt% OA composition and 3.13b is the data for the gels with PDMS beads with 10 wt% MNPs in the OA at 10 wt% OA composition. The moduli for the oven-stored gels are denoted in blue, the data for the fridge-stored gels are shown in red, and the data for the freezer-stored gels are depicted in green. We observed the same overall trend we observed earlier in this Chapter, with the gels with the MNPs in the OA exhibiting higher moduli than the gels with the MNPs in the PDMS beads. In general, the moduli were very similar for all of storage temperature conditions for the gels with the MNPs in the PDMS. The gels with MNPs in the OA had very similar moduli for the gels stored in the fridge and freezer. We did observe a discrepancy with these gels being stored in the oven. The moduli were slightly lower but still within the same order

of magnitude. This could be because the increase in temperature might be affecting the MNPs that are freely moving in the OA. The increase in temperature could be enabling the MNPS to move around faster and thus disturbing the capillary bridging, resulting in a slightly weaker gel. This suggests that these types of gels with the MNPs in the OA should not be stored at higher temperatures as it can result in a slight decrease in gel strength. Overall, from this data, we conclude that our gels are stable even after being stored at varying temperatures for extended periods of time for the gels with MNPs in the PDMS beads and that the gels with MNPs in the OA should only be stored at room temperature or lower temperatures.

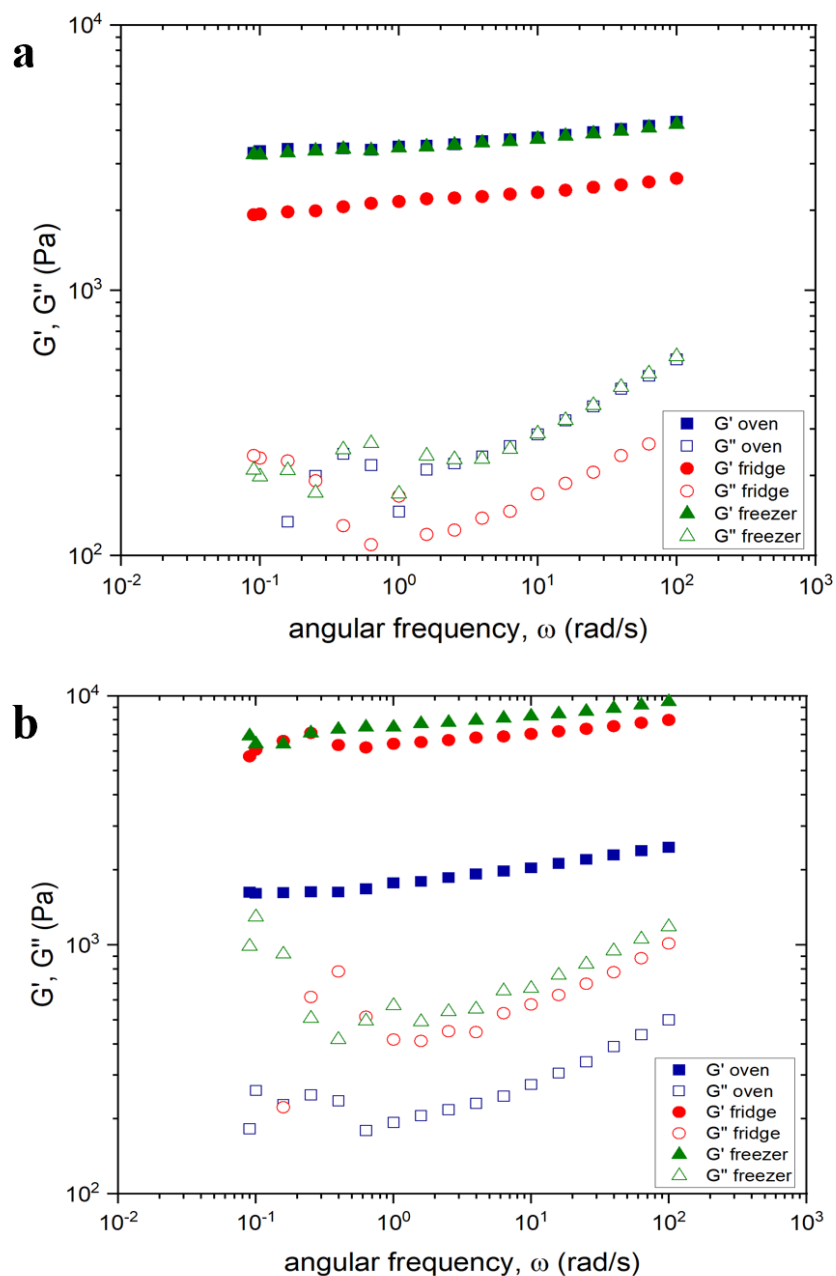


**Figure 3.13** Angular frequency dependence of  $G'$  (filled symbols) and  $G''$  (open symbols) of samples stored in the oven (blue square), stored in the fridge (red circle) and stored in the freezer (green triangles) for gels with (a) 10 wt% MNPs in the PDMS beads with 10 wt% OA composition and (b) PDMS beads with 10 wt% MNPs in the OA at 10 wt% OA composition.

### 3.3.5 Other types of magneto-capillary gels studied

After making magneto-capillary gels with  $\text{Fe}_2\text{O}_3$ , we decided to attempt to make gels with other magnetic material. We tried both Fe particles and NdFeB particles and loaded the PDMS beads with 10 wt% as before. The gels' magnetic response seemed to be high, however, further work would have to be done to determine the self-repairing capabilities of gels with these types of magnetic particles.

We were also able to make magneto-capillary gels with the magnetically aligned PDMS beads discussed in Chapter 2 of this dissertation. We have conducted preliminary rheological characterization of these gels to determine if the gels can be stored at different temperature conditions (data not shown), but further characterization is still needed. The morphology of these gels can be seen in the microscopy image in Figure 3.14 below.

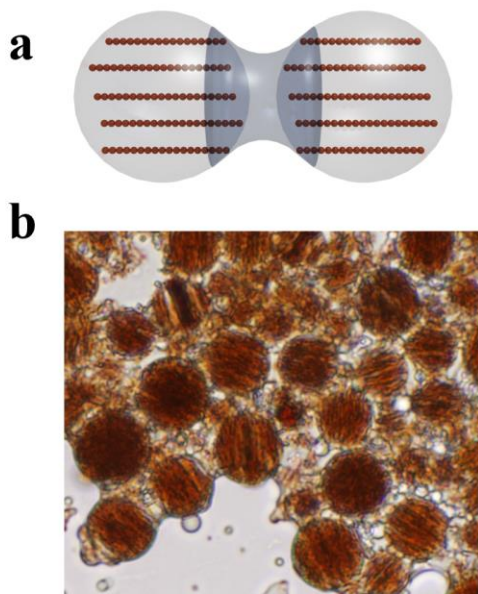


**Figure 3.14** A third type of magneto-capillary gel with PDMS beads with 10 wt% magnetically aligned embedded MNPs. (a) Schematic of this type of gel (b) Microscopy image of this type of gel.

### **3.4 Conclusions**

Going forward, many research approaches could be used to better understand and compare the novel gel systems developed here. Interfacial tension can be tuned by varying the temperature of the gels, with the tension decreasing with increasing temperature in most cases.<sup>28</sup> We are also interested in looking at lower temperatures to freeze the capillary bridges between the PDMS particles. This could mean evoking widely different mechanical and rheological properties depending on the temperature. A fluid-to-gel like transition of the capillary bridges should be present around the freezing temperature of the oleic acid. We would expect the bridges to become liquid upon increasing the temperature beyond the phase transition temperature and upon applying of an external magnetic field. By studying the samples at temperatures below and above the transition of PDMS, we may be able to obtain thermo-magneto responsive gels. Atomic force microscopy could also be used to study the surface structure of the gel.<sup>29</sup> Tuning the temperature of the samples will also potentially have an impact on the magnetic coercivity of the gels, so we would also conduct further magnetometry studies at varying temperatures.

### **3.5 Acknowledgements**

The authors would like to thank Dr. L. Hsiao for the use of the rheometer, Dr. J. Tracy for the magnetometry measurement discussions, and Dr. S. Khan for the valuable rheology discussions.

### 3.6 References

1. Kralchevsky, P.A. & Denkov, N.D. Capillary forces and structuring in layers of colloid particles. *Curr. Opin.* **2001**, *6*, 383-401.
2. Iveson, S.M.; Litster, J.D.; Hapgood, K.; Ennis, B.J. Nucleation, growth and breakage phenomena in agitated wet granulation processes: a review. *Powder Technology* **2001**, *117*, 3–39.
3. Hemmerle, A.; Schroter, M.; Goehring, L. A cohesive granular material with tunable elasticity. *Sci. Rep.* **2016**, *6*, 1-11.
4. Hassan, P.A.; Verma, G.; Ganguly, R. (2012) Soft Materials- Properties and Applications. *Polymer Gel* (1-59).
5. Ahn, S-k.; Kasi, R.M.; Kim, S-C. et al. Stimuli-responsive polymer gels. *Soft Matter*, **2008**, *4*, 1151–1157.
6. Bossler, F. & Koos, E. Structure of Particle Networks in Capillary Suspensions with Wetting and Nonwetting Fluids. *Langmuir* **2016**, *32*, 1489–1501.
7. Koos, E. & Willenbacher, N. Capillary forces in suspension rheology. *Science* **2011**, *331*, 897–900.
8. Liu, F.; Alici, G.; Zhang, B.; Beirne, S.; Li, W. Fabrication and characterization of a magnetic micro-actuator based on deformable Fe-doped PDMS artificial cilium using 3D printing. *Smart Mater. Struct.* **2015**, *24*, 035015, 1-9.
9. Zhang, J.; Huang, Q.; Du, J. Recent advances in magnetic hydrogels. *Polym Int* **2016**, *65*, 1365–1372.
10. Liu, Z.; Wang, H.; Li, B. et al. Biocompatible magnetic cellulose–chitosan hybrid gel microspheres reconstituted from ionic liquids for enzyme immobilization. *J. Mater. Chem.*, **2012**, *22*, 15085.
11. Li, Y.; Huang, G.; Zhang, X. et al. Magnetic Hydrogels and Their Potential Biomedical Applications. *Adv. Funct. Mater.* **2013**, *23*, 660–672.
12. Xu, F.; Wu, C-a M; Rengarajan, V. et al. Three-Dimensional Magnetic Assembly of Microscale Hydrogels. *Adv. Mater.* **2011**, *23*, 4254–4260.

13. Castellanos, N.I.; Bharti, B.; Velev, O.D. Field-Driven Reversible Alignment and Gelation of Magneto-Responsive Soft Anisotropic Microbeads *J. Phys. Chem. B*, **2021**, *125* (28), 7900–7910.
14. Christov, N.C.; Ganchev, D.N.; Vassileva, N.D.; Denkov, K.D.; Kralchevsky, P.A. Capillary mechanisms in membrane emulsification: oil-in-water emulsions stabilized by Tween 20 and milk proteins. *Colloids Surf. A Physicochem Eng. Asp.* **2002**, *209*, 83-104.
15. Roh, S. & Velev, O.D. Nanomaterials Fabrication by Interfacial Templating and Capillary Engineering in Multiphase liquids. *AIChE*. **2017**, *64*, 3558-3564.
16. Niehoff, A.; Manton, A.; McAloney, R.; Huber, A. et al. Elucidation of the structure of poly( $\gamma$ -benzyl-L-glutamate) nanofibers and gel networks in a helicogenic solvent. *Colloid Polym Sci*, **2013**, *291*, 1353–1363.
17. Koos, E.; Johannsmeier, J.; Schwebler, L.; Willenbacher, N. Tuning suspension rheology using capillary forces. *Soft Matter* **2012**, *8*, 6620-6628.
18. Butt, H.-J. Controlling the Flow of Suspensions. *Science* **2011**, *331*, 868–869.
19. Domenech, T. & Velankar, S.S. On the rheology of pendular gels and morphological developments in paste-like ternary systems based on capillary attraction. *Soft Matter* **2015**, *11*, 1500 –1516.
20. Hoffman, S.; Koos, E.; Willenbacher, N. Using capillary bridges to tune stability and flow behavior of food suspensions. *Food Hydrocolloids*, **2014**, *40*, 44-52.
21. Bharti, B.; Fameau, A.-L.; Rubinstein, M.; Velev, O.D. Nanocapillarity-mediated magnetic assembly of nanoparticles into ultraflexible filaments and reconfigurable networks. *Nat. Mater.* **2015**, *14*, 1104-1109.
22. Bharti, B.; Fameau, A.-L.; Velev, O.D. Magnetophoretic assembly of flexible nanoparticle/lipid microfilaments. *Faraday Discuss.* **2015**, *181*, 437-448.
23. Roh, S.; Okello, L.B.; Golbasi, N.; Hankwitz, J.P.; Liu, J. A.-C; Tracy, J.B.; Velev, O.D. 3D-Printed Silicone Soft Architectures with Programmed Magneto-Capillary Reconfiguration. *Adv. Mater. Technol.* **2019**, *4* (1800528), 1-7.
24. Mishra, S.R.; Dickey, M.D.; Velev, O.D.; Tracy, J.B. Selective and directional actuation of elastomer films using chained magnetic nanoparticles. *Nanoscale* **2016**, *8*, 1309-1313.

25. Chinni, F.; Spizzo, F.; Montoncello, F.; Mattarello, V. et al. Magnetic Hysteresis in Nanocomposite Films Consisting of a Ferromagnetic AuCo Alloy and Ultrafine Co Particles. *Materials*, **2017**, *10*, 717, 1-16.
26. Mitarai, N. & Nori, F. Wet granular materials. *Adv. Phys.* **2006**, *55*, 1-45.
27. Alguacil, D.M. & Gauckler, L.J. Analysis of the capillary forces between two small solid spheres binded by a convex liquid. *Adv. Powder Technol.* **2010**, *198*, 211-218.
28. Merland, T.; Waldmann, L.; Guignard, O.; Tatry, M-C. et al. Thermo-induced inversion of water-in-water emulsion stability by bishydrophilic microgels. *J. Colloid and Interface Sci.* **2022**, *608*, 1191–1201
29. Schreiber, S.; Savla, M.; Pelekhov, D.V. et al. Magnetic Force Microscopy of Superparamagnetic Nanoparticles. *Small*, **2008**, *4*, 270-278.

## CHAPTER 4

### Design of 3D printed anchor sites for enhanced characterization of soft magnetic gels

#### 4.1 Introduction

3D printing is an additive manufacturing technology that allows for the fabrication of multi-scale (micro and macro) 3D objects by taking advantage of computer-assisted design and directional additivity to make a vast variety of structures.<sup>1,2</sup> Current 3D printing techniques include continuous direct ink writing and drop-ejection techniques, amongst others.<sup>3-6</sup> Direct ink writing, specifically, is a material fabrication method that uses an ink extrusion nozzle and a computer-controlled translational stage to extrude material with tunable compositions and architectures.<sup>7</sup> This method for 3D printing can be defined as a layer-by-layer fabrication process in which a viscous material, typically a thermoplastic polymer, a photopolymerizable resin,<sup>8</sup> continuous, or even a liquid metal,<sup>9,10</sup> is extruded from a nozzle onto a planar print bed or plate.<sup>1,11</sup> This means that once one layer of material had been printed, the print head moves up, in the z-direction, in order to print the next layer.<sup>11,12</sup> This process is repeated until all the layers of the material are extruded, and the printed material can then be heated to cure or seal the shape of the structure. One of the many advantages of 3D direct ink printing is that it allows for rapid fabrication of complex 3D structures without the need for lithographic masks or expensive tools.<sup>3</sup> Moreover, by using open-source hardware and software tools, 3D printing by extrusion can be quite rapid and cost effective.<sup>12</sup>

One important requirement is that the paste used for extrusion should exhibit a well-defined viscoelastic response such that the filament-shaped paste can flow through the nozzle and then retain its shape once extruded.<sup>3</sup> Another essential requirement is that the paste must be composed primarily composed of the colloid in order to reduce the possibility of shrinkage after the sample

dries or is being cured.<sup>3,13</sup> 3D printing has been used to fabricate numerous structures such as artificial magnetic cilium and artificial tissues.<sup>14,15</sup> The ability to make 3D structures is of large importance in the technological development of photonic, mechanical, electronic, microswimmers,<sup>16</sup> soft robotic devices,<sup>17</sup> as well as drug delivery and tissue engineering,<sup>5,18,19</sup> as well as other biomedical applications.<sup>1,3,4,7,20,21</sup> The design of material with the ability to reversibly respond to external stimuli, in particular, is of essence for numerous applications involving actuators, optics, stimuli responsive surfaces, and sensors.<sup>22,23</sup>

One advantage of these methods is that the 3D printed material can be made stimuli responsive by simply adding a second component such as magnetic material.<sup>20-22,24</sup> Incorporating a magnetic component has an advantage over other stimuli in that the resulting structure can be actuated and controlled remotely.<sup>14</sup> By applying an external field, one is able to obtain a rapid response and alignment in the direction of the applied field. Unfortunately, the majority of the existing magnetic polymeric components are costly, time consuming and involve complex syntheses.<sup>14</sup> Colloidal capillary gels are ideal candidates for 3D printing ink/paste because their viscoelastic properties can be fine-tuned to allow for the extrusion of these soft materials.<sup>7,13,25,26</sup>

Polydimethylsiloxane (PDMS) is biologically compatible and is currently being used in a vast range of biomedical applications such as medical devices,<sup>27</sup> flexible electronics,<sup>10</sup> and microfluidics.<sup>12,28,29</sup> The current standard in the tissue engineering field and in microfluidics is the resin Sylgard 184 PDMS.<sup>12</sup> One disadvantage of PDMS, however, is that its low elastic modulus ( $\sim 1$ MPa) and low viscosity have often proved to be a challenge for 3D printing of complex PDMS-based structures.<sup>12</sup> One way in which some researchers have sought to overcome this disadvantage is by incorporating filler material such as wax microparticles in order to increase the viscosity, however, this often leads to the resulting paste being hardened and therefore too

viscous to extrude. Other researchers have attempted to avoid fillers and have instead opted to use a hydrophilic support structure during the printing process. This results in an increase in cost of materials and experiment/bench time; therefore, it is not ideal. Tuning the concentration of the embedded material allows the optimization of the viscosity such that the system doesn't require support structures.<sup>30</sup>

Magnetic composite material containing dispersed randomly orientated particles behave as single magnetic domain. Fe<sub>2</sub>O<sub>3</sub> nanoparticles of size ~20 nm have superparamagnetic behavior that can be imparted to material in which these types of nanoparticles embedded such as the beads we present in Chapter 2 of this dissertation.<sup>31</sup> Furthermore, iron oxide nanoparticles have been often incorporated into biocompatible materials to make the material magnetically responsive.<sup>32</sup> Moreover, the magnetic response of these nanoparticles can be used to obtain magnetically aligned wire-like structures or chains of particles that demonstrate anisotropic properties. These characteristics can also be transferred to a polymer composite that can be embedded with these types of magnetically aligned particles.<sup>31, 33-35</sup> We have also presented PDMS beads with these types of characteristics in Chapter 2 of this thesis.

Rheological characterization is an important method for understanding colloidal sample strength such as the mechanical properties of suspensions and gels. These measurements can provide information on the viscosity, yield stress, and overall viscoelastic properties of a gel sample. Ensuring that the measurements are accurate is of essence to properly characterize a material. Common errors that can lead to erroneous rheological results are wall slip in liquid-like suspensions and sample sedimentation. Sedimentation can occur depending on the density mismatch of the different components in the measured sample and can be of particular concern in

the case of heavy materials such as metals. Potential sedimentation could increase depending on the length time of a measurement.

In this Chapter, we present a magneto-capillary direct ink-based 3D extrusion printing technique. Through this technique we are able to design and make smart elastomeric anchor sites by 3D printing with homocomposite silicon capillary-based ink that can be physically manipulated in response to an applied field. An earlier version of this technique was originally developed in our group.<sup>25</sup> It is inexpensive and simple/rapid in terms of preparation work and synthesis. This technique used 3D printing paste that is composed of three main materials: water medium (continuous runoff phase), magnetic PDMS beads, and surface-wetting liquid PDMS precursor. In this method, the liquid precursor is able to successfully form capillary bridges between the magnetic beads, resulting in a paste-like gel. This gel can then be extruded to the desired shape/structure and the liquid PDMS precursor capillary bridges can then be cured. This yields soft, elastic 3D structures thereby enabling improved rheology measurements.

## **4.2 Materials and Methods**

***4.2.1 Synthesis of magnetic PDMS prepolymer (10 wt% MNPs)*** See Chapter 2 of this dissertation for a detailed description of this synthesis.

***4.2.2 Synthesis of PDMS beads containing embedded magnetic nanoparticles*** See Chapter 2 of this dissertation for a detailed description of this synthesis.

***4.2.3 Synthesis of PDMS beads containing embedded, aligned magnetic nanoparticles*** See Chapter 2 of this dissertation for a detailed description of this synthesis.

#### ***4.2.4 Permanent NdFeB magnet specifications***

Both types of magnets were rare earth metal, NdFeB magnets. Small square magnets were 1 inch x 1 inch x 2/16 inch. Large rectangle magnet was 2 inches x 3/4 inch x 1 inch.

***4.2.5 Fabrication of precursor magnetic anchor sites (large magnet)*** The rectangular coating-like interaction sites were synthesized by mixing a small amount of the magnetic PDMS (10 wt% MNPs) prepolymer with PDMS crosslinker in a 10:1 ratio and then spreading this precursor on the surface of a Petri dish in the shape of the applied permanent magnet ( $H= 50$  mT) and leaving it to cure at 65 °C overnight.

***4.2.6 Fabrication of precursor magnetic anchors (two small magnets)*** The square coating-like interaction sites were synthesized by mixing a small amount of the magnetic PDMS (10 wt% MNPs) prepolymer with PDMS crosslinker in a 10:1 ratio and then spreading this precursor on the surface of a Petri dish in the shape of the square applied permanent magnet ( $H= 22$  mT) and leaving it to cure at 65 °C overnight.

***4.2.7 Fabrication of precursor magnetic anchor sites (large magnet)*** The droplet interaction sites were synthesized by mixing a small amount of the magnetic PDMS (10 wt% MNPs) prepolymer with PDMS crosslinker in a 10:1 ratio then placing droplets of this precursor on the surface of a Petri dish in a straight-line pattern formation and then spreading this precursor on the surface of a Petri dish in the shape of the applied permanent rectangular magnet ( $H= 50$  mT) and leaving it to cure at 65 °C overnight.

**4.2.8 Fabrication of precursor droplet magnetic anchors (two small magnets)** The droplet interaction sites were synthesized by mixing a small amount of the magnetic PDMS (10 wt% MNPs) prepolymer and PDMS crosslinker in a 10:1 ratio, and then placing droplets of this precursor on the surface of a Petri dish in a straight-line pattern formation and then spreading this precursor on the surface of a Petri dish in the shape of the applied permanent square magnets ( $H=22$  mT) and leaving it to cure at  $65\text{ }^{\circ}\text{C}$  overnight.

#### **4.2.9 Fabrication of dispersed magnetic anchors**

The interaction sites were formed by placing a suspension of 5 wt% MNPs PDMS beads in a droplet in the center of a round Petri dish. The suspension separated and dried at the two poles of the applied small permanent magnets. ( $H=22$  mT) The suspension droplets were dried in the oven at  $65\text{ }^{\circ}\text{C}$  for a couple of hours.

#### **4.2.10 Fabrication of Mayer rod coated magnetic anchors**

Chained PDMS beads with 5 wt%  $\text{Fe}_2\text{O}_3$  MNPs were synthesized using a similar method to that described in Chapter 2 of this dissertation. The main difference was in the form of a further dilution of the beads (prior to curing) with 14 wt% PVA solution in either a 1:3 or 1:10 bead:PVA solution ratio. This addition of PVA was done to assist in the coating of the beads since the chained bead sample is more liquid-like prior to coating and would not be able to be coated effectively otherwise. The two ratios were chosen to attempt to make the sample more viscous in order to assist in the coating of the glass slide. Mayer rod #26 was the final chosen size for coating.

#### ***4.2.11 Fabrication of 3D printed homocomposite, PDMS capillary structures***

**1 wt%** magnetic PDMS beads: 1 wt% Fe<sub>2</sub>O<sub>3</sub> MNPs PDMS beads (1 wt% MNPs, 99 wt% PDMS) were synthesized and modified to 50 wt% magnetic beads to water in suspension.

**2.5 wt%** magnetic PDMS beads: 2.5 wt% Fe<sub>2</sub>O<sub>3</sub> MNPs PDMS beads 2.5 wt% MNPs, 97.5 wt% PDMS were synthesized and modified to 50 wt% magnetic beads to water in suspension.

**5 wt%** magnetic PDMS beads: 5 wt% Fe<sub>2</sub>O<sub>3</sub> MNPs PDMS beads were synthesized and modified to 50 wt% magnetic beads to water in suspension.

**10 wt%** magnetic PDMS beads: 10 wt% Fe<sub>2</sub>O<sub>3</sub> MNPs PDMS beads were synthesized and modified to 50 wt% magnetic beads to water in suspension.

Magnetic beads of desired magnetic concentration were vortexed and used to make the 3D printing capillary paste. Sylgard 184 PDMS base and crosslinker were mixed in a 10:1 ratio and then stirred using a commercial mixer at 750 rpm for five minutes in a disposable beaker to ensure homogenization. The resulting precursor was centrifuged and degassed. The magnetic beads and PDMS precursor were then mixed in a 6:4 ratio of beads: precursor with water as the runoff phase. Once mixed, the paste was then further refined at 600 rpm using the ServoDyne mixer for 5 minutes. A mortar and pestle were then used to further mix the capillary paste, taking note to have no clumps present as these could lead to clogging of the nozzle during 3D printing. The capillary paste was then loaded into the syringe to be used for the 3D printing.

The desired structure was extruded and printed using the corresponding MATLAB code at a pressure of approximately 60 psi. The resulting structures were then placed in the oven to cure at 65 °C for a couple of hours under an applied magnetic field between two small square magnets (H=18 mT). 3D printed structure samples that were used to image by microscopy were printed on

glass slides whereas the 3D printed structures used for rheological measurements were printed on disposable aluminum Peltier plates, top and bottom, of 20 mm diameter.

**4.2.12 3D printer specifications** The 3D printer used was a modified version of a computer numerical control mini-mill from OpenBuilds. The printer was customized to move a Nordson EFD syringe barrel instead of the CNC spindle the machine was designed for. The Pneumatic pressure was regulated by a Performus V Fluid Dispenser and delivered to the syringe barrel to provide controlled extrusion through a 27-gauge polyethylene nozzle. The syringe had movement in the x, y, and z direction.<sup>36</sup>

**4.2.13 Optical Microscopy** Optical microscopy (Olympus, BX-61) with an Olympus DP-70 digital CCD camera was used to characterize the morphology of the anchors, as well as the interactions between the PDMS beads with chained MNPs and the anchors and in the presence of an applied magnetic field.

**4.2.14 Rheological characterization of chained bead gels** Rheological analysis of the suspensions was performed using a DHR-2, TA Instruments (New Castle, DE) rheometer with disposable Peltier aluminum plates (diameter = 20 mm with 0.6 mm gap size). Sandpaper was used as a comparison to the 3D printed structures to minimize the effect of wall slip during the experiments. The angular frequency sweeps were conducted at 0.05% strain for  $100 - 0.05 \text{ rad s}^{-1}$ . The amplitude oscillatory measurements were conducted within the linear viscoelastic regime of the samples. All tests were performed at a constant temperature of 25 °C.

## 4.3 Results and Discussion

### 4.3.1 Other attempted magnetic anchoring techniques

#### *Precursor magnetic anchor sites*

The primary focus of the work presented in this Chapter was to effectively form magnetic structures that could act as “magnetic anchors” for the magnetically induced gels composed of the chained PDMS beads. Before using a 3D printing fabrication to do this, however, we attempted several other droplet and coating-based techniques. We will highlight some of the methods we used to try to achieve magnetic anchor sites below. The first technique involved using the magnetic 10 wt% MNPs PDMS precursor. No magnetic PDMS beads were present in the anchor site, it was simply composed of Fe<sub>2</sub>O<sub>3</sub> MNPs dispersed in PDMS Sylgard 184 prepolymer base. The base was then mixed with the PDMS crosslinker in a 10:1 ratio as in the case of the beads, however, no PVA was added, and no high shear was applied. The resulting precursor was then spread onto a round Petri dish in the shape of the applied permanent magnet. This technique was attempted with two different types of permanent NdFeB magnets. In the case of the large rectangular magnet, the magnet was placed under the Petri dish to give a resulting magnetic field of 22 mT while being cured overnight at 65 °C. In the case of the smaller square magnets, the magnets were placed both above and below the Petri dish with the prepolymer sample under an applied field of 18 mT while being cured overnight at 65 °C. This meant that both samples were placed under a vertical magnetic field. This configuration should result in the embedded magnetic particle moments aligning in the field direction in a chain-like formation, vertically, as this alignment is more energetically favorable.<sup>37</sup>

### *Precursor magnetic anchors*

The resulting 3D structures were too thick to visualize effectively under the microscope which meant that the interactions between the MNPs within the precursor anchor sites and the chained magnetic PDMS bead suspension would not be visualized. Thus, we wouldn't be able to confirm the presence of magnetic anchoring. Hence, we decided to modify this technique by forming droplets instead of a spread sample of precursor. We were able to do this using a pipette. The samples with precursor anchor sites (left) and droplets (right) magnetized using the large permanent magnet are shown in Figure 4.1a and the samples with precursor anchor sites (left) and droplets (right) magnetized using the two small permanent magnet are shown Figure 4.1b. At this point, we were able to effectively visualize the anchor sites. As see in Figure 4.1d (top), the droplets were about 1.5 mm in diameter and vertically aligned MNPs could be clearly distinguished. This vertical alignment was a result of the magnetic anisotropy caused by the dipolar interaction between the particles when aligned in the direction of the vertically applied magnetic field. The magnetic anisotropy of these magnetic particle chains enables controllable and directional actuation in three dimensions.<sup>37</sup>

The interaction between the droplet anchor sites and the chained PDMS beads in suspension could be conveniently visualized using microscopy. The chained beads in the suspension and the anchor sites were both magnetized during curing, however neither was magnetized additionally during imaging. It was observed that, the beads seem to aggregate along the outer part of magnetic anchors. The beads appeared to create a coffee ring-like effect around the periphery of the droplet as the sample dried. This observation aligns with previous findings in that in the absence of an external magnetic field, the magnetic beads are transported to the edge of the droplets during drying due to solvent evaporation, resulting in a magnetic bead-rich edge

(Figure 4.1d, bottom images).<sup>38</sup> There was an evidently different interaction observed if the beads were magnetized prior to adding them to the anchor droplet. Upon introducing a magnetic field ( $H=38$  mT), the chained beads seem to be attracted to the droplet and effectively “anchored” to its surface due to the magnetic attraction between the embedded MNPs in the beads and the vertical magnetic nanoparticles in the droplets (Figure 4.1d, middle images). All chained beads form a percolation network that can be traced to terminate at beads that are attached directly to the anchor droplet sites.

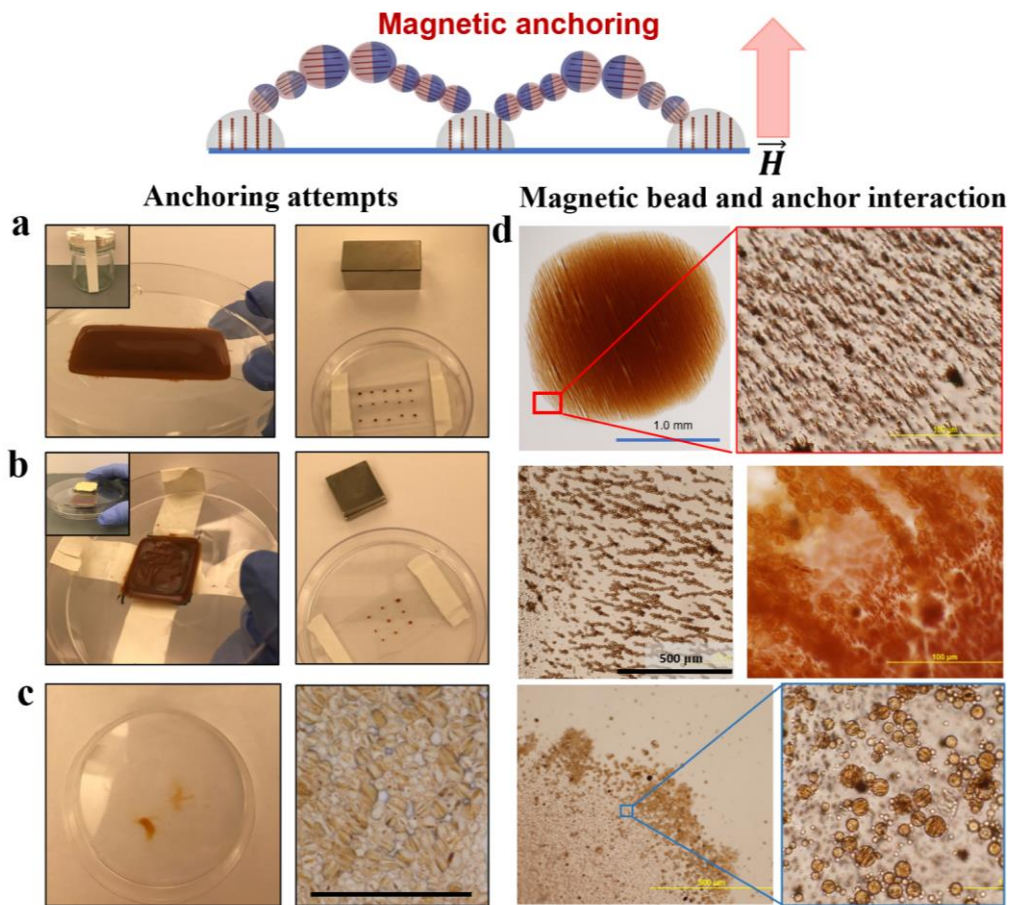


**Figure 4.1** Images of the set-ups from some of the different methods that were tested for making magnetic anchors. (a) Highlights the methods involving spreading magnetic PDMS precursor (10 wt% dispersed, shown on left) or forming droplets (right) and using a single large permanent NdFeB magnet ( $H= 50$  mT) to magnetize the  $\text{Fe}_2\text{O}_3$  MNPs. (b) Shows the methods involving spreading magnetic precursor (10 wt% dispersed, shown on left) and using two smaller permanent NdFeB magnets ( $H= 22$  mT, shown on the right). (c) Presents a method that includes a suspension of the magnetically aligned beads magnetized between two small permanent NdFeB magnets ( $H= 22$  mT). (d) (top left and right) Microscopy images of a 5 wt% MNPs droplet that was cured under the presence of the two smaller permanent magnets. The remaining microscopy images show how dispersed chained PDMS beads interact and anchor to the cured  $\text{Fe}_2\text{O}_3$  nanoparticles within a 1 wt% MNPs droplet.

### ***Dispersed magnetic anchors***

At this point, we had been able to prove that we could synthesize anchor sites for the magnetic chained beads, however, we aimed to form anchors that were composed of not only MNPs, but the actual beads as well. To do this, we placed a droplet of concentrated chained magnetic beads in the center of a Petri dish and applied a field of ( $H=22$  mT) using two small square magnets. The resulting drying droplet separated in two, attracted by both ends of the applied magnet. The sample was then dried in the oven at 65 °C. The set up (left) and resulting morphology (right) can be observed in Figure 4.1c. Although we had been able to dry a sample to create an anchor site composed of the beads as desired, this method lacked uniformity because we could not yet control the spacing and the size of the resulting dried sample if we introduced a magnetic field. Thus, our next goal was to be able to create anchor sites with uniform size, specifically, thickness.

### ***Mayer rod coated magnetic anchors***

We applied the Mayer rod deposition method to try to achieve anchor sites with uniform thickness. The Mayer rod deposition is a coating method that involves moving a wire-round stainless-steel metering rods to apply a coating onto a surface. Different sized rods result in different coating thickness and for the purpose of the experiments described in this Chapter, rod #26 was used. We sought the ability to visualize beads within the coating, not just magnetic nanoparticles as with the droplets. Hence, we decided to make and use chained PDMS beads. We emulsified the bead precursor as previously described using 14 wt% PVA and the Servodyne mixer. After this, we added more PVA in either a 1:3 or 1:10 PVA: emulsion ratio in order to make the sample more viscous since the sample is typically more liquid-like before curing. This would help the sample be coated onto the glass surface better. The sample was then coated onto the surface of the glass

slides using the Mayer rod and was then placed to cure overnight at 65°C under a vertical magnetic field gradient of ( $H=22$  mT) using two small square magnets placed above and below the glass slide, which was placed inside a Petri dish. Figure 4.2a presents two sets of finished and cured coatings of 1:3 (left) and 1:10 (right) composition. Since the magnets did not cover the whole coating area, two regions of beads formed within the coating. Figure 4.2b shows the beads within the coating cured in the vertical magnetic field in the 1:3 (left) and 1:10 (right) samples. Figure 4.2c shows the beads within the coating cured outside of the vertical magnetic field (within the field gradient) in the 1:3 (left) and 1:10 (right) samples.

As evidenced by the microscopy images, the beads formed under the vertical field gradient had vertically embedded MNPs and those beads formed outside of the field gradient had horizontally embedded MNPs. We then conducted an experiment to test how a suspension of 5 wt% chained beads interacted with the beads with chains within the coating. Figure 4.2.d shows the suspension beads (darker beads) successfully anchoring onto the beads within the coating (lighter colored beads). The diameter of the chosen Mayer rod resulted in a coating with beads of the same magnitude as the chained beads in suspension. The beads within the coating were chained and we could tune the alignment of these chains depending on what part of the coating we placed a droplet of chained bead suspension in. However, further improvements were needed. The Mayer rod coating technique was not ideal for our system because although we were able to synthesize the beads and coat them onto the surface, the addition of more PVA and likely the mechanical deformation caused by rolling the wire rod onto the glass slide to make the coating, resulted in non-spherical beads. Again, these non-spherical beads are within the coating on the glass slide. As can be seen in Figure 4.2b and c, some of the beads were slightly deformed. Some bead appeared more oval shaped. Furthermore, since we cured the beads directly onto the glass slide surface, we

did not apply the usual bead cleaning technique. This meant that we did not clean the sample and dispose of the smaller beads, resulting in an increase in polydispersity. Lastly, because the sample was still primarily liquid-like at the time of coating, the coating lines were not always uniform. In the 1:10 sample, some of the lines disappeared as the sample dried.

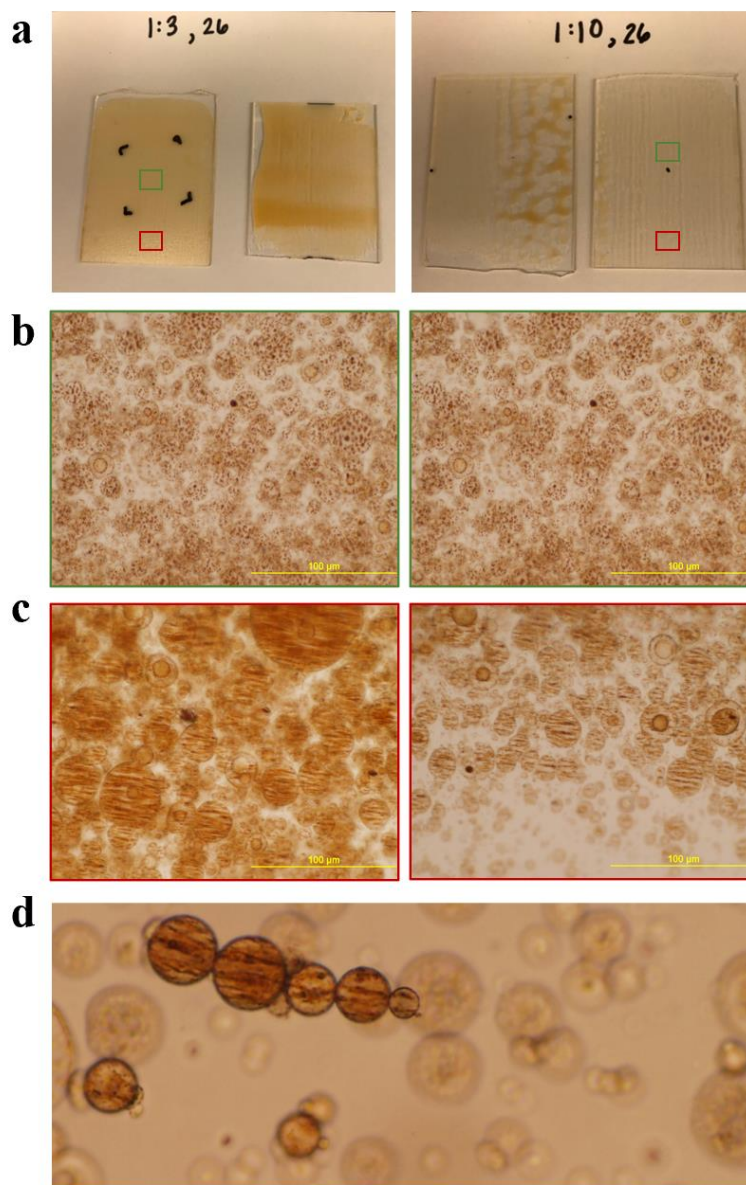


**Figure 4.2** Highlights of a promising magnetic anchoring method involving the Mayer rod technique. (a) Images of glass slides that were coated with different concentrations of PVA (used as diluent) using rod 26. (b) Images of beads that were cured under the presence of a vertical magnetic field, resulting in the visible vertical chains within the PDMS beads. (c) Beads that were not cured under the presence of the vertical magnetic field, resulting in the visible horizontal chains embedded in the PDMS beads. (d) Dispersed beads (10 wt% MNPs) interacting with the beads in the coating which are notably of the same size and structure.

### ***4.3.2 3D printed homocomposite, PDMS capillary structures***

3D printing using a technique previously developed by our lab appeared to be the best option for improving the uniformity and controllability of our anchor sites. As shown in Figure 4.3a, this 3D printing technique involves continuous extrusion of a magnetic capillary paste composed of chained PDMS beads being bridged together by PDMS. Our system was homocomposite since it was PDMS beads wetted and then bridged together by solid PDMS upon curing. Figure 4.3b shows an example of one of the structures being 3D printed. Figure 4.3c is a schematic of what our printed structure capillary bridges should look like and Figure 4.3d presents a microscopy image confirming that the ink looks as expected, with the chained PDMS beads being bridged by solid PDMS (clear in color).

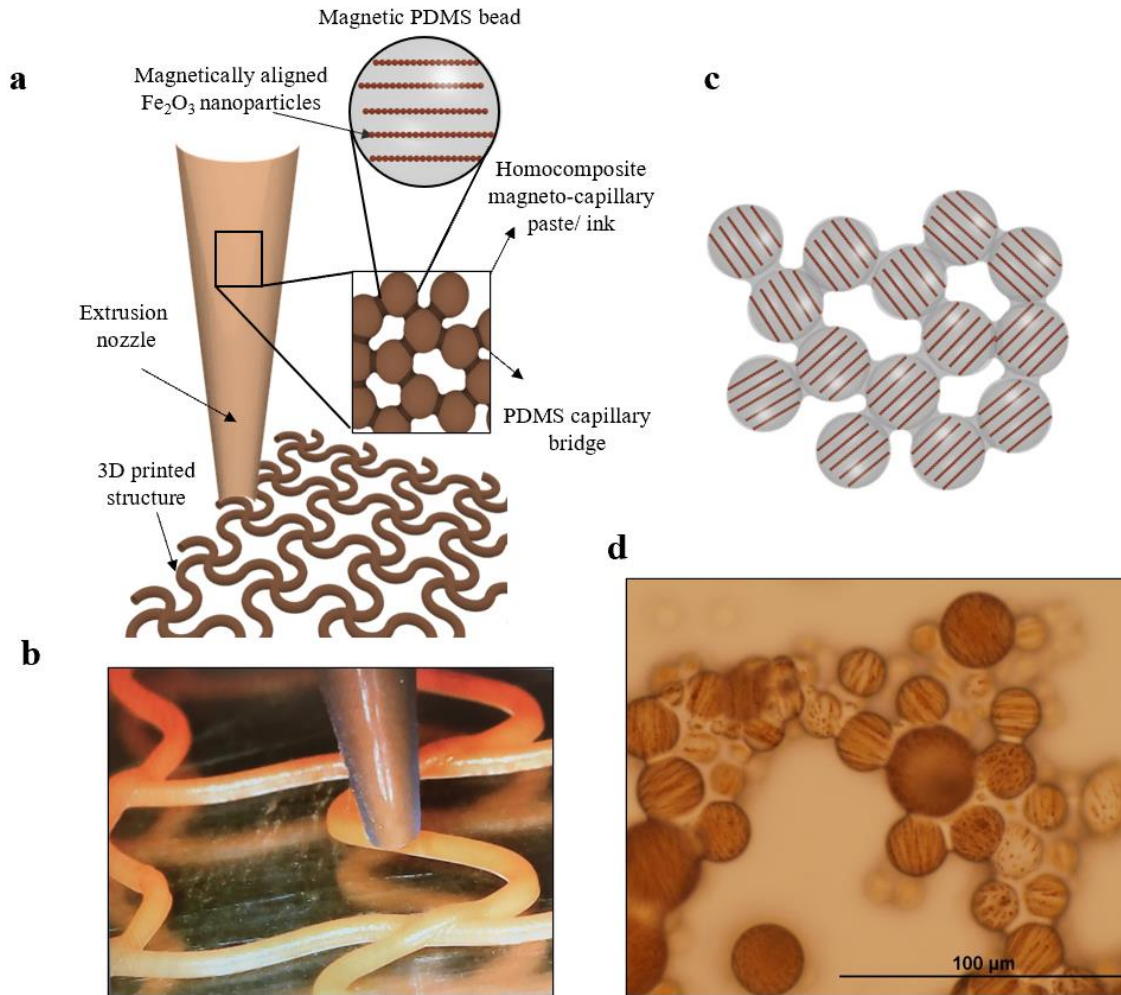


**Figure 4.3** Overview of the 3D-printing homocomposite technique used for shaping the structures from our chained PDMS beads. (a) Schematic of our 3D printing technique. The capillary paste is composed of the chained beads bridged together by PDMS. (b) An example of the 3D printing of one of the structures printed using this technique. (c) Schematic of the capillary paste composition. (d) Microscopy image of the cured capillary paste in a 3D printed structure.

The implementation of this technique involved using MATLAB or a similar program to code for the desired structure shape for extrusion. An example of a portion of a code is shown in Figure 4.4c. Once the code was finished, it needed to be uploaded to the 3D printing program. The

printer moved in the x and y direction to form the shape and in the z direction as each layer was printed to leave room for the new layer and to avoid touching the printed material with the nozzle tip. Figures 4.4a and b show examples of what the code preview looks like in MATLAB (left) and the resulting shape once printed (right) for the structure we referred to as “holey circle” and “grid circle” respectively.

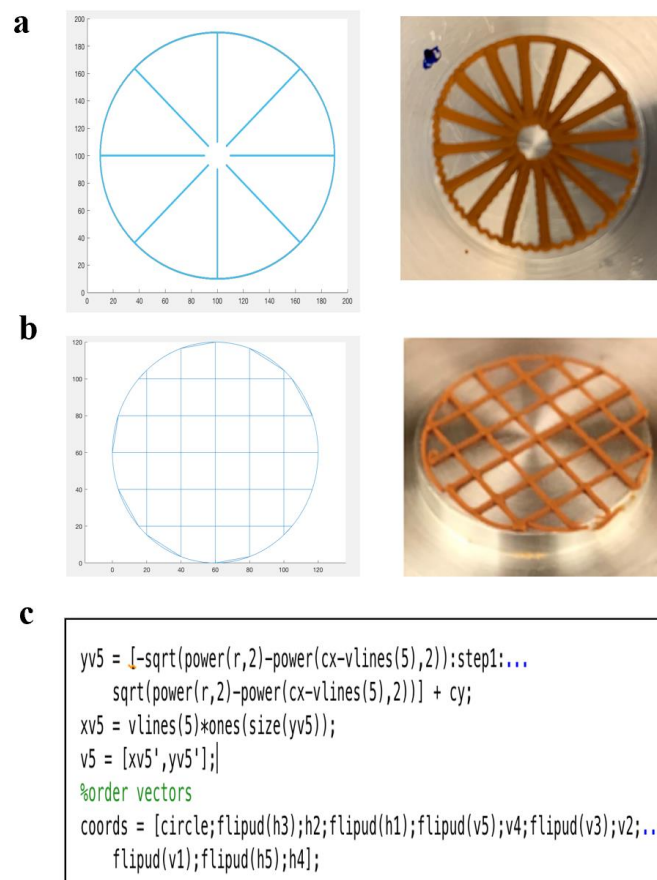


**Figure 4.4** 3D printing the structures involved MATLAB coding of desired structures. (a) MATLAB code projection of holey wheel structure (left) and actual printed structure on disposable rheometer plate (right). (b) MATLAB code projection of grid circle structure (left) and actual printed structure on disposable rheometer plate (right). (c) Example of what part of the code looked like for the grid circle structure.

An additional advantage of this technique was that although we didn't focus on printing multiple layers of ink for the structures, we were able to prove that our system could be printed up to at least 30 layers in a dog bone shape without collapsing (Figure 4.5b). This means that our ink could be used to print a variety of structures in 3D shapes. Figure 4.5a shows one of our most used shapes, a rectangle with a line, that we used (as described later in this Chapter) to study the magnetic interactions between the beads within the printed structures and the suspension of chained beads.

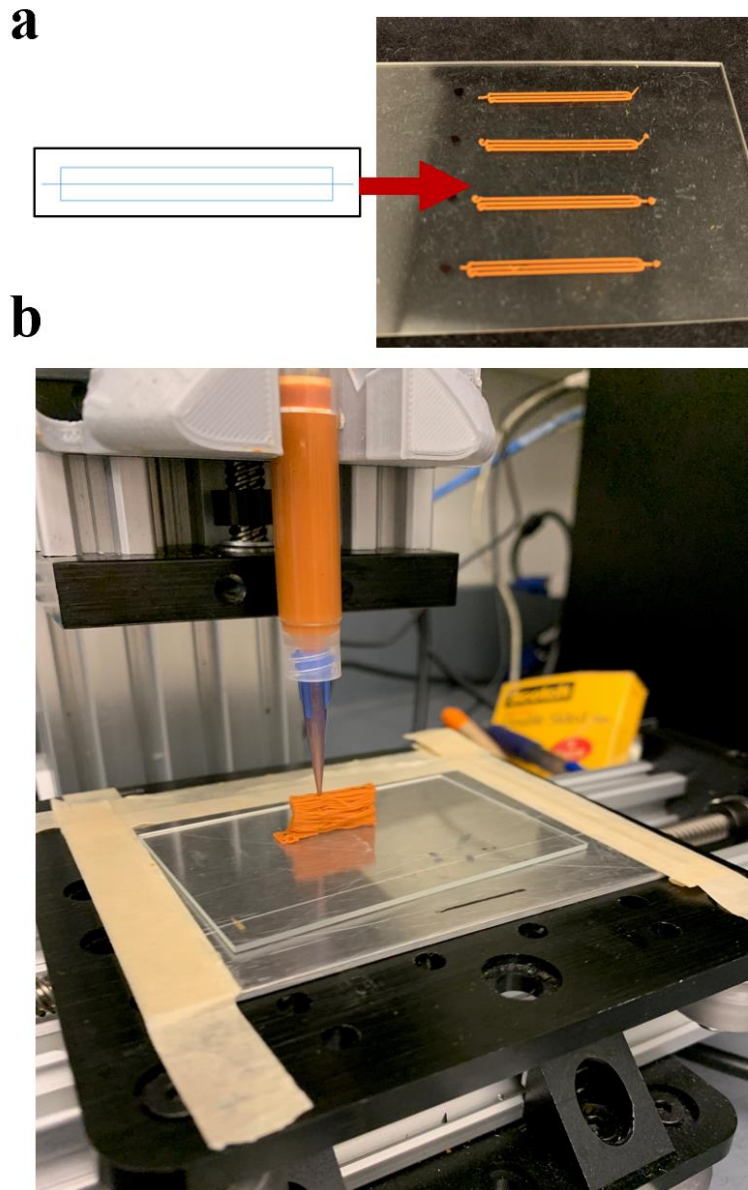


**Figure 4.5** (a) 3D printed rectangle used to study the magnet interaction of the chained beads within two printed lines. (b) 3D printing of dog bone shape demonstrated the versatility of this technique in that although we typically only printed one layer of material, we could deposit vertically at least up to 30 layers without the structure collapsing.

Optimization of the concentration of MNPs within the chained beads in the ink was necessary. It is well-known that the higher the amount of magnetic material present in a sample, the stronger the magnetic response of the system. Therefore, having ink with the highest fraction of magnetic material possible was essential. This could prove to be a barrier to imaging, however, as it was observed that the more magnetic material was embedded in our ink, the darker the ink was and the harder it was to visualize the structure using microscopy. Thus, we needed to find the optimal amount of magnetic material that could be in our structures but would still allow imaging to confirm magnetic alignment and interaction with suspensions.

Figure 4.6 shows microscopy images of different structures with increasing concentrations of MNPs that we incorporated in our chained bead capillary paste used to form the 3D printed lines. The images on the right show the beads within the ink. Notably, 1 wt% MNPs concentration was not ideal because it had the least amount of magnetic material possible. Moreover, this fraction of MNPs was not enough to form the chains of MNPs within the PDMS beads (Figure 4.6a). We attempted to use 10 wt% MNPs chained beads, however, they were not optimal either. Although the amount of magnetic material was favorable, the sample's magnetic particle concentration resulted in the ink being too dark to visualize. We were not able to effectively distinguish any beads and, more importantly, we were not able to see the embedded MNPs chains in the beads within the printed line (Figure 4.6d).

We next attempted to use beads with 5 wt% embedded and chained MNPs for the ink. The 3D printed line with this concentration could still not be well visualized using a 4× objective. By using a 50× objective, we were able to observe some of the beads within the printed line, however, further improvement was still needed (Figure 4.6c). Our final composition was 2.5 wt% chained and embedded MNPs. At this concentration we were able to visualize the printed line better using

a 10× objective. We were also able to better distinguish the beads within the printed line as well as the embedded chains (Figure 4.6d). This composition was used for the capillary paste for the printed structures going forward.

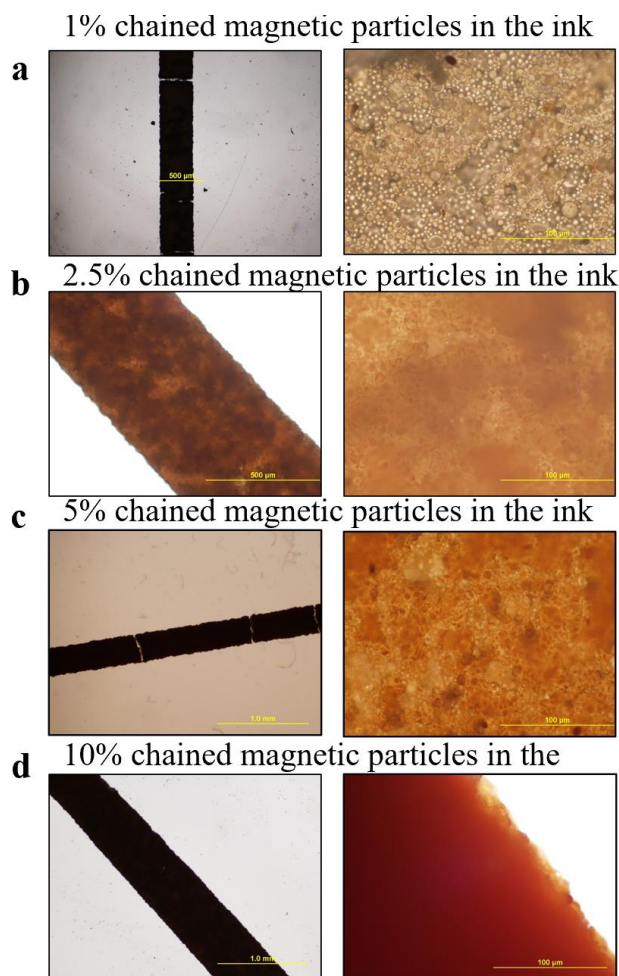


**Figure 4.6** Microscopy images of selected examples of printed lines with different loading amounts of embedded MNPs in the ink. (a) A 3D printed filament with 1 wt% embedded MNPs (left) and a cross section of the filament showing little magnetic material and no visible magnetic chains within the beads (right). (b) A 3D printed filament with 2.5 wt% embedded MNPs (left) and a cross section of the filament showing clearly visible magnetic chains within the beads. This was our final chosen loading amount. (right). (c) A 3D printed filament with 5 wt% embedded MNPs (left) and a cross section of the corresponding filament showing slightly visible magnetic chains within the beads (right). (d) A 3D printed filament with 10 wt% embedded MNPs (left) and a cross section of the filament. (right) The filament at this point is too dark and therefore the beads are no longer visible.

The optimal pressure to print our system was also a parameter that we needed to fine-tune. The outcome was largely dependent on the composition of the ink or the ratio of beads to capillary bridging liquid. Previous work has shown that higher magnetic particle concentration in a printed material results in higher modulus of elasticity of the material<sup>14,36</sup> Thus, the more magnetically chained beads our system enclosed, the more resistant it would be to deformation within the elastic range. This would also mean that the ink would be thicker which could potentially increase the chance of clogging during extrusion and would result in an increase in required pressure for extrusion.

We attempted several compositions including 7:3 and 6:4 chained beads: bridging liquid PDMS precursor for the ink. Our final composition of choice was 6:4. This composition resulted in little to no clogging during extrusion, an acceptable amount of minimum pressure required for extrusion, and flexible yet durable 3D printed structures. Although the pressure required could vary slightly depending on the 3D printed structure shape, the minimum pressure required was 50 psi and the typical pressure we used for all extrusions was 60 psi, +/- 10. Once the minimum amount of pressure required was reached, we could easily modify the thickness of the lines in our printed structure by adjusting the pressure. As can be seen in Figure 4.7a, the minimum pressure of 50 psi resulted in thinly printed lines whereas the maximum amount of pressure possible with our 3D printer, 100 psi (Figure 4.7b), resulted in thicker, flatter lines. It's important to note that the curing time was essential for this printing technique. As can be noted in some of the microscopy images from our earlier experiments, if the printed structures remained in the oven for too long, they could potentially crack resulting in an undesired discontinuity of the structure. This was something we observed in our systems most likely because we mostly printed structures with only one layer, meaning they had less material and therefore required less curing time than other more

elaborate 3D printed structures. For this reason, we limited our samples to a curing time of < 2 hours rather than the overnight curing for other syntheses we previously conducted.

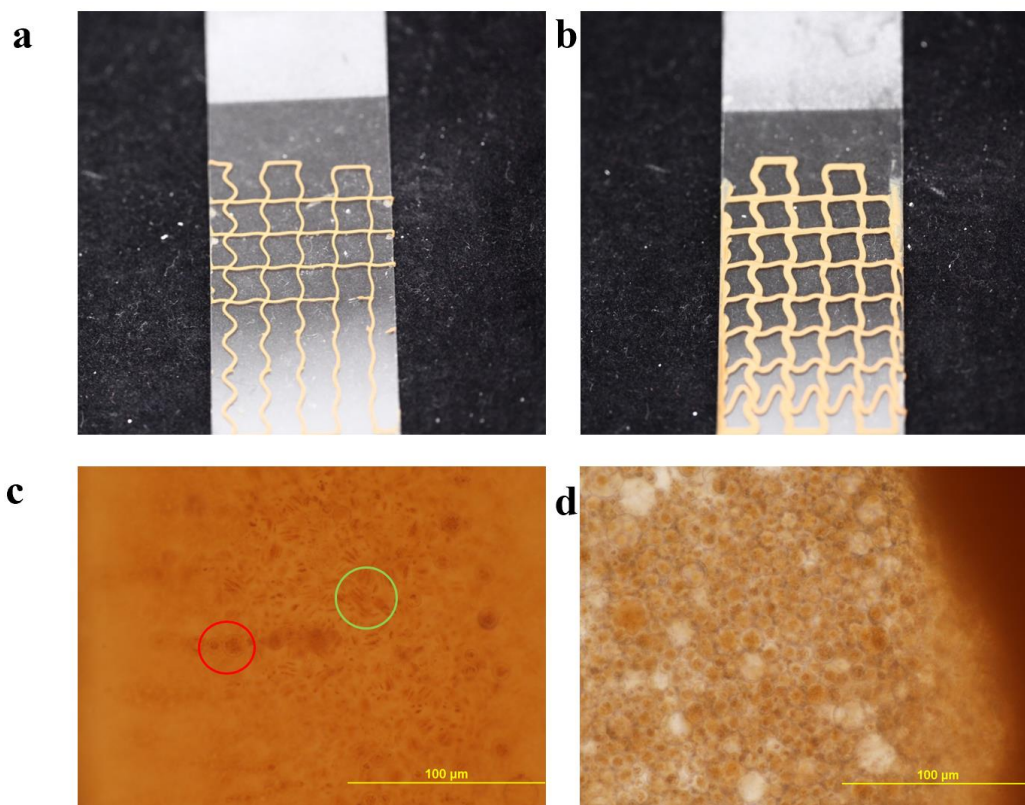


**Figure 4.7** The thickness of a 3D printed structure can be easily tuned by varying the pressure during extrusion. Once the minimum pressure for extrusion is reached, increasing the pressure further results in thicker printed lines. (a) A mesh printed at 50 psi and (b) a mesh 3D printed at 100 psi. The magnetic interaction of unchained beads with the 3D structures was also briefly investigated using microscopy. (c) Shows the unchained beads (example circled in red) interacting with the chained beads within the printed structure (circled in green). (d) A suspension of unchained beads interacting with the printed line in a non-structured way.

### *4.3.3 Magnetic interaction of soft magnetic gel and the 3D printed structures*

The magnetic interaction studies with beads in suspension were conducted for both chained and unchained beads in order to observe key differences in their interactions caused by the alignment or non-alignment of the embedded MNPs. As can be seen in Figure 4.7c, the unchained beads (circled in red) appear to be magnetically attracted to the counter-facing bead within the printed structure (circled in green). However, the unchained beads appear to simply aggregate near the anchor instead of forming percolated or branch networks (Figure 4.7d). This behavior correlates to the interactions we observed for these two bead types in Chapter 2. Aggregation is not favorable since we want to be able to see “bridging” chains from one printed structure to another for the structures to be effective anchor sites.

We then looked at the soft magnet gels composed of the chained beads and how they interacted with the printed structures. Figure 4.8a shows the morphology of our 3D printed structures as well as confirms that we are able to visualize the chained beads within the structure. Figure 4.8b shows the chained beads anchoring onto a printed line during a percolation network formation (top image). When a droplet of these chained beads was placed within two printed lines, we were able to confirm bridging behavior (bottom image). The sample of chained beads not only formed the percolation network, but this network traversed the whole area between the two printed structures, proving that these 3D printed structures are effective anchor sites for the chained beads and that they do not affect negatively their typical percolation network formation. As previously observed, these beads formed more flexible branched chains that connected to the 3D printed structures when no additional magnetic field was applied (Figure 4.8e) and formed better defined linear structures when a magnetic field was applied ( $H= 19$  mT). Figure 4.8e also shows chained beads on the outer edges of the printed ink interacting with the chained beads in suspension.

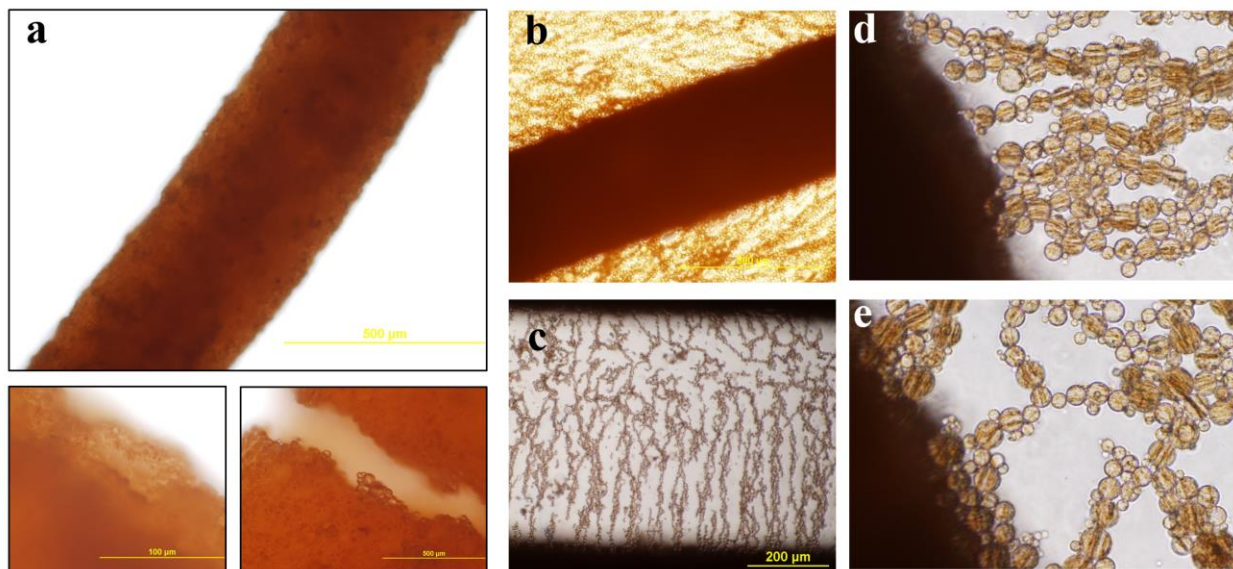


**Figure 4.8** The 3D printed line with the selected 2.5 wt% MNP and 6:4 composition and its interaction with a suspension of 5 wt% chained beads. (a) Microscopy images showing the morphology of the printed line and, specifically, visible chained beads within the printed structure. (b) A suspension of 5 wt% chained PDMS beads magnetically interacting with a single printed line. (c) A suspension of 5 wt% chained PDMS beads interacting between two 3D printed lines, demonstrating bridging behavior expanding from one printed structure (top) to the other (bottom). (d) A suspension of 5 wt% chained PDMS beads interacting with a printed structure after having been magnetized, showing more structured or aligned magnetic interaction. (e) A suspension of 5 wt% chained PDMS beads interacting with a printed structure with no prior magnetization after curing, showing more flexible branched structures composed of the chained beads.

#### ***4.3.4 Interaction of chained beads and printed structures under a rotating magnetic field***

The interaction of the chained beads with the printed structures was further explored under the presence of a rotating magnetic field. This was done to determine the pattern that the particles in

the chains will form and whether they would aggregate. A sample of the 5 wt% chained beads was placed between two printed lines on the glass slides and a rotating field of  $H=16$  mT was applied to the system. Figure 4.9a again illustrates the bridging behavior that the chained beads exhibit when placed in between two printed structures. Figure 4.9b shows the beads under a rotation of approximately  $45^\circ$ . As can be noted, although the beads respond and orient their embedded chains in the direction of the applied rotating field, the 3D printed anchor sites don't allow the top and bottom of the percolation to break apart do to the magnetic attraction between the chained beads in the ink and in the suspension closest to the structures. This has a ripple effect on the rest of the percolated structure. That is, the percolation network is slightly altered, but the overall location of the chained beads remains the same. In essence, the beads must first overcome their magnetic attraction to the 3D printed anchor site before being able to align in the direction of the applied field, resulting in the beads aligning but not disrupting the overall chained bead structure.

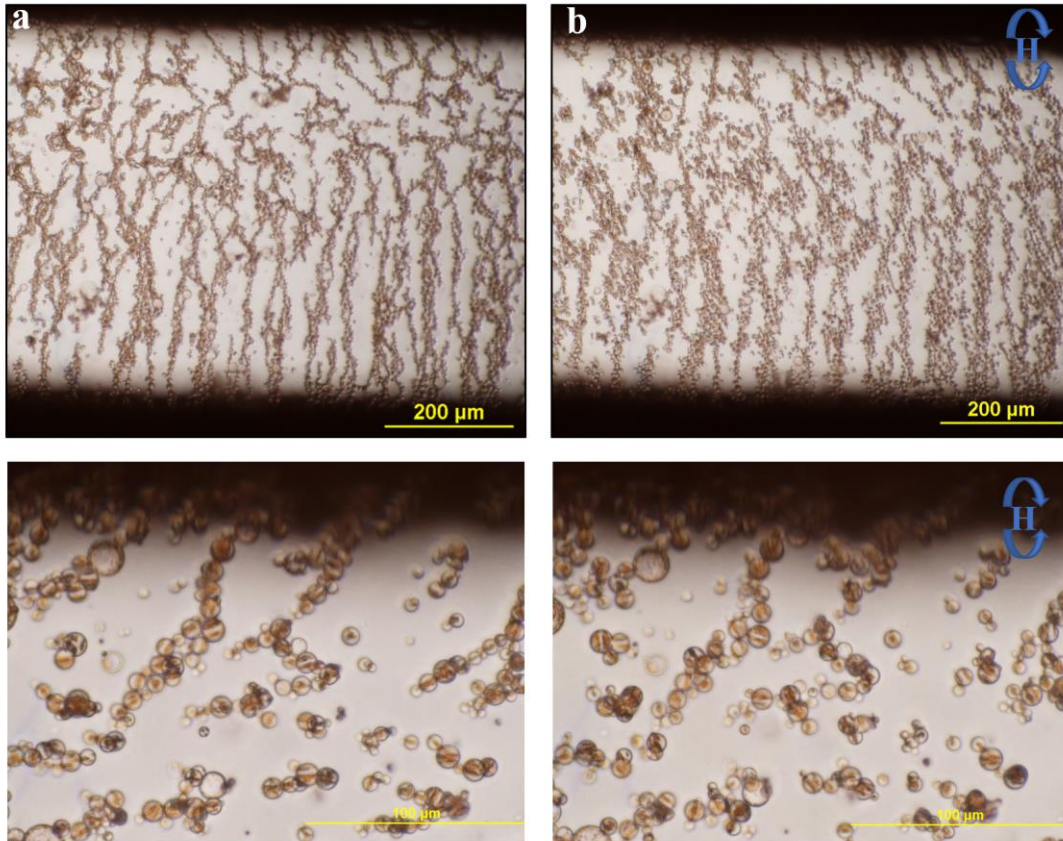


**Figure 4.9** (a) A suspension of 5 wt% chained PDMS beads forming a percolation network that expands through the whole area within two printed lines (top) and a closer view of the chained beads in suspension interacting with the top line (bottom). (b) 5 wt% chained PDMS beads in suspension being exposed to a rotating field ( $H= 16\text{mT}$ ). Although the percolated network of beads are partially disrupted when responding to the rotating field, they almost immediately re-form once the field is removed and the beads re-align (top) The beads appear to individually respond to the applied rotating magnetic field but stay approximately in the same position (bottom).

#### ***4.3.5 Demagnetization studies of the soft magnetic gel and 3D printed structures***

We conducted demagnetization studies on the chained bead suspensions within two printed lines. For these experiments, we used suspensions of varying concentration of MNPs: 2.5 wt% chained

beads, 5 wt% chained beads, and 10 wt% chained beads. The 3D printed lines in all of these experiments contained the 2.5 wt% chained beads used in the majority of the 3D printed structures discussed in this Chapter. A magnetic field of 19 mT was applied to each sample. The resulting morphology was imaged using microscopy. The samples were then demagnetized using a benchtop demagnetizer and the new morphology of the system was imaged using microscopy. All three samples were then re-magnetized with the same magnetic field as before, 19 mT, and the resulting morphology was again imaged using microscopy.

Microscopy images of the different conditions of the three sample concentrations are shown in Figure 4.10. The morphology of the samples with a suspension of 2.5 wt% chained beads can be observed in Figure 4.10a, containing images of samples being magnetized (left), demagnetized (middle), and re-magnetized (right). The morphology of the samples with a suspension of 5 wt% chained beads can be observed in Figure 4.10b and that of the suspension of 10 wt% chained beads can be observed in Figure 4.10c with the same magnetization pattern as in 4.10a. As can be observed in Figure 4.10a, the sample of 2.5 wt% chained beads formed a percolation network that spanned the whole area between the top and bottom printed lines. Clear straight branches of chained beads of mostly one bead diameter could be seen. The sample was then evidently demagnetized as the percolation formation was notably destroyed. Once the sample was re-magnetized, however, clear one diameter thick lines were again formed. In the case of 5 wt% chained beads, slightly thicker lines of chained beads percolated when the system was magnetized. When this system was demagnetized, most of the percolated network broke apart, however a few small branches of chained beads remained. When the sample was re-magnetized, a percolation network that was slightly thicker than the original formed. Finally, in the case of the 10 wt% chained bead sample, noticeably thicker branches of chained beads formed when the

sample was magnetized. Furthermore, when the system was demagnetized, it was clear that the demagnetizer wasn't as successful at randomizing the magnetic moment of the chained beads.

Once this final system was re-magnetized, the chained beads were able to reform thicker branches. Some of these observations have also been seen in similar systems previously. That is, it has been observed that the length and thickness of chains of magnetic material depends heavily on a number of factors, including the concentration of the magnetic material present.<sup>37</sup> Other parameters that can affect the thickness of these chains are drying conditions, field strength, and surface functionalization, which should all be the same between the three systems since we only varied the concentration of MNPs. Therefore, having the thickness of the branches of chained beads increase with amount of MNPs is expected. Having the system with the least amount of embedded MNPs, 2.5 wt% demagnetized more readily than that of the sample containing 10 wt% MNPs can also be explained. First, this sample contains less magnetic material and is thus less attracted to the applied field than the sample with the most amount of embedded MNPs. Secondly, because these beads are between the anchor sites, the beads must also overcome not only their internal residual magnetization, but also their magnetic attraction to the printed lines or magnetic anchor sites. Moreover, because the printed structures are a solid material with beads that cannot move or rotate, the beads in the printed structure likely retain some residual magnetization even after demagnetizing the sample.

From the experiments described above we were able to confirm that the printed structures can be visualized under the microscope with chained beads at a concentration of 2.5 wt% MNPs. More importantly, we were able to confirm that the printed structures are able to effectively serve as magnetic anchor sites, attracting the chained beads of all concentrations studied and resulting in a bridging behavior.

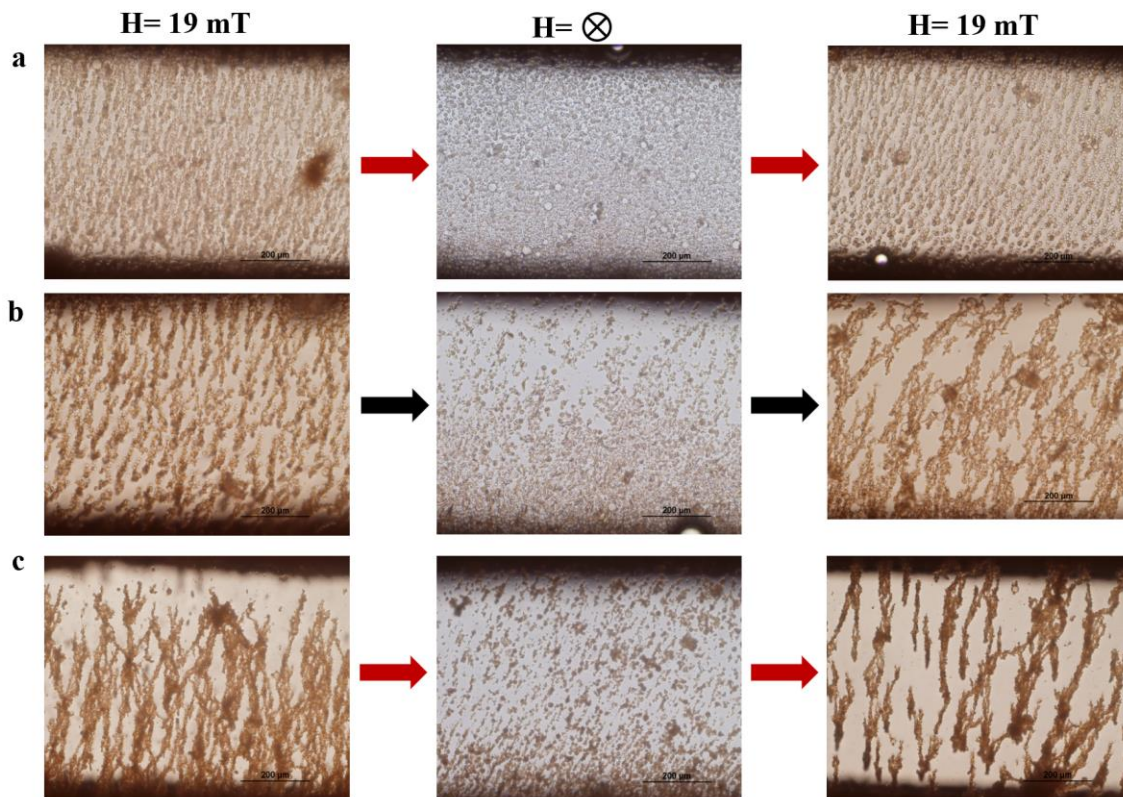


**Figure 4.10** Systems of chained bead suspensions of varying MNP concentration located within two 3D printed lines being magnetized, demagnetized and re-magnetized. (a) Suspension of 2.5 wt% chained beads magnetized and placed in between two printed lines, demonstrating bridging behavior and a percolation network (left). The same system after being subjected to a demagnetizing field, showing the chained beads no longer interacting with each other (middle). The same system once it was re-magnetized, resulting in the recovery of the percolation network of beads expanding the whole space within the printed lines. (b) 5 wt% chained beads show thicker aggregates within the percolated network. (c) 10 wt% chained beads showed even thicker chained bead aggregates in both magnetized (left) and re-magnetized (right) cases. The demagnetized system also does not appear to have been fully de-magnetized (middle).

#### ***4.3.6 Rheological characterization of the soft magnetic gels***

The rheological characterization of suspensions can often be faced with two barriers. First, the samples' liquid content can result in an increase in wall slip. Second, if the sample material has a high density, the sample may experience significant sedimentation during longer measurements. Both of these problems could result in erroneous results, and it is therefore of essence to find a solution. Based on the results from the previous section of this Chapter, we hypothesized that our 3D printed magnetic anchors could be a potential solution to this problem in the characterization of our chained bead suspensions.

Figure 4.11 highlights some of our rheology measurements using 3D printed anchor sites. All measurements were frequency sweeps of the 2.5 wt% chained beads at 30 wt% concentration of chained magnetic beads in suspension. We chose a more dilute suspension than we usually studied in order to have a more liquid-like sample. For these types of experiments, the resulting graphs give the storage ( $G'$ ) and loss ( $G''$ ) moduli as a function of frequency. Figure 4.11a demonstrates how we envisioned the sample would interact with the 3D printed magnetic structures on the disposable rheometer plate, based on what we observed using microscopy.

All samples demonstrated gel-like behavior with  $G' > G''$  throughout the whole frequency range, regardless of whether the sample was run using sandpaper or 3D printed structures on the rheometer plates. Preliminary results show that our printed structure surfaces with a wheel-like shape yield moduli that are at the same magnitude as these given by the samples run in sandpaper. 3D printed structures that were shaped more like a grid, however, resulted in moduli that were an order of magnitude lower than that of the sample run on sandpaper. These results were confirmed by repeating frequency sweep measurements using each shape of 3D printed structures. Further we tried to print structures that covered the whole rheometer plate. These attempts failed, however,

as the samples were too dry after curing and would fall apart. This confirmed that it isn't enough for there to be a coating of printed magnetic material on the plates, but that there must be a structure that can have points that serve as magnetic anchor sites. We next used a wheel-shaped circle with more lines to increase the number of anchor sites.

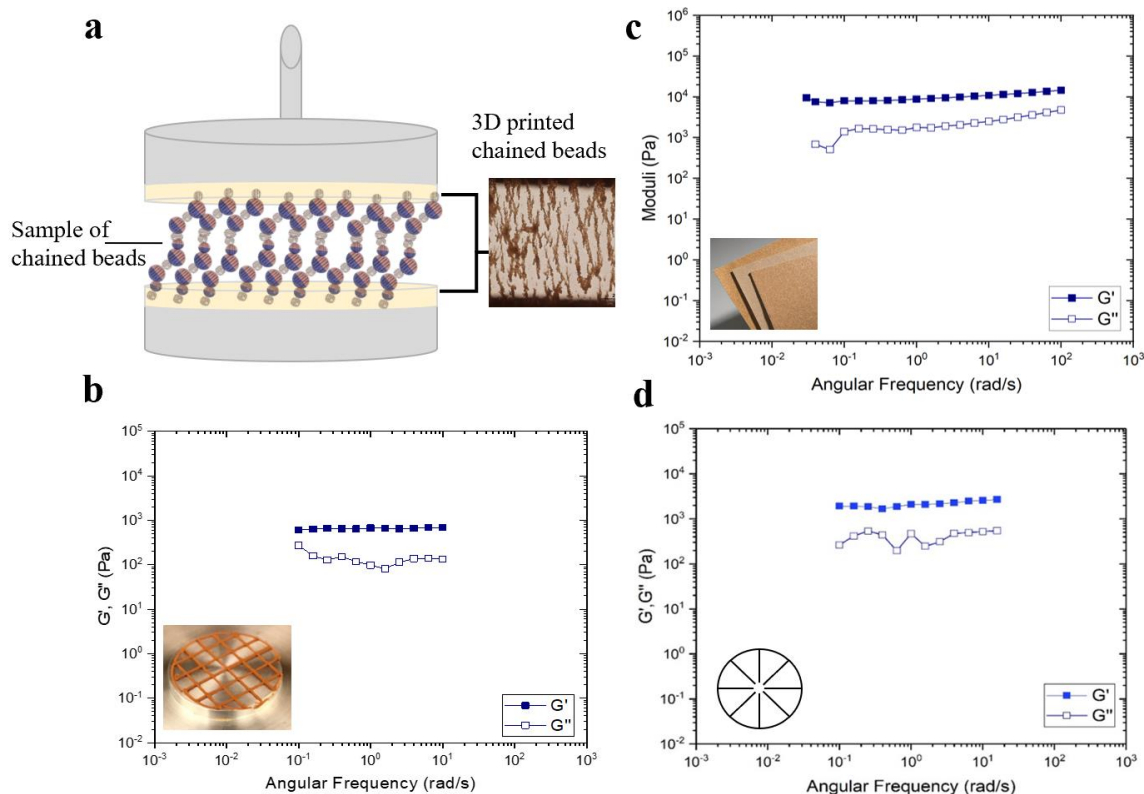


**Figure 4.11** (a) A schematic of a sample of the chained beads would interact with the printed structure on the rheometer plates. (b) A frequency sweep of a suspension of 2.5 wt% chained beads using a grid circle shaped 3D printed structure on the rheometer plate. (c) A frequency sweep of a suspension of 2.5 wt% chained beads using the traditionally used sandpaper on the rheometer plate (d) A frequency sweep of a suspension of 2.5 wt% chained beads using a wheel shaped circle 3D printed structure on the rheometer plate.

The 3D printed structures were so flexible and durable, that they were able to withstand the shear from the rheometer and remained in one piece and attached to the disposable rheometer plates. We were even able to run two different soft magnetic gel sample frequency sweeps using the same anchor (Figure 4.12a). Figure 4.12b shows that even after we removed the anchors from the rheometer plate after taking two sample measurements, the printed anchor site remained in great condition.

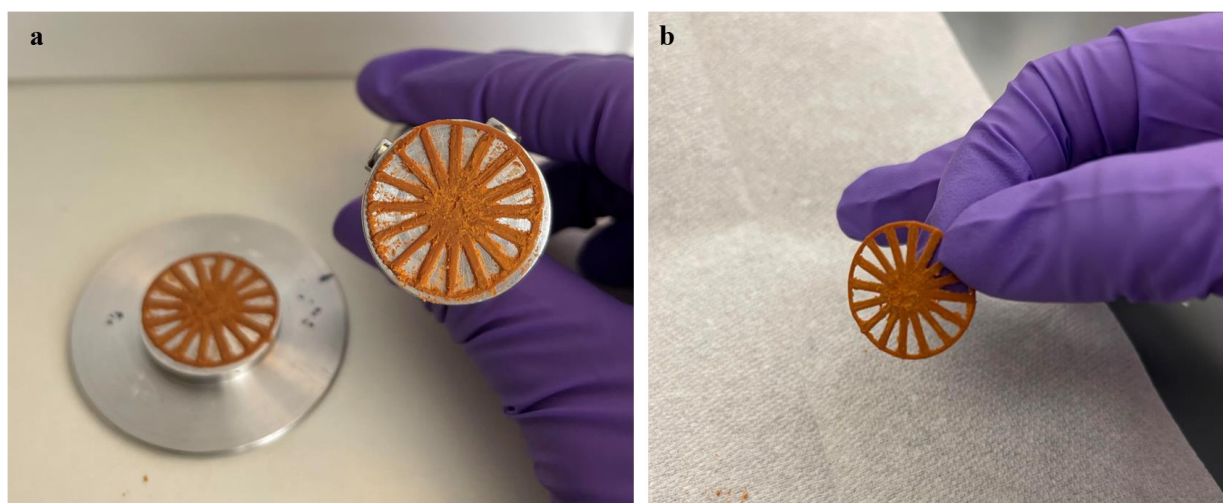


**Figure 4.12** Demonstration of the durability and flexibility of the printed anchor sites. (a) Shows what the wheel shaped magnetic anchor site looks like after taking two sample measurements. Intermittent cleaning was done to ensure anchors were only measuring the current sample. (b) Shows the 3D printed wheel anchor remains in one piece and in good condition after running two separate samples on it.

#### ***4.3.7 NdFeB as magnetic material in 3D printed structures***

We printed structures containing the NdFeB embedded PDMS beads that we briefly discussed in Chapter 2. Figure 4.13a shows the printed mesh structure containing 10 wt% NdFeB in the PDMS

beads. Figure 4.13b is a microscopy image of the morphology of the mesh that was printed that contained non-magnetized NdFeB microparticles. Lastly, Figure 4.13c shows microscopy images of a mesh that was magnetized during curing and that contained 10 wt% pre-magnetized NdFeB microparticles in the PDMS beads. As can be observed in the right image in Figure 4.13c, applying a magnetic field when curing the 3D printed mesh leads to the embedded NdFeB microparticles resembling magnetic cilia. This was a proof-of-concept experiment. Further work would be needed to study NdFeB PDMS beads as 3D printed magnetic anchor sites for rheological measurements if we decided to conduct more research on the NdFeB PDMS bead suspensions.

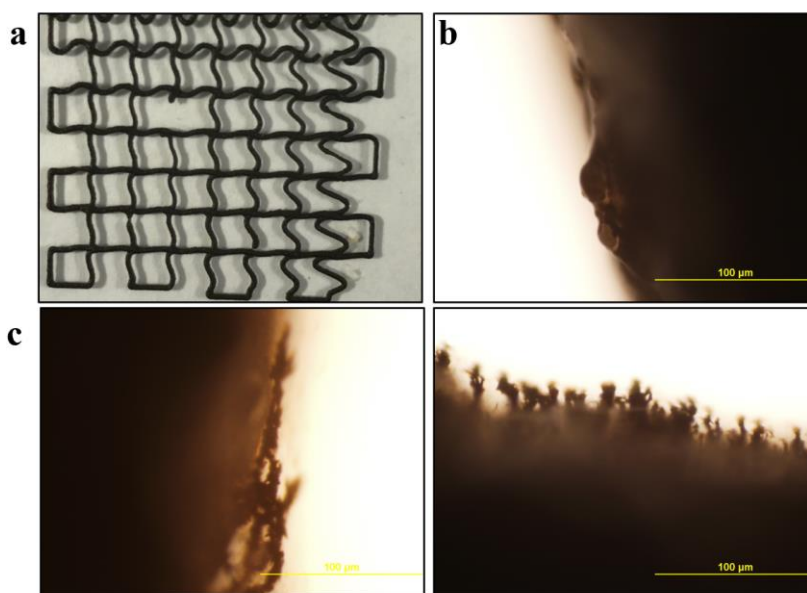


**Figure 4.13** (a) 3D printed mesh structure composed of 10 wt% NdFeB microparticles embedded in PDMS beads being bridged by PDMS and (b) a microscopy image of the morphology of a sample that was not magnetically aligned during curing. (c) Microscopy images of 3D structures that were cured under a magnetic field ( $H= 18\text{mT}$ ) with the left showing that the NdFeB microparticles are embedded in the structure and the right image showing the NdFeB particles resembling magnetic cilia.

#### 4.4 Conclusions

We present a facile, cost and time efficient, synthesis of capillary pastes for use in the 3D printing of soft magnetic anchor sites. We have shown that these printed anchor sites help reduce wall slip and potentially sedimentation, due to the magnetic interactions observed between the magnetically aligned PDMS beads in suspension and the same type of beads that can be found within the anchor sites. We were able to visualize this type of interaction microscopically. We envision that through this technique, rheological characterization in soft magnetic bead systems such as the one we have presented in this chapter, will be vastly improved. The 3D printed structures demonstrated good durability as they were able to withstand the shear from the rheological measurements and proved to remain in one piece. With intermediate cleaning, these 3D printed structures could potentially be used in multiple rheological sample measurements, decreasing cost and synthesis time required.

Further improvements such as rapid printing speeds and small length scales can lead to many possible applications for these magnetic anchor sites. 3D printing of these soft magnetic architectures allows for making of functional structures with magnetic reconfiguration. These magnetic structures can be rapidly and easily manipulated with the application of an external magnetic fields, leading to magnetic force being exerted onto the embedded magnetic nanoparticles as well as the capillary forces found between the magnetic PDMS microbeads. Although here we present these 3D printed structures as anchor sites, they could potentially also serve as active tissue scaffolds and could be key making in soft robotics components.<sup>39</sup> We have printed several other shapes and could print many others with multiple layers (Figure 4.14). Further studies are needed to characterize these structures in terms of their yield stress under shear and compression and their viscoelastic properties, amongst others. Several parameters such as the size of the embedded magnetic nanoparticles, the type of embedded magnetic nanoparticles, and the

intensity of the applied field during the curing of the structures could be explored further<sup>33</sup> in order to tune the strength of the dipolar moment interactions that lead to the assembly of the magnetic nanoparticles. Thus, further development and research of such structures include vast possibilities.

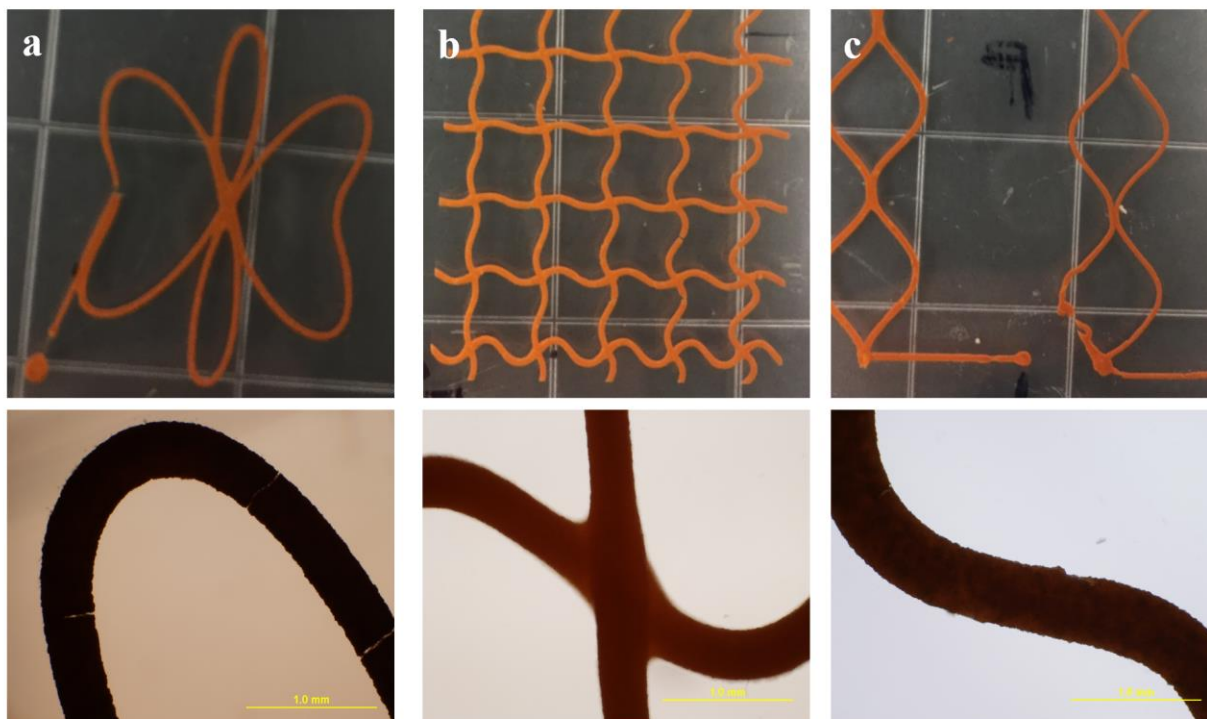


**Figure 4.14** Overview of other 3D printed magnetic structures demonstrating the vast possibilities enabled by the method. These structures include (a) a butterfly (b) a mesh (c) a diamond structure.

#### 4.5 Acknowledgements

The authors thank Dr. Lilian Hsiao and Dr. Saad Khan for generously providing the rheometer equipment and adapter as well as Lilian Okello for training on the 3D printer.

## 4.6 References

1. Highley, C.B.; Rodell, C.B.; Burdick, J.A. Direct 3D Printing of Shear-Thinning Hydrogels into Self-Healing Hydrogels. *Adv. Mater.* **2015**, *27*, 5075–5079.
2. Clausen, A.; Wang, F.; Jensen, J.S.; Sigmund, O. Lewis, J.A. Topology Optimized Architectures with Programmable Poisson's Ratio over Large Deformations. *Adv. Mater.* **2015**, *27*, 5523–5527.
3. Lewis, J.A. Direct Ink Writing of 3D Functional Materials. *Adv. Funct. Mater.* **2006**, *16*, 2193–2204.
4. Sommer, M.R.; Alison, L.; Minas, C.; Tervorrt, E.; Rühls, P.A.; Studart, A.R. 3D printing of concentrated emulsions into multiphase biocompatible soft materials. *Soft Matter*, **2017**, *13*, 1794.
5. Skylar-Scott, M.A.; Guasekaran, S.; Lewis, J.A. Laser-assisted direct ink writing of planar and 3D metal architectures. *PNAS*, **2016**, *113*, 6137-6142.
6. Shan, S.; Kang, S.H.; Raney, J.R.; Wang, P.; Fang, L.; Candido, F.; Lewis, J.A.; Bertoldi, K. Multistable Architected Materials for Trapping Elastic Strain Energy. *Adv. Mater.* **2015**, *27*, 4296–4301.
7. Lewis, J.A. & Gratson, G.M. Direct writing in three dimensions. *Mater. Today*, **2004**, *7*, 32-39.
8. Tumbleston, J.R.; Shirvanyants, D.; Ermoshkin, N.; Januszewicz, R.; et al. Continuous liquid interface production of 3D objects. *Science*, **2015**, *347*, 1349-1351.
9. Ladd, C.; So, J-H.; Muth, J.; Dickey, M.D. 3D Printing of Free Standing Liquid Metal Microstructures. *Adv. Mater.* **2013**, *25*, 5081–5085.
10. Parekh, D.P.; Ladd, C.; Panich, L.; Moussa, K.; Dickey, M.D. 3D printing of liquid metals as fugitive inks for fabrication of 3D microfluidic channels. *Lab Chip*, **2016**, *16*, 1812-1820.

11. Bollig, L.M.; Hilpisch, P.J.; Mowry, G.S.; Nelson-Cheeseman, B.B. 3D printed magnetic polymer composite transformers. *J. Magn. Magn. Mater.* **2017**, *442*, 97–101.
12. Hinton, T.J.; Hudson, A.; Pusch, K.; Lee, A.; Feinberg, A.W. 3D Printing PDMS Elastomer in a Hydrophilic Support Bath via Freeform Reversible Embedding. *ACS Biomater. Sci. Eng.* **2016**, *2*, 1781–1786.
13. Smay, J.E. Cesarano III, J.; Lewis, J.A. Colloidal Inks for Directed Assembly of 3-D Periodic Structures. *Langmuir* **2002**, *18*, 5429-5437.
14. Liu, F.; Alici, G.; Zhang, B.; Beirne, S.; Li, W. Fabrication and characterization of a magnetic micro-actuator based on deformable Fe-doped PDMS artificial cilium using 3D printing. *Smart Mater. Struct.* **2015**, *24*, 035015, 1-9.
15. Gladman, A.S.; Matsumoto, E.A.; Nuzzo, R.G.; Mahadevan, L.; Lewis, J.A. Biomimetic 4D printing. *Nat. Mater.* **2016**, *15*, 413-419.
16. Ceylan, H.; Yasa, I.C.; Yasa, C.; Tabak, A.F.; Giltinan, J.; Sitti, M. 3D-Printed Biodegradable Microswimmer for Theranostic Cargo Delivery and Release. *ACS Nano* **2019**, *13*, 3353–3362.
17. Wehner, M.; Truby, R.L.; Fitzgerald, D.J.; Mosadegh, B.; Whitesides, G.M.; Lewis, J.A.; Wood, R.J. An integrated design and fabrication strategy for entirely soft, autonomous robots. *Nature*, **2016**, *536*, 451–455.
18. Kolesky, D.B.; Truby, R.L.; Gladman, A.S.; Busbee, T.A.; Homan, K.A.; Lewis, J.A. 3D Bioprinting of Vascularized, Heterogeneous Cell-Laden Tissue Constructs. *Adv. Mater.* **2014**, *26*, 3124–3130.
19. Kolesky, D.B.; Homan, K.A.; Skylar-Scott, M.A.; Lewis, J.A. Three-dimensional bioprinting of thick vascularized tissues. *PNAS*, **2016**, *113*, 3179-3184.
20. Tang, J.; Yin, Q.; Shi, M.; Yang, M.; Yang, H.; Sun, B.; Guo, B.; Wang, T. Programmable shape transformation of 3D printed magnetic hydrogel composite for hyperthermia cancer therapy. *Extreme Mech. Lett.* **2021**, *46*, 1-9.

21. Huang, Z.; He, Y.; Chang, X.; Liu, J. Yu, L. et al. A Magnetic Iron Oxide/Polydopamine Coating Can Improve Osteogenesis of 3D-Printed Porous Titanium Scaffolds with a Static Magnetic Field by Upregulating the TGF $\beta$ -Smads Pathway. *Adv. Healthcare Mater.* **2020**, *9*, 1-13.
22. Babaei, S.; Shim, J.; Weaver, J.C.; Chen, E.R.; Patel, N.; Bertoldi, K. 3D Soft Metamaterials with Negative Poisson's Ratio. *Adv. Mater.* **2013**, *25*, 5044–5049.
23. Heger, Z.; Zitka, J.; Cernei, N.; Krizkova, S.; Sztalmachova, M. et al. 3D-printed biosensor with poly(dimethylsiloxane) reservoir for magnetic separation and quantum dots-based immunolabeling of metallothionein. *Electrophoresis*, **2015**, *36*, 1256–1264.
24. Song, H.; Spencer, J.; Jander, A.; Nielsen, J. et al. Inkjet printing of magnetic materials with aligned anisotropy. *J. Appl. Phys.* **2014**, *115*, 1-4.
25. Roh, S.; Parekh, D.P.; Bharti, B.; Stoyanov, S.D.; Velev, O.D. 3D Printing by Multiphase Silicone/Water Capillary Inks. *Adv. Mater.* **2017**, *29*, 1701554, 1-7.
26. Hodaei, A.; Akhlaghi, O.; Khani, N.; Aytas, T.; Sezer, D. et al. Single Additive Enables 3D Printing of Highly Loaded Iron Oxide Suspensions. *ACS Appl. Mater. Interfaces*, **2018**, *10*, 9873–9881.
27. Lazarus, N.; Bedair, S.S.; Smith, G.L. Creating 3D printed magnetic devices with ferrofluids and liquid metals. *Addit. Manuf.* **2019**, *26*, 15–21.
28. Qin, Z.; Compton, B.G.; Lewis, J.A.; Buehler, M.J. Structural optimization of 3D-printed synthetic spider webs for high strength. *Nat. Commun.* **2015**, *6*, 1-7.
29. Nie, J.; Gao, Q.; Qiu, J-j.; Sun, M.; et al. 3D printed Lego®-like modular microfluidic devices based on capillary driving. *Biofabrication* **2018**, *10*, 1-10.
30. Hong, S.; Sycks, D.; Chan, H.F.; Lin, S.; Lopez, G.P.; Guilak F.; Leong, K.W.; Zhao, X. 3D Printing of Highly Stretchable and Tough Hydrogels into Complex, Cellularized Structures. *Adv. Mater.* **2015**, *27*, 4035–4040.

31. Castellanos, N.I.; Bharti, B.; Velev, O.D. Field-Driven Reversible Alignment and Gelation of Magneto-Responsive Soft Anisotropic Microbeads. *J. Phys. Chem. B*, **2021**, *125*, 28, 7900–7910.
32. Lin, H-Y.; Huang, H-Y.; Shiue, S-J.; Cheng, J-K. Osteogenic effects of inductive coupling magnetism from magnetic 3D printed hydrogel scaffold. *J. Magn. Magn. Mater.* **2020**, *504*, 1-8.
33. Pissanello, F.; De Paolis, R.; Lorenzo, D.; Guardia, P.; Nitti, S. Monti, G.; et al. GHz Properties of Magnetophoretically Aligned Iron-Oxide Nanoparticle Doped Polymers. *Appl. Mater. Interfaces* **2013**, *5*, 2908–2914.
34. Kokkinis, D.; Schaffner, M.; Studart, A.R. Multimaterial magnetically assisted 3D printing of composite materials. *Nat. Commun.* **2015**, *6*, 1-10.
35. Khatri, B.; Lappe, K.; Noetzel, D.; Pursche, K.; Hanemann, T. A 3D-Printable Polymer-Metal Soft-Magnetic Functional Composite—Development and Characterization. *Materials* **2018**, *11*, 1-12.
36. Roh, S.; Okello, L.B.; Golbasi, N.; Hankwitz, J.P. et al. 3D-Printed Silicone Soft Architectures with Programmed Magneto-Capillary Reconfiguration. *Adv. Mater. Technol.* **2019**, *4*, 1-6.
37. Mishra, S.R.; Dickey, M.D.; Velev, O.D.; Tracy, J.B. Selective and directional actuation of elastomer films using chained magnetic nanoparticles. *Nanoscale*, **2016**, *8*, 1309-1313.
38. Lee, J.G.; Porter, V.; Shelton, W.A.; Bharti, B. Magnetic Field-Driven Convection for Directed Surface Patterning of Colloids. *Langmuir*, **2018**, *34*, 15416–15424.
39. Jang, K-I.; Chung, H.U.; Xu, S.; Lee, C.H. et al. Soft network composite materials with deterministic and bio-inspired designs. *Nat. Commun.* **6**, 2015, 1-11.

## CHAPTER 5

### Conclusions and Future Directions

#### 5.1 Summary

The aim of this dissertation is to develop novel magneto-capillary networks and to understand the means of their control and actuation. In the research described in Chapter 2, we focused on the synthesis and interactions of two types of magneto-colloidal microbeads. We were able to formulate soft micromagnet PDMS beads with embedded, randomly distributed  $\text{Fe}_2\text{O}_3$  MNPs. By applying an external magnetic field during curing, we were able to synthesize beads with magnetically aligned  $\text{Fe}_2\text{O}_3$  MNPs that demonstrate residual polar magnetization. We proved the tunability of this system by conducting magnetization, demagnetization, and re-magnetization experiments that provided conclusive evidence of the reformation of percolating networks. We characterized each bead type using rheology and demonstrated that the beads have noticeably different physical properties. We characterized the magnetic properties of each bead type using magnetometry. To the best of our knowledge, the chained bead suspension presented a peculiar split hysteresis loop that has not been observed before. This suggests that new physical mechanisms within the suspension could lead to this unexpected behavior, potentially driven by the beads' ability to rotate freely. We observed that the beads with chained MNPs aligned in the direction of Earth's magnetic field and confirmed that they did so by calculating the amount of energy required for them to do so and proving that the interaction energy can overcome  $kT$  during the re-alignment process.

The studies in Chapter 3 focused on intersecting important capillary and magnetic interactions to synthesize two types of magneto-capillary gels. We were able to show operational capillary bridging forces at a scale of dense microscopic gel samples and demonstrated that an

external magnetic field could direct the aggregation of the system through its inherent magnetic response. We formulated two novel types of magnetically responsive capillary gels containing magnetic nanoparticles, silicone beads, liquid fatty acid, and water medium. We established that the formation of capillary bridges between the PDMS microbeads via the addition of a secondary, immiscible fluid such as oleic acid leads to well-developed, gel-like behavior. We enabled the formation of smart gels by incorporating magnetic nanoparticles into either the PDMS microbeads with randomly distributed magnetic nanoparticles (MNPs) or by using MNPs randomly dispersed within the liquid OA (oleic acid) capillary bridges. The gel with MNPs in the capillary bridges was magnetically responsive capillary gel (MRCG) type 1 and the gel with MNPs within the PDMS beads was MRCG type 2. We characterized the properties of the MRCG Types 1 and 2 with respect to rheology, magnetic response, and ability to re-assemble on field application. One other important research result is that we proved that both of these MRCGs exhibit the property of magnetic field induced self-repair, which can happen both in air and water. The self-repair occurs as a result of the re-formation of the capillary bridges between the beads, when the two pieces of the cut gel are pulled together by the action of the externally applied magnetic fields. We were able to confirm that the gels were reconstituting to single material using rheological characterization.

Finally, the work described in Chapter 4 highlights the research that we have begun using magnetic interaction sites to study and manipulate the magnetic response in our suspensions of chained beads. We optimized their magnetic anchor sites and used a continuous extrusion-based 3D printing technique to get homocomposite, PDMS-based magneto-capillary structures. This allowed our structures to be reproducible and uniform with good flexibility and durability. The formation method of these structures also enables their high tunability. By modifying the extrusion

pressure, we are able to control the thickness of the 3D printed features. We showed that modifying the amount of loaded MNPs has a direct relationship with the magnetic response of the structures. We have introduced these 3D printed structures as potential substitutes for the traditionally used sandpaper for rheological characterization of our chained bead suspensions. The goal is to reduce the possibility of wall-slip affecting the measurement and decreasing any potential sample sedimentation due to the beads' magnetic attraction to the 3D printed anchors. Current results point to the printed structures providing efficiency of rheological measurements fully comparable to the samples run using sandpaper surfaces.

## **5.2 Future Outlook**

As we move forward, more advanced studies could be done to further understand the magnetic interactions between our magnetically anisotropic and chained PDMS beads in suspension. Future work could include molecular or discontinuous molecular dynamics simulations to better understand the formation of percolation networks as well as to predict their interactions and network structure at different magnetic and polymer bead concentrations. As presented in Chapter 2 of this dissertation, we believe that the maximum amount of possible embedded nanoparticles for our magnetic beads could be somewhere between 20 wt% and 25 wt%. Using these studies, we could possibly calculate and maximize the magnetic response of our system while ensuring that no magnetic material is left outside of the PDMS beads in suspension. Moreover, future studies could include using an electromagnetic field of time-variable configuration, rather than a static magnetic field using permanent magnets as we have done until now. Preliminary work involving an electromagnetic field showed that the 5 wt% chained beads also align in the direction of Earth's magnetic field at both 0.51T and 0.84T applied field strength (Figure 5.1). For these experiments,

we emulsified the chained beads and before curing, placed the curing chamber with the beads inside electromagnetic field at one of the two previously mentioned strengths for 5 minutes before the chamber was placed in the oven for curing.

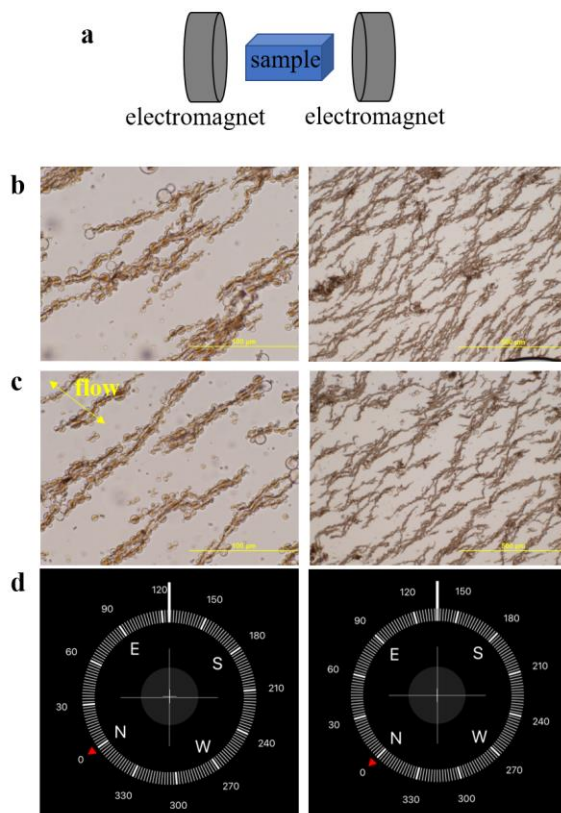


**Figure 5.1** Demonstration of applying an electromagnetic field to our chained beads system rather than the static magnetic field using a permanent magnet. (a) Schematic of the set up of the electromagnetic field with the sample of emulsified, but not yet cured, chained beads. (b) Microscopy image of 5 wt% chained beads in suspension cured after applying electromagnetic field of 0.51 T. (c) Microscopy image of 5 wt% chained beads in suspension cured after applying an electromagnetic field of 0.84 T. (d) Compasses confirming that the orientation of the branched structures formed by the chained beads are in the direction of Earth's magnetic field for the beads cured using a 0.51T (left) and 0.84T (right).

Potential future simulation studies of this system could also include the modeling of the fractal patterns created when drying chained beads in suspension. The preliminary work that we have conducted shows that different fractal patterns are formed when drying samples of chained beads with varying MNP concentrations, MNP alignment, and overall suspension concentrations (Figure 5.2). Moreover, the drying times and patterns differ as these parameters are changed. That is, it takes different amounts of time to dry samples depending on their condition. Moreover, the samples appear to form larger aggregated patterns as well as less complex structures upon drying as the concentration of beads in suspension increases. Furthermore, we looked at the samples both without applying magnetic field before imaging (not shown) and after being magnetized (as seen in Figure 5.2). Overall, the data from almost 300 images of the samples at different conditions shows that we could predict the potential fractal arrangements of chained bead suspensions under different conditions. This process could in the future be used to fabricate new types of layers with variable morphology for applications such as deposition of superhydrophobic or special tribology coatings on surfaces.

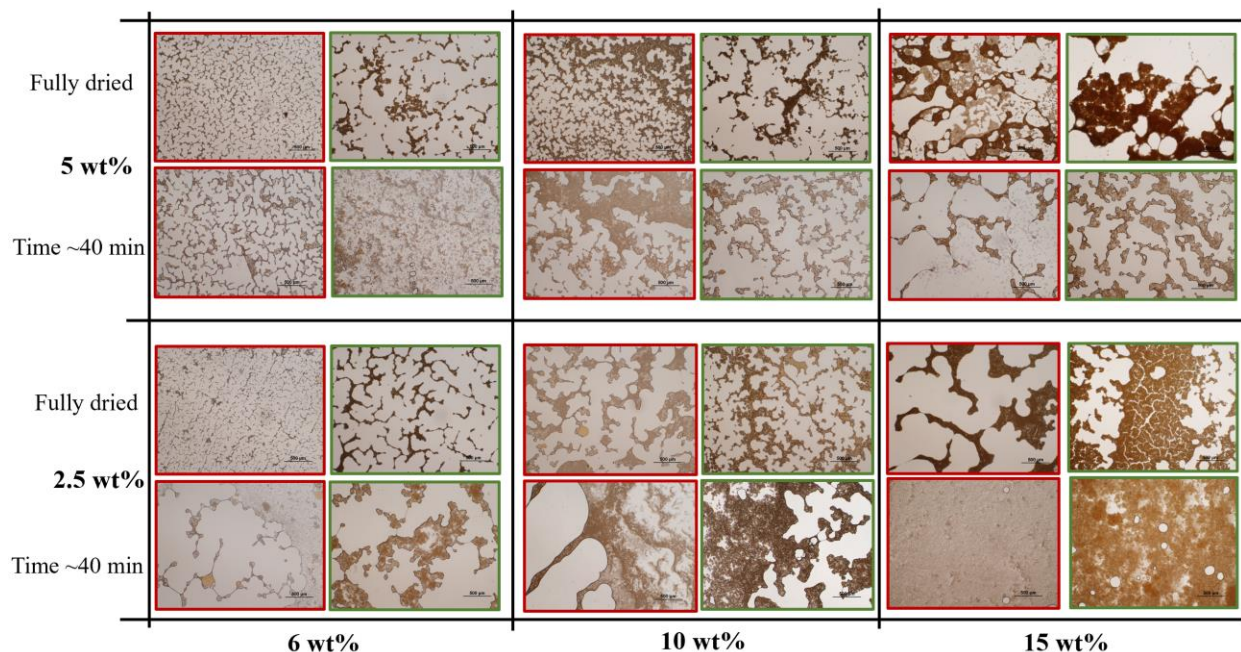


**Figure 5.2** Drying pattern study of 2.5 wt% as well as 5 wt% magnetically aligned and randomly distributed MNPs in PDMS beads at 3 different concentrations of the magnetic beads to water, 6 wt%, 10 wt%, and 15 wt% at two different drying times, after 40 minutes and after the sample was fully dried. Red outline denotes chained beads samples and green outline denotes unchained beads or beads with randomly distributed MNPs.

Moreover, we were not as of yet able to observe in great detail the structure of the individual chains of MNPs embedded in the PDMS beads, even at 2.5 wt% MNPs. The imaging capabilities in this study did not have high enough resolution to distinguish individual MNPs embedded in the PDMS beads. Finding a way to synthesize individual chains of MNPs within the beads would allow us to draw an even greater analogy to magnetotactic bacteria. Thus, future use of AFM-based techniques such as magnetic force microscopy, could shed more light in terms of the MNP chain size within the beads.<sup>1</sup> Additionally, it could prove beneficial to measure the dispersion stability of our bead suspensions using a Turbiscan.<sup>2</sup> Although we ensured that our

samples were well-dispersed during imaging and characterizations, this is an important property to understand, especially when considering potential future applications for our suspensions. As magnetization can lead to local heating,<sup>3</sup> it could be useful to confirm that any heating is negligible. One other system that we believe would be interesting to explore further experimentally and potentially computationally, would be a system of mixed particles of both randomly distributed MNP PDMS beads and magnetically aligned PDMS beads. Thus far, we have mixed a sample of 5 wt% magnetically aligned beads and 5 wt% randomly distributed PDMS beads and looked at them microscopically, however future work is needed to understand how their interaction will be impacted by their varying MNP distribution.



**Figure 5.3** Microscopy images of a mixed suspension of 5 wt% magnetically aligned beads and 5 wt% randomly distributed PDMS beads.

In Chapter 3 of this dissertation, we presented the rheological characterization of two types of magneto-capillary gels. We included work that focused on the effect of placing our gels in

different temperature conditions for extended periods of time with varying concentrations of bridging material. These experiments were all performed at room temperature, after the gels were stored under varying temperature conditions. It could also be beneficial to determine the effect of varying the temperature of the sample during the actual rheology measurement and its impact on the gels' physical properties. Furthermore, studying gels within the physiological pH range could be a large step towards the development of new functional gels for biomedical applications.

Lastly, in Chapter 4 of this dissertation, we presented the process and data of using 3D printed magnetic anchor sites for studies of PDMS bead suspensions. We conducted demagnetization studies and observed that as the amount of MNPs embedded in the PDMS increased, the demagnetization of the suspension appeared to be less effective. Further work on this complex system could include conducting demagnetization studies on chained beads whose embedded MNPs are analyzed using an electromagnetic field instead of a permanent magnetic field as we have done up until now. Preliminary data (not shown) proved that the beads aligned using an electromagnet readily demagnetized using a demagnetizer, which lead us to believe that beads with MNPs aligned using an electromagnet could potentially more readily demagnetize even when included inside 3D printed structures. Furthermore, we presented preliminary rheological characterization of our chained bead suspensions using 3D printed structures on disposable rheometer plates. It became clear that printed structures with radial symmetry such as the wheel circle design gave results with higher moduli for the chained beads suspensions than that of other printed patterns such as the grid circle design. This leads us to believe that the wheel-like structures are the type of anchors that we should focus on for optimization. Additionally, we attempted to print structures that could cover the whole rheometer plate; however, we were not able to correctly translate the MATLAB code to the 3D printer program in a way that would make the structure

print correctly. We attempted to spread the capillary paste onto the rheometer plate surface, but this resulted in a crumbly structure that performed poorly. These results emphasized that covering the whole surface does not result in any type of anchor sites. We could potentially coat a surface for other applications using a 3D printing technique; however, we would need to continue developing and modifying our approach further in order to attain this.

Overall, the primary contribution of the work presented in this dissertation is the enabling knowledge of how to synthesize new classes of soft magnetically responsive beads with variable structure and magnetic retentivity. These beads can form numerous gels with interesting properties by either long-ranged magnetic forces or short-range capillary bridging. They constitute a rich structural and interaction toolbox of novel magneto-responsive networks that can be applied to a variety of responsive and functional colloidal systems.

### 5.3 References

1. Schreiber, S.; Savla, M.; Pelekhov, D.V. et al. Magnetic Force Microscopy of Superparamagnetic Nanoparticles. *Small*, **2008**, *4*, 270-278.
2. Kim, M.W.; Han, W.J.; Kim, Y.H.; Choi, H.J. Effect of a hard magnetic particle additive on rheological characteristics of microspherical carbonyl iron-based magnetorheological fluid. *Colloids Surf. A: Physicochem. Eng*, **2016**, *506*, 812-820.
3. Tarama, M.; Cremer, P.; Borin, D.Y.; Odenbach, S.; Lowen, H.; Menzel, A. Tunable dynamic response of magnetic gels: Impact of structural properties and magnetic fields. *Phys. Rev. E*, **2014**, *90*, 1-9.

## APPENDIX

## APPENDIX A

### **Fe<sub>2</sub>O<sub>3</sub>: Dispersion and maximum MNPs loading of PDMS beads**

Appendix A provides more detailed information of how we determined what organic solvent to use during the magnetic PDMS bead synthesis as well as how we determined that the maximum loading of Fe<sub>2</sub>O<sub>3</sub> MNPs in the PDMS beads was about 25 wt% in Chapter 2. It's important to note that these experiments were only conducted for the PDMS beads with non-aligned or randomly distributed MNPs. However, similar results should be observed for the magnetically aligned beads. The maximum loading should be at most 25 wt% since the PDMS beads are of the same size and the alignment likely limits the loading.

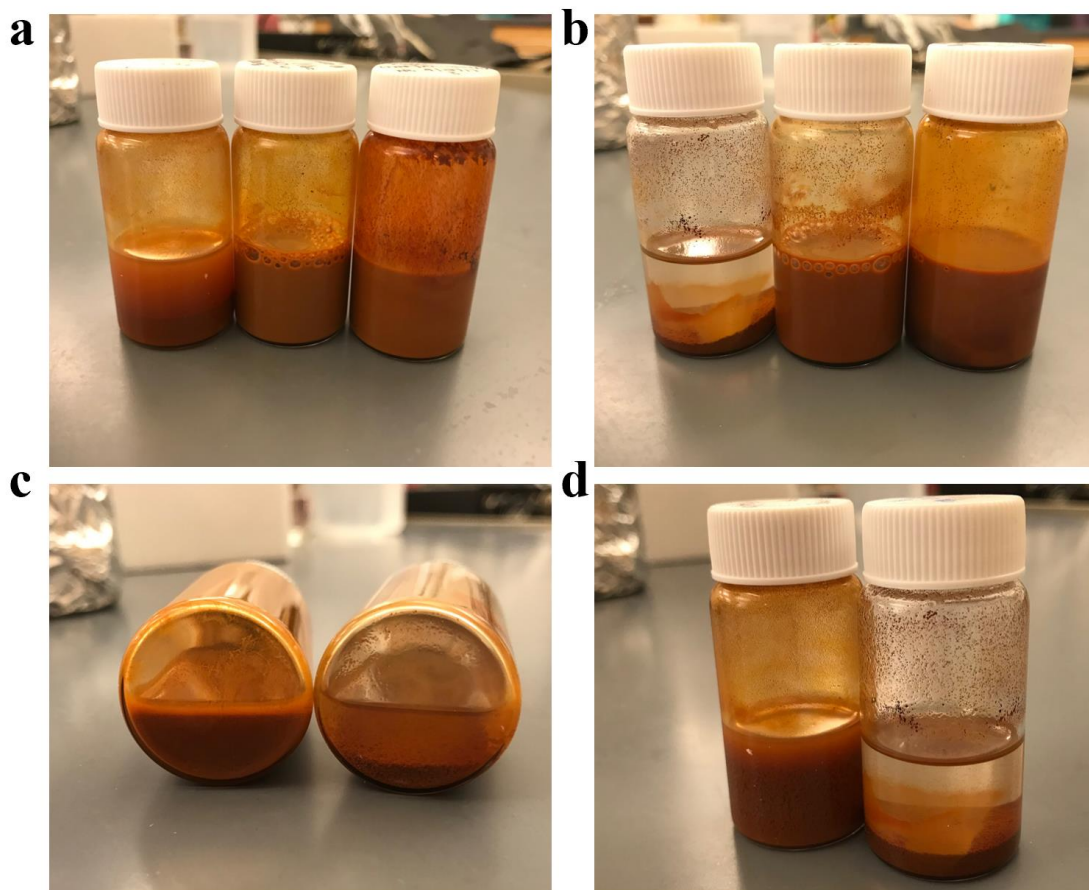


**Figure A.1** Images highlighting two types of organic solvents that were used to try to disperse the Fe<sub>2</sub>O<sub>3</sub> MNPs and to reduce the viscosity of the PDMS Sylgard 184 base. (a) THF was used to disperse the MNPs and (b) toluene was used. (c,d) MNPs dispersed in THF (left) and toluene (right) after 5 hour sonication. As can be observed, only THF resulted in effective MNP dispersion and toluene resulted in MNP sedimentation.

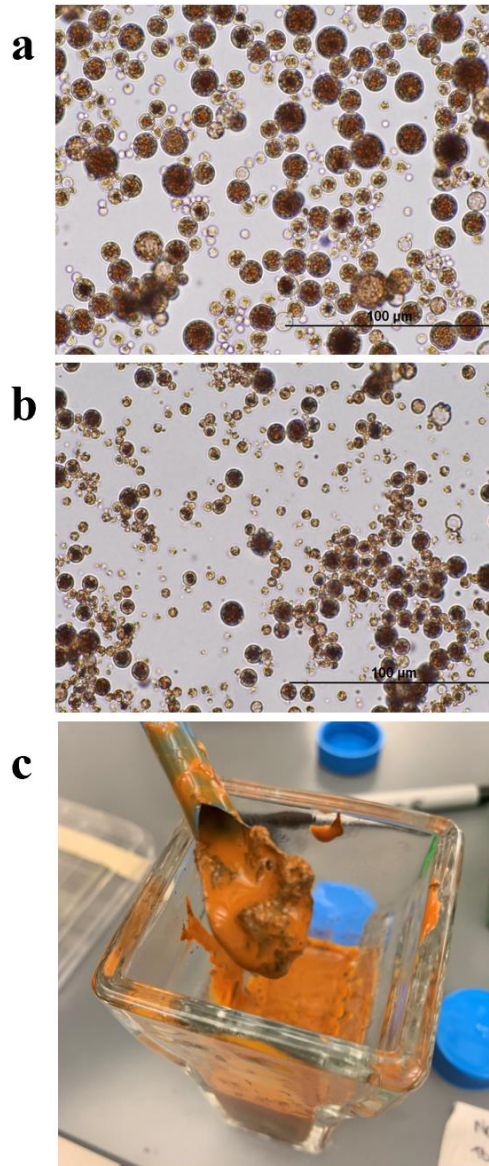


**Figure A.2** Microscopy images of (a) 20 wt%  $\text{Fe}_2\text{O}_3$  MNPs embedded in PDMS beads and (b) 30 wt%  $\text{Fe}_2\text{O}_3$  MNPs embedded in PDMS beads. At 30 wt%, we begin to see smaller PDMS beads and what appears to be residual magnetic material in the cured sample before cleaning the beads. This means that all of the magnetic material is no longer being embedded into the PDMS beads. (c) At 40 wt% MNPs in the PDMS bead, there is a considerable amount of magnetic material left in the chamber as denoted by the darker filament like structures in the blue spatula above. This leads us to conclude that this percentage exceed the loading threshold.